RICE UNIVERSITY

Ultra-short Carbon Nanotubes as Nanocapsules for Medical Imaging and Therapy

by

Keith Bennett Hartman

A THESIS SUBMITTED
IN PARTIAL FULFULLMENT OF THE
REQUIREMENTS FOR THE DEGREE

Doctor of Philosophy

APPROVED, THESIS COMMITTEE:

Lon J. Wilson, Chair
Professor of Chemistry

R. Bruce Weisman
Professor of Chemistry

Adrian V. Lee
Associate Professor
Baylor College of Medicine

HOUSTON, TEXAS
DECEMBER 2007

ABSTRACT

Ultra-short Carbon Nanotubes as Nanocapsules for Medical Imaging and Therapy

by

Keith Bennett Hartman

This thesis details the development of ultra-short, single-walled carbon nanotubes (US-tubes) for use as nanocapsules to contain and deliver medical agents for both imaging (Gd^{3+}) and therapeutic (^{211}At) purposes. In particular, Gd^{3+}-loaded US-tubes, known as gadonanotubes, operate as high-performance MRI contrast agents with relaxivities (image enhancement efficacy) a factor of 40-100 greater than current clinical contrast agents. Furthermore, gadonanotube relaxivities are highly pH-dependent, with image intensity nearly tripling from pH 7.5 to 6.8. Coupled with their high efficacies and targeting potential, these agents are promising candidates for next-generation targeted imaging probes for the early detection of cancer.

Single gadonanotubes have also been encapsulated in a polymer shell for use as an intravenous MRI contrast agent. In addition, a new functionalization scheme has been developed to covalently attach a variety of amino acids in high quantity to the outer surface of the gadonanotubes and to attach a small peptide sequence for targeting breast cancer cells. The gadonanotubes have also been used as magnetic cell labeling agents, while also demonstrating efficacy *in vivo* as contrast agents.

In addition to functioning as an imaging agent platform, the US-tubes have demonstrated efficacy as nanocapsules for radiotherapeutic agents. Astatine-211 (At-

211), an α-emitting radionuclide, can be loaded inside the US-tube with excellent containment stability for the targeted delivery of an α-radiotherapeutic agent to micrometastatic and single-cell cancers. The loading levels for At-211 are comparable to, or better than, other known compounds. At-211, existing as the mixed-halogen compound ^{211}AtCl, is retained in the US-tube nanocapsules due to van der Waals forces between the ^{211}AtCl and the interior sidewalls of the nanotube.

Finally, the US-tubes have been shown to induce few health risks in mammalian experiments. Acute toxicity tests were conducted on mice with both raw and purified full-length carbon nanotubes (SWNTs), as well as US-tubes, using large doses (up to 1 g/kg of bodyweight). Even at these large doses, no animal death was recorded, although in a few cases behavioral changes were observed. Nanotubes were observed to be eliminated from the liver and kidneys through the urine and feces. It is believed that any toxicity at high doses can be attenuated (and prevented) by properly formulating the administered dose.

ACKNOWLEDGEMENTS

I wish to thank my thesis advisor, Prof. Lon J. Wilson, for the opportunity to work with him in his laboratory over the past four years. His assistance, advice, and guidance have been indispensable in my professional growth as a scientist. His outstanding mentorship will be a guide to me throughout my career.

I furthermore wish to acknowledge the other two members of my thesis committee, Prof. R. Bruce Weisman and Prof. Adrian V. Lee, for thesis guidance and fruitful collaborations over the years.

So many collaborators have given their time, expertise, and instrumentation to assist in data collection, for which I am grateful. Without them, this thesis would not have been possible. Thanks to Prof. Andre E. Merbach, Prof. Lothar Helm, Dr. Eva Toth, Dr. Sabrina Laus, and Löick Morrigi at Ecole Polytechnique Fédérale de Lausanne for all of their NMRD work. Thanks to Prof. Paul S. Engel and Dr. Runtang Wang of Rice University for their GadoPegEgg synthesis. Thanks to Prof. Robia G. Pautler, Dr. Amy Hassan, Dr. Bonita Chan, and Lingyun Hu at Baylor College of Medicine and Dr. Raja Muthupillai at Texas for their MR imaging work. Thanks to Prof. D. Scott Wilbur and Don Hamlin at the University of Washington for their At-211 labeling studies. Finally, special thanks to Prof. Fathi Moussa, Dr. Jelena Kolosnjaj, and Sabah Boudjemaa at Université Paris-Sud 11 for their exhaustive study of carbon nanotube toxicity.

I am indebted to the current and past members of the Wilson Group whom I have had the honor to work with on many projects: Jared Ashcroft, Scott Berger, Matthew Cheney, Stuart Corr, Phillip Hodge, Kyle Kissell, Yuri Mackeyev, Michael Matson,

Daniel Matthews, Andrey Mirakayan, Preeti Misra, Chris Myers, Ivana Peralta, Sophie Phounsavath, Richard Piggott, Balaji Sitharaman, Jeyarama Subramanian, Lesa Tran, and Tatiana Zakharian. It was a pleasure to work with each of you, and I wish you the best in your future endeavors.

Thanks to the Robert A. Welch Foundation, the Center for Biological and Environmental Nanotechnology, the US National Institutes of Health, the Helis Medical Foundation, and the Norman Hackerman Fellowship in Chemistry from Rice University for financial support and Carbon Nanotechnologies, Inc. for the gift of nanotubes.

Finally, I would like to thank my family and Cristina Hofmann for all of their love and support, without which, this thesis would not have been possible. They are a constant source of inspiration and motivation, encouraging me to pursue my highest aspirations.

TABLE OF CONTENTS

LIST OF FIGURES

CHAPTER I

CHAPTER II

CHAPTER III

CHAPTER IV

CHAPTER V

LIST OF TABLES

CHAPTER II

CHAPTER III

CHAPTER IV

LIST OF SCHEMES

CHAPTER III

CHAPTER IV

CHAPTER I: INTRODUCTION

Magnetic Resonance Imaging

In 2003, Paul Lauterbur and Peter Mansfield were awarded the Nobel Prize in Medicine in recognition of their development of magnetic resonance imaging (MRI), now a fundamental medical imaging technique. Essentially, the MR instrument images water, making this technique ideally suited for the visualization of soft tissues in the diagnosis of cancers, ligament damage, and brain activity. Annually, approximately 60 million MR images are obtained worldwide.

Derived from the principles of nuclear magnetic resonance (NMR), clinical MRI uses a strong homogenous magnetic field to align the proton spins of water and then measures the time it takes them to equilibrate after perturbation, a process known as relaxation.[1] Differences in relaxation times are portrayed in the MR image as varying shades of white and gray. Although water has a very slow relaxation time and is ubiquitous in living organisms, complex instrumentation and mathematical algorithms are able to filter the data and coarsely differentiate between neighboring tissues which have slightly different relaxation times.

Because it is difficult to distinguish between similar tissue (e.g. a tumor within fat tissue), chemical contrast agents (CAs) are often used to enhance images. CAs operate by decreasing the relaxation time of local water protons by introducing a paramagnetic species, thus allowing for better differentiation between areas of interest. Dozens of CAs have been approved by the United States Food and Drug Administration (FDA), typically consisting of a chelated Gd^{3+} compound (Magnevist, a common clinical Gd^{3+}-based CA

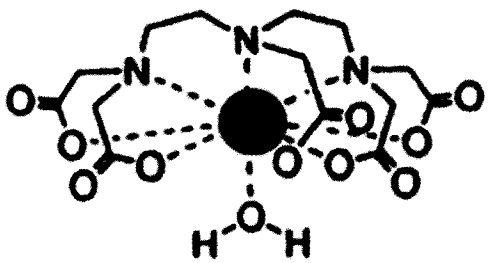

Figure 1: A common Gd^{3+} chelate MR contrast agent, $[Gd(DTPA)(H_2O)]^{2-}$ (Magnevist).

is shown in Figure 1) that circulates in the blood until eliminated through the kidneys. Proton relaxation occurs via two mechanisms: longitudinal relaxation, known as r_1, and transverse relaxation, or r_2. An r_1-agent produces a positively-enhanced image (the image brightens), and it is usually a paramagnetic ion (Gd^{3+} or Mn^{2+}). An r_2-agent produces a negatively-enhanced image (the image darkens), and it is typically a superparamagnetic species (nanocrystalline Fe_3O_4). Generally clinicians prefer r_1 agents as it is easier to distinguish features in a brightened image as opposed to a darkened image.

Relaxivity is relatively simple to measure. About 0.2 mL of sample is placed in an NMR tube and positioned in a relaxometer or NMR instrument. Although temperatures can be varied to determine characteristics of the system, the most medically-relevant data is acquired at 37 °C (body temperature). A uniform magnetic field aligns the proton spins of the sample and a pulse inverts the magnetization vector; the time required for the magnetization vector to realign is known as the relaxation time (T_1 or T_2, depending on whether it is an r_1 or r_2 agent). Fortunately, water protons relax slowly, on the order of several seconds. Upon the addition of a CA, the relaxation time decreases to tens of milliseconds. Because the relaxation time is concentration dependent, mathematical adjustments are made to yield "relaxivity", a standard by which

all contrast agents are compared quantitatively for efficacy. The magnitude of the relaxivity (units are $mM^{-1}s^{-1}$), is directly proportional to the efficacy of a given contrast agent. Typical relaxivities for clinical agents at 37 °C and clinical-field strengths (~60 MHz or 1.5 Tesla) are approximately 4 $mM^{-1}s^{-1}$.[2,3]

Current imaging methods are able to distinguish between neighboring tissues of different composition and anomalies within these tissues. However, in the case of tumors, too often by the time a tumor is large enough to be detected with today's imaging technology, it is metastatic and too late for a cure. To this end, medical imaging research strives to image the most fundamental unit of life: the cell. Known as molecular imaging, researchers seek to develop "smart CAs" that are molecularly targeted to diseased cells (tumor cells, arterial plaque cells, etc.) so as to accumulate within targeted cells, in order to detect disease (via some abnormal cellular biochemistry) at its earliest stage when relatively few cells are present.[4-7] Such capabilities would allow for earlier diagnosis of cancer, arterial blockage, etc., leading to an increase in successful therapies and the preservation of more lives. Pursuant to these goals, engineered nanostructures may be able to overcome many of the limitations of current clinical MRI CAs. Specifically, today's CAs are not targeted to sites of disease, not internalized by cells, and have relaxivities much too low to realize molecular imaging. However, nanomaterials, due to their unique or enhanced properties, are gaining attention as possible solutions to these limitations.

Nanotechnology in Medicine

Several nanomaterials have already established a strong presence in medicine. Quantum dots[8,9] and gold nanoshells[10] have demonstrated efficacy in mammals as agents in fluorescence imaging,[11-14] surface-enhanced Raman scattering,[15] and thermal ablation.[16,17] Currently, the most developed nanomaterial in medicine is superparamagnetic iron oxide (SPIO).[18,19] Viewed on the macroscale, rust (iron oxide) is hardly exotic, however, on the nanometer scale, iron oxide particles exhibit remarkable magnetic behavior that makes them attractive candidates for advanced medical materials. Because of their nanoscale size, SPIO particles have a single magnetic domain, resulting in a large magnetic moment, known as superparamagnetism.

The iron oxide species that has gained the most attention for medical applications is magnetite (Fe_3O_4), which has mixed oxidation states of iron.[20] Particle sizes can range from several nanometers to hundreds of nanometers in diameter.[21] Because magnetite SPIOs possess highly-aligned/single-magnetic domains, they have a very large magnetic moment, making them especially effective MRI contrast agents.[1,22] In addition to chemical composition, other parameters that can influence relaxivity are the degree of crystallinity/size of the SPIO particle and the agglomeration of the particles inside the body.[22]

Several commercial SPIO agents are available with a variety of external coatings. Many such agents have been explored as CAs for MR imaging in humans,[23-27] often "targeting" (more likely due to being a particulate, than being molecularly-targeted) liver tumors.[28] Much work still needs to be done to determine the relationship between pharmacokinetics, particle size, and surface modification. Typical blood half-lives are

found to vary between one hour for anionic coatings to 24-36 hours for starch coatings in humans and 2-3 hours in mice.[23-27]

SPIOs offer a convenient platform for covalent attachment of biologically-relevant moieties due to their large, relatively easily-derivatized surface. SPIO-labeled antibodies have been used to image a variety of targets, including rectal carcinoma,[29] breast cancer,[30] and VCAM.[31] Other targeting systems include the HIV-1 tat peptide for lymphocyte imaging,[32,33] hormones for breast cancer,[34] and folic acid as a general targeting strategy for cancer.[35] SPIOs have also been used as magnetic labels for tracking stem cells *in vivo*.[36,37]

These versatile agents are not only limited to imaging, but can also function as magnetically-induced hyperthermia therapeutic agents. The word "hyperthermia" is Greek for "over-heat". It has long been known that tumor cells are more susceptible to heat than are healthy cells, thus, if SPIOs can exercise fine control over tissue temperature, they may act as cancer-selective agents.[38-40] Magnetic hyperthermia is based on the phenomenon that metals produce an electrical current in an alternating magnetic field.[41] Electrical conductivity in any metal is accompanied by resistance which dissipates energy as heat to the surrounding medium. A superparamagnetic species, with a single magnetic domain, has an enhanced effect caused by the relaxation of the domain dipole which results in heat dissipation, a process known as Néel relaxation. A far weaker field is needed to achieve the same level of heating with a nanoscale superparamagnetic material relative to larger ferromagnetic materials and thus, single-domain SPIOs (3-7 nm in size) far outperform their larger, ferromagnetic counterparts in *in vitro* experiments.[42] Calculations suggest that successful tumor

ablation could be accomplished with a mere 5-10 mg of SPIO/cm^3 of tissue.[43] A major problem is the difficulty in localizing and sequestering these particles inside a single tissue. However, the recent completion of a Phase I clinical trial yielded promising results for the treatment of prostate cancer using SPIOs as hyperthermia agents, where decreases in prostate specific antigen, a protein correlated to prostate cancer, were recorded in 8 of 10 patients.[44]

Carbon Nanostructures in Medical Imaging

Nanostructures. While quantum dots, gold nanoshells, and superparamagnetic iron oxide clearly demonstrate that nanotechnology has much to offer medicine by way of new materials with novel properties and capabilities, carbon nanostructures, especially carbon nanotubes, have the potential for an even bigger impact on medicine because they are much more versatile.

In 1996, the Nobel Prize in Chemistry was awarded to Robert Curl, Harold Kroto, and Richard Smalley for the discovery of a new allotrope of carbon known as fullerenes, with C_{60} or "buckyball" being the prime example.[45] This discovery marked the beginning of extensive research into carbon-based nanotechnology. The two main building blocks of carbon nanotechnology are fullerenes (C_{60}, C_{72}, C_{80}, C_{2n}, etc.), most of which are spherical (or nearly spherical) molecules and carbon nanotubes, which are tube-like materials (Figure 2).[46,47] A full-length, single-walled carbon nanotube (SWNT) can be visualized as a single layer of graphene, rolled upon itself, assuming the morphology of a drinking straw; full-length SWNTs range from ca. 300-3000 nm in length, with a ca. 1.0 nm diameter. All carbon atoms are on the surface of SWNTs and are sp^2 hybridized.

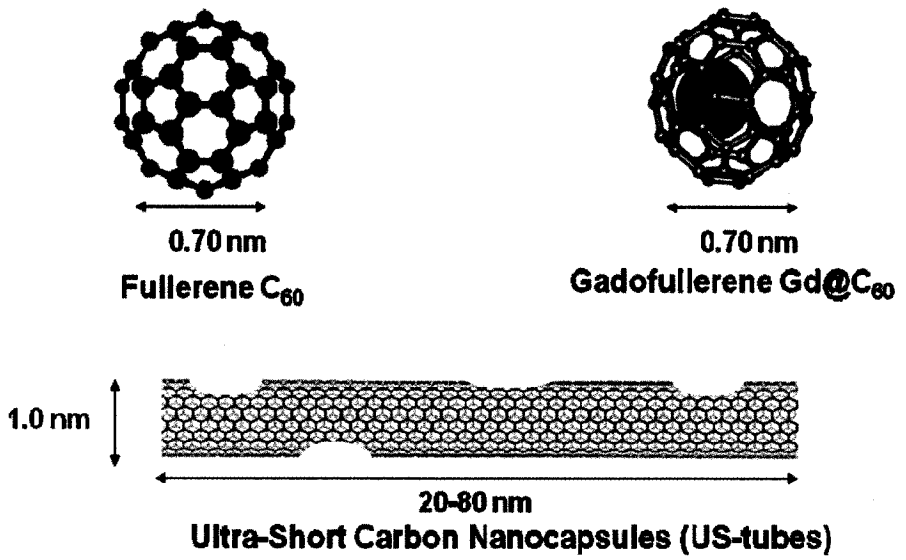

Figure 2: The building blocks of carbon nanotechnology.

Furthermore, the interior of a SWNT is empty, allowing for the filling with small molecules or ions. Ultra-short carbon nanotubes (US-tubes), with sidewall defects from the cutting process (Figure 2), have proven especially efficient in loading. Fullerenes, such as C_{60}, C_{80}, etc., can also be filled (with great difficulty) with 1-3 metal ions to produce endohedral metallofullerenes such as Gd@C_{60}, as also shown in Figure 2.

Carbon Nanotube Fluorescence. SWNTs come in a variety of sizes and chiralities (determined by the angle of the roll-up vector of a sheet of graphene) which control the type of nanotube, semi-conducting or metallic, existing in approximately a 2:1 ratio in a given batch of SWNTs.[48,49] The band-gap of the semi-conducting SWNTs controls the fluorescence properties. Altering the diameter and chirality of the carbon nanotube alters the band gap, which in turn controls the fluorescence properties. SWNTs are immune to

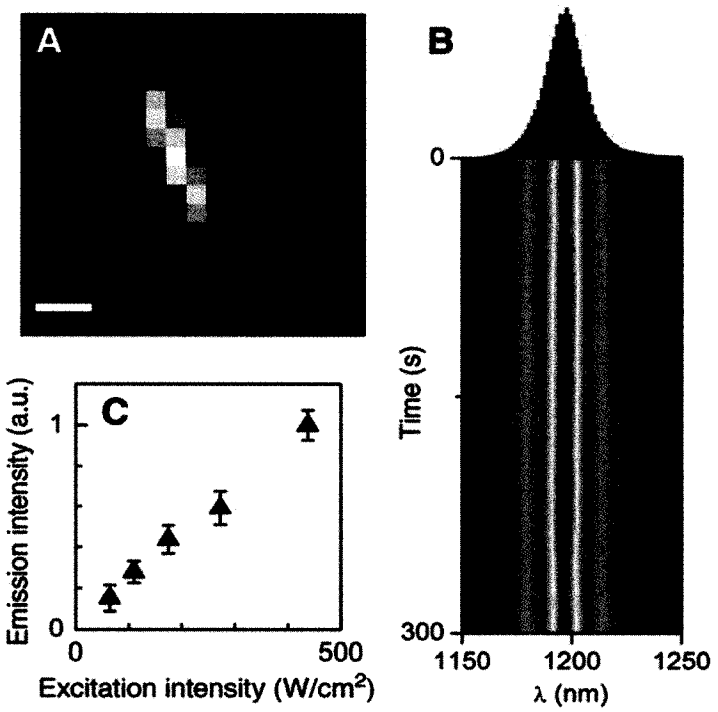

Figure 3: (A) Image of a single SWNT excited at 1000 W/cm^2, scale bar = 100 nm; (B) Spectral intensity of the same SWNT demonstrating signal intensity over 5 minutes (5 second measurement intervals); (C) Emission intensity as a function of excitation intensity of the same SWNT.[51]

photobleaching and they do not "blink" like quantum dots,[50] and amazingly, even a single nanotube has been imaged by fluorescence microscopy (Figure 3).[51]

This SWNT fluorescence has been exploited as an optical imaging agent in living organisms. It has been used to image the uptake of SWNTs in macrophages,[52] elimination of SWNTs from i.v. injection in rabbits,[53] and biocompatibility effects of SWNTs on fruit-fly larvae.[54] Finally, exploiting the strong near-infrared (NIR) absorption properties of SWNTs has resulted in their application as hyperthermia agents.[55] In the study, folate-labeled SWNTs were preferentially internalized by cancer cells, and upon irradiation with near-infrared light, the nanotubes were heated hot enough to induce cell death selectively to the cancer cells, without harming the surrounding

healthy cells. In a similar vein, another method utilized radiofrequency (RF) radiation to heat carbon nanotubes and kill a tumor in a rabbit model.[56]

Gadofullerenes. One of the first use of carbon nanomaterials in medicine was the application of gadolinium-encapsulated fullerenes (gadofullerenes) as MR contrast agents.[57-63] Initially, gadofullerenes were attractive contrast agents because the fullerene cage acts as a perfect chelate (it is impossible for Gd^{3+} to escape the cage) and the relaxivity (efficacy) of the gadofullerenes is superior to traditional Gd^{3+} chelate-based MRI CAs, like Magnevist. For example, $Gd@C_{60}[C(COOH)_2]_{10}$ and $Gd@C_{60}(OH)_x$, have relaxivity values ranging from 20 $mM^{-1}s^{-1}$ to 100 $mM^{-1}s^{-1}$ (per Gd^{3+} ion) at 1.5 T and 37 °C, which is approximately 5-20 times greater than current clinical CAs.[63] Originally believed to be due to the unique confinement of the Gd^{3+} ion and aggregation effects,[61] more recent studies have demonstrated that the extremely slow molecular tumbling time of the individual gadofullerenes (1.2 ns) and the nanoscale confinement of water molecules within the gadofullerene aggregates are the main reasons for the increased relaxivity over traditional Gd^{3+}-chelated clinical agents.[62] The nuclear magnetic relaxation dispersion (NMRD) profile, a plot of relaxivity as a function of magnetic field strength, for the gadofullerenes can be modeled using classical Solomon-Bloembergen-Morgan (SBM) theory of paramagnetic relaxation.[64-68] The gadofullerene plot, shown in Figure 4, is a nearly perfect fit for the molecular-rotation-optimized SBM relaxation.[63,69] Gadofullerenes have been used to magnetically label stem cells for *in vivo* tracking.[62] Several recent reports have attached fullerene materials to antibodies for potential use in targeted drug delivery.[70,71]

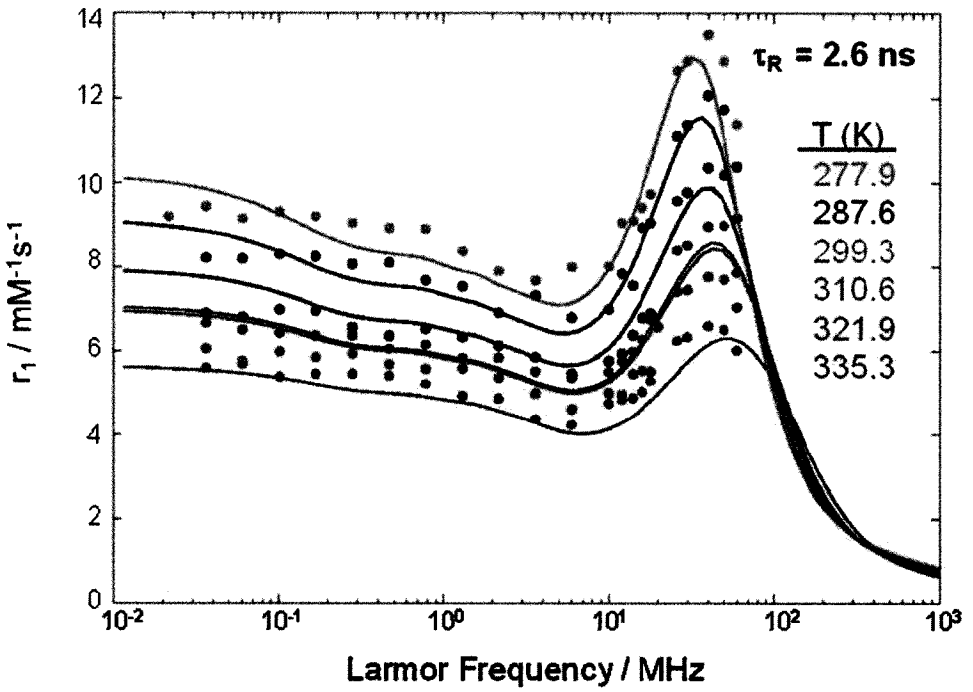

Figure 4: NMRD plot of $Gd@C_{60}[C(COOH)_2]_{10}$ as a function of temperature (circles) and the SBM optimized theoretical curve (solid lines) for slowly-rotating molecules.[63]

While gadofullerenes are attractive candidates for next-generation CAs, a major problem with all gadofullerenes is the enormous difficulty of synthesizing amounts large enough to permit clinical application. Obtaining gram quantities of purified gadofullerenes is both chemically challenging and extremely time consuming. $Gd_3N@C_{80}$ has higher yields, but it is much more difficult to chemically derivatize. These two obstacles (low yields and synthetic difficulties) make the short-term implementation of these materials into the clinic problematic. This realization prompted the investigation of alternative nanostructures (ultra-short carbon nanotubes) which are more available in mass quantities to substitute as a carbon cage.

This thesis will detail the development of ultra-short carbon nanotubes (US-tubes) as a nanoscale molecular capsule platform for medical imaging and therapy. The advantages of this platform are multi-fold. Their carbon exterior functions as a scaffold for the design of a nanoscale molecular carrier platform. Due to their intrinsic lipophilic character (even when derivatized to be water-soluble), carbon nanotubes readily cross cell membranes, and because of their bio-inertness, act as robust molecular capsules. Coupled with the easily-functionalized surface, they are attractive candidates for the development of an intracellular nanocapsule delivery vehicle. Upon loading US-tubes with Gd^{3+} (known as gadonanotubes), the gadonanotubes were discovered to act as a high-performance MRI contrast agent, dramatically outperforming all known contrast agents.[72] The high relaxivities (efficacies) of these agents make them attractive molecular imaging candidates to image at the cellular level. They have been derivatized with a variety of functional groups for biocompatibility and cell targeting. In order to demonstrate their therapeutic possibilities, the US-tubes have also been internally-loaded with At-211, an α-radionuclide, at levels comparable (or higher) to others reported in the literature. Finally, initial toxicity studies in mice suggest that any US-tube toxicity can be satisfactorily attenuated through proper dose formulation.

CHAPTER II: GADONANOTUBES: OPTIMIZATION AND CHARACTERIZATION

The original motivation for the development of gadonanotubes was to investigate an alternative Gd@carbon nanostructure to gadofullerenes. Although the latter exhibited a marked increase in relaxivity compared to traditional Gd^{3+}-chelates, the extreme synthetic difficulty, relatively low yields, and prohibitively high production costs made near-term clinical application of these materials highly unlikely. Thus, the US-tubes, which can be made relatively inexpensively and in significantly large quantities, offered a possible alternative to the fullerene cage. However, much to our surprise, the gadonanotubes had even larger relaxivities than the gadofullerenes, making them not only attractive candidates for next-generation targeted imaging, but a significantly more viable platform for near-term medical implementation than their fullerene counterpart.

US-tube Synthesis

Full-length, single-walled carbon nanotubes (SWNTs) are chemically cut into ultra-short segments (US-tubes) by the fluorination/pyrolysis method.[73] In a typical experiment, 500 mg of raw, full-length SWNTs were placed in a Monel boat and sealed in a custom-built fluorinator apparatus pictured in Figure 5. The system was purged with pure He gas for 45 minutes and heated to 50 °C for high pressure carbon monoxide (HiPco) produced SWNTs or 100 °C for arc ablation (Arc) produced SWNTs. Differences in temperature account for varying reactivity rates between SWNT types. HiPco-produced SWNTs are smaller in diameter (0.8-1.0 nm), possessing greater bond strain, and hence greater reactivity, than their Arc-produced counterparts (1.3-1.5 nm in

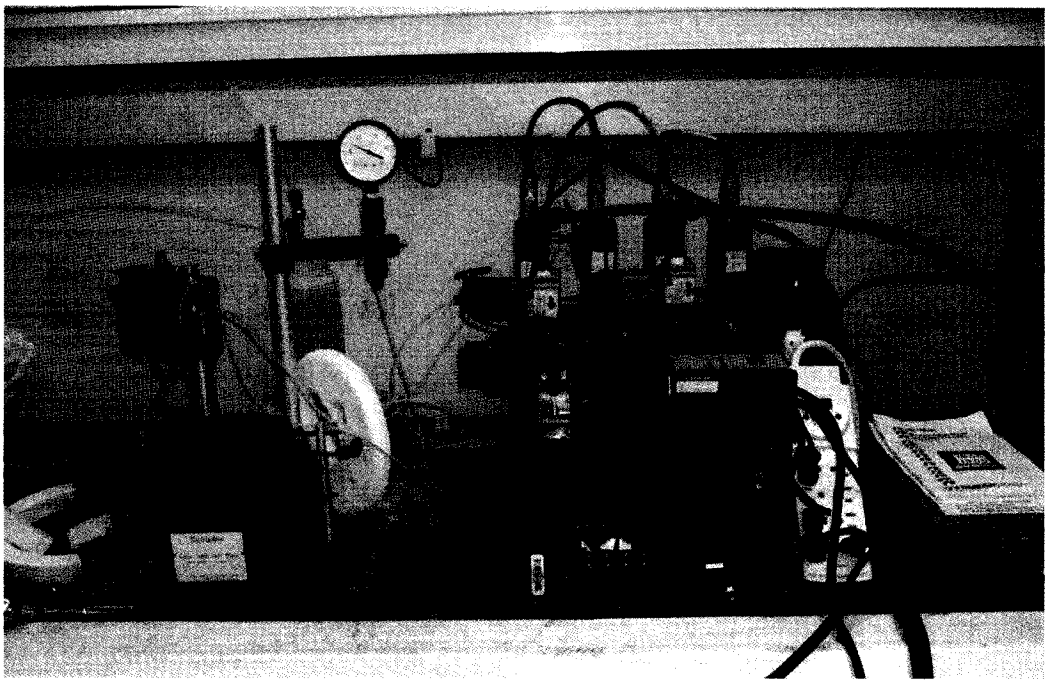

Figure 5: Custom-built Monel fluorinator apparatus.

diameter). After the system reached the set temperature, the tubes were fluorinated with gaseous F_2 (1%) in He for 2 hours. The F_2 gas was then turned off, and the sample cooled for 1 hour under a flow of He to remove any unreacted F_2 from the reactor. The fluorination of SWNTs does not result in a random deposit of fluorine along the length of the nanotube, but rather, fluorine forms bands of C-F bonds around the circumference of the nanotube. These bands are several nm in axial length, with 20-100 nm of relatively unfunctionalized nanotube between bands.

Upon removal of the fluorinated SWNTs from the reactor, they were heated under flowing Ar gas to 1000 °C in a tube furnace for 1 hour. The volatile fluorocarbons were driven off, leaving behind the ultra-short carbon nanotube segments (US-tubes) typically 20-100 nm in length. The result of this cutting method yields nanotube segments with several defect sites in the sidewalls which facilitates the internal loading of ions and small

molecules. Next, the US-tubes were added to ca. 75 mL of concentrated HCl and bath sonicated for 45 minutes to remove the metal catalyst impurities. The sample was then gravity-filtered over a rough sintered glass filter and washed several times with 20 mL aliquots of deionized water. The US-tubes were either collected on a watch glass and dried in an oven at 80 °C or directly added to an aqueous solution of Gd^{3+} ions for loading. The dried, empty US-tubes can be loaded later with ions or small molecules, functionalized for targeting or bio-compatibility, or chemically reduced to obtain single US-tubes.

Much like SWNTs, US-tubes exist in large bundled aggregates, rather than discrete single US-tubes, due to the strong intermolecular van der Waals interactions between the nanotubes. The force between SWNTs is ca. 0.5 eV per nm of carbon nanotube,[74] an incredibly strong force that is difficult to mechanically overcome by sonication alone. However, by chemically reducing the SWNTs or US-tubes, a single nanotube species can be obtained.

While several methods can successfully accomplish de-bundling of nanotubes (e.g. Na^0 in liquid ammonia or NaH in toluene), the US-tubes were usually reduced using the Na^0 in THF method.[75] In this procedure, ca. 1 mg of metallic sodium was added for every 1 mg of US-tubes in 100 mL of dry, distilled THF (maximum of 60 mg of nanotubes). The solution was bath sonicated for 1 hour prior to quenching with deionized water, filtering, washing, and drying. This process worked successfully for both SWNTs and US-tubes. Figure 6 shows an AFM image of de-bundled US-tubes with lengths of ca. 40 nm and heights of 0.5-1.2 nm, suggestive of single US-tubes.

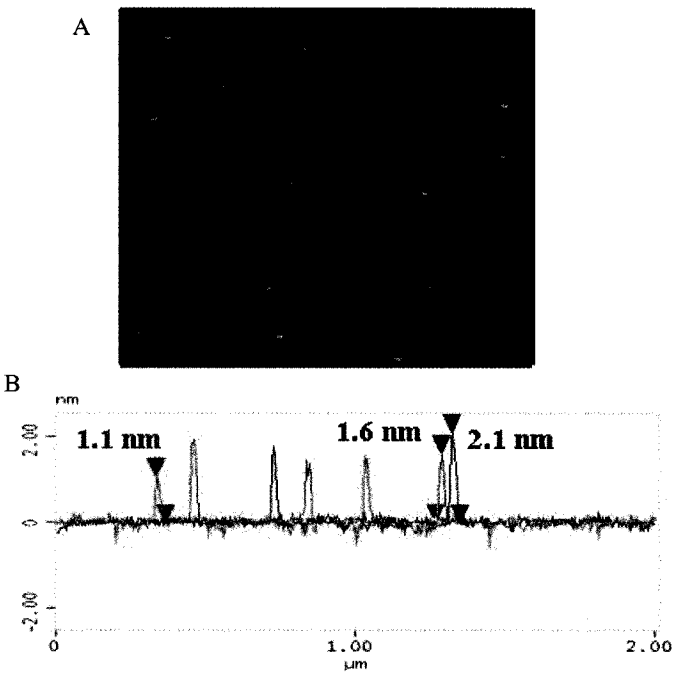

Figure 6: (A) AFM height image of reduced US-tubes and (B) Z-scan resolution height analysis of reduced US-tubes.[75]

Gd^{3+}-Loading of US-tubes

US-tubes were loaded with aqueous Gd^{3+} ions by sonicating the sample in ca. 1 ppt $GdCl_3$ in deionized water at ca. pH = 4.5. Typical loading was accomplished by sonicating the sample for 30-60 minutes, followed by unperturbed soaking for at least another 60 minutes before collecting the sample on a rough sintered glass filter. The sample was then washed with several aliquots of deionized water. Studies of Gd^{3+}-ion loading revealed that little to no loading occurred if the US-tubes were filtered immediately following sonication. However, 15 minutes of soaking after a five minute sonication period produced significant Gd^{3+}-ion loading with high-performance relaxivity characteristics. Superconducting quantum interference device (SQUID) measurements revealed that the gadonanotubes are superparamagnetic and that their magnetic behavior is characteristic of small clusters.[72] Coupled with electron imaging, the Gd^{3+}-ions are

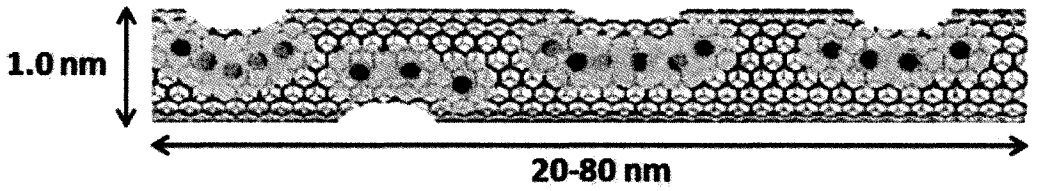

Figure 7: Pictorial representation of the gadonanotubes.

believed to reside in the sidewall defects in the US-tubes in small clusters of 3-10 Gd^{3+} ions, as illustrated in Figure 7.

Once loaded with Gd^{3+} ions, the gadonanotubes can be directly suspended in water via a dispersion agent or dried in a furnace at 60 °C for subsequent derivatization or suspension at a later time. Due to the innate insolubility of carbon nanotubes, the gadonanotubes must be "solubilized" with the aid of a dispersion agent, typically a surfactant or a protein matrix, for relaxivity measurements. To accomplish this, roughly 1 mg/mL of gadonanotubes was added to a 0.1-1% aqueous solution of the dispersion agent and sonicated for 1-5 minutes. Most gadonanotube batches were suspended in an ionic surfactant, sodium dodecylbenzene sulfonate (SDBS), for characterization because it was the most effective agent. Other biocompatible agents were also explored, including polyethylene glycol, starch, bovine serum albumin (BSA) proteins, and pluronic F-108. The relaxivity was found to be independent of SDBS and pluronic surfactant coating.

Methods of Gadonanotube Relaxivity Characterization

Initial characterization of a gadonanotube sample began with a T_1–weighted relaxation time using a Bruker mq60 MiniSpec operating at 60 MHz (1.41 Tesla). This value was used to compute a relaxivity using the following formula:

$$r_n = \frac{\left(\frac{1}{T_n} - \frac{1}{T_d}\right)}{c}$$

where r_n is the T_n-weighted (either T_1 or T_2, measured in seconds) relaxivity and c is the concentration of the paramagnetic substance in mM.[1] A full plot of relaxivity as a function of magnetic field was obtained for several samples. Data points at 20, 40, and 60 MHz were obtained with Bruker MiniSpec mq series instruments while data points from 1 MHz to 20 MHz were obtained using a custom-built, variable-field relaxometer, and high-field measurements were obtained using Bruker NMR instruments at 100, 200, and 400 MHz. Temperature baths were used for all data acquisition to regulate sample temperature.

Due to the small concentrations of Gd^{3+} in the suspended samples (ca. 0.05 mM), determination of the concentration is of utmost importance since any error will greatly affect the relaxivity calculation. The best method for the determination of Gd^{3+}-ion concentration is inductively-coupled plasma optical emission spectroscopy (ICP-OES), which has sub-ppb sensitivity. All measurements were conducted on a Perkin-Elmer Optima 4300DV ICP-OES instrument. For a typical Gd^{3+} concentration measurement, 500 μL of suspended gadonanotubes were added to ca. 1 mL of 30% chloric acid ($HClO_3$) and gently heated to the boiling point. The chloric acid oxidatively destroyed the nanotube (as evidenced by the change in color from black to colorless). The sample

was heated until almost all liquid was boiled off. The sample was then diluted to 10.00 mL in a volumetric flask with a 2% HNO_3 solution, with care taken to ensure that all Gd^{3+} was extracted from the original vessel by multiple 0.5 mL washings with the HNO_3 matrix. The sample was filtered through a 0.22 μm syringe filter to remove any undigested nanotubes. Typical Gd^{3+} concentrations in the gadonanotube samples ranged from 0.02 mM to 1.5 mM. Some of the initial suspensions were sent to Galbraith Laboratory for professional elemental analysis and the results were statistically identical to our own measurements. Estimations suggest there are ca. 100 Gd^{3+} ions per US-tube.

A plot of relaxivity as a function of magnetic field is known as a nuclear magnetic resonance dispersion (NMRD) plot. This curve can be fitted through classical Solomon-Bloembergen-Morgan (SBM) theory to determine a variety of molecular and electronic parameters.[64-68] The NMRD profile of the first gadonanotube reported and the plot of Magnevist is shown in Figure 8.[72] This plot has several features that cannot be fit by

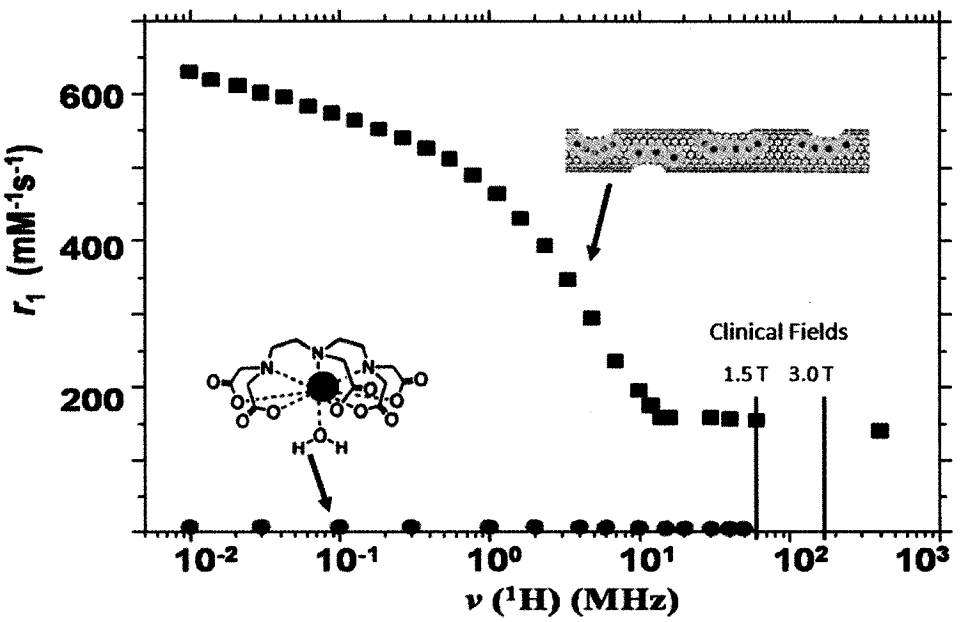

Figure 8: An NMRD profile of the gadonanotubes and Magnevist. Common clinically-used fields are marked at 1.5 and 3.0 T.

SBM theory: i) The increasing relaxivity as magnetic field strength is reduced, ii) constant relaxivity at high fields, and iii) the magnitude of the relaxivity. The failure of SBM theory to model these new materials is likely due to their superparamagnetic clusters and the fast flow rate of water through a carbon nanotube.[76]

Gadonanotube Optimization

Typical characterization of a gadonanotube sample involved first measuring the T_1 at 37 °C and 60 MHz and then digesting a small amount of the sample to determine the Gd^{3+} concentration used to calculate a relaxivity value. If the sample had a high relaxivity value (>60 $mM^{-1}s^{-1}$), further tests were conducted to determine temperature, pH, or salt effects. Stability was qualitatively measured by periodically re-measuring the T_1 of a suspended sample. An unstable sample resulted in the precipitation of gadonanotubes, leading to lower relaxation rates (greater T_1 times). Measuring the relaxivity of an empty US-tube or Eu^{3+}-loaded US-tube resulted in low relaxivities (lower than that of the clinical Gd^{3+} chelate agents). Thus the Gd^{3+} is certain to be responsible for these remarkable relaxivities.

Drying out the sample did appear to affect relaxivity performance of the gadonanotubes. US-tubes can be extensively loaded (30% by mass) using molten anhydrous $GdCl_3$ (melting point = 609 °C), but the relaxivity is very low, ca. 4 $mM^{-1}s^{-1}$. In this case, it is believed that the US-tubes are full of tightly-packed $GdCl_3$ in which most of the Gd^{3+}-ions are inaccessible to bulk water protons, thereby substantially lowering the relaxivity.

Nanotube Type. The two main processes for synthesizing carbon nanotubes are the HiPco and the Arc procedure. HiPco tubes are typically smaller in diameter (ca. 1 nm) compared to Arc nanotubes (ca. 1.4 nm) in diameter. The former are synthesized using an iron catalyst, while the latter use a nickel-yttrium catalyst. Gadonanotubes were prepared from both of these nanotube types. In general, relaxivity was the same for the two types. However, the Arc tubes suspend better (more tubes in suspension) and therefore, gave stronger signals. The HiPco tubes were often difficult to suspend in high concentrations. Therefore, for most experiments, Arc-produced tubes were used. HiPco nanotubes are much easier to derivatize owing to their smaller diameter and greater chemical reactivity, so when the exterior of the US-tubes were functionalized, HiPco gadonanotubes were used (see Chapter III).

Gd^{3+} Counter-Anion. The first gadonanotube sample was prepared by soaking the US-tubes in an aqueous solution of $GdCl_3$. XPS measurements indicated a Gd:Cl ratio of 1:3, and the Gd peak is much closer to $GdCl_3$ than Gd_2O_3, suggesting that the clusters within the US-tubes are composed mostly of $GdCl_3$. A set of experiments was conducted to see if the anion played a significant role in the degree of Gd^{3+}-loading or the relaxivity. From the same batch of Arc US-tubes, samples were loaded with a 2.6 mM aqueous solution of one of the following: $GdCl_3$, $Gd(NO_3)_3$, $Gd(CH_3COO)_3$, or $Gd(CF_3SO_3)_3$. Table I records the relaxivity and the concentration of Gd^{3+} in solution for each of the samples.

Table I: Relaxivity values as a function of magnetic field (at 37 °C), high-field maxima (obtained from NMRD profile), and Gd^{3+} concentrations of 4 different Gd salt preparations. All samples suspended in SDBS.

Anion	$[Gd^{3+}]$ (mM)	r_1 (60 MHz) $mM^{-1}s^{-1}$	r_1 (40 MHz) $mM^{-1}s^{-1}$	r_1 (30 MHz) $mM^{-1}s^{-1}$	High-field Peak Maxima (MHz)
Chloride	0.194	60.9	65.8	61.8	45.4
Nitrate	0.177	53.4	58.2	54.5	44.8
Triflate	0.112	60.1	65.7	61.2	44.9
Acetate	0.268	48.5	51.3	42.9	48.8

The anion size does not appear to influence Gd^{3+} ion loading as recorded in Table I. The sample with the greatest Gd^{3+}-loading was that for acetate, one of the larger anions. At a casual glance, the anion does not appear to affect relaxivity since the triflate and chloride samples have nearly identical relaxivities at three measured fields. However, a close examination of the acetate and the chloride-loaded samples revealed a small, but significant, upward shift in the relaxivity peak maximum frequency, as shown in Table I. These maximum points were determined by fitting the truncated NMRD curves as second degree polynomials. In the six different chloride samples that were tested, all exhibited similar maxima (within 1 MHz). The acetate sample is shifted by 3.5 MHz or about 0.1 Tesla. This suggests that the anion may play a role in shifting the relaxivity maxima of the NMRD curves, which may allow the possibility of customizing gadonanotube performance by selecting the proper anion to suit the field strength of the MR scanner.

pH Dependency. Initial work exploring the relaxivity characteristics of gadofullerenes found that their relaxivities were partially due to aggregation state and solution pH.[61,63] Acidic solutions created larger gadofullerene aggregates, and therefore larger relaxivities.

In order to assess possible similarities between the gadonanotubes and gadofullerenes, relaxivity and aggregate size of the gadonanotubes were measured as a function of pH.

Relaxivities (per Gd^{3+} ion) of SDBS-suspended gadonanotubes were acquired as a function of pH from 3-10 at 60 MHz and 37 °C. pH was altered using sub-μL amounts of 1 *M* LiOH and HCl. The mass of the sample was measured after addition of each acid or base and was less than 0.01 mg, so Gd^{3+}-ion concentration change was negligible.

The plot of r_1 as a function of pH at 60 MHz and 37 °C is shown in Figure 9. The r_1 vs. pH curve was found to be fully reversible upon pH cycling. As seen from Figure 9, the relaxivity of the gadonanotubes undergoes more than a three-fold increase in relaxivity from pH = 8.3 (40 $mM^{-1}s^{-1}$) to pH = 6.7 (133 $mM^{-1}s^{-1}$) at 37 °C, with the slope of the change between pH 7.4 and 7.0 being 98 $mM^{-1}s^{-1}$/pH. Although the magnitude of

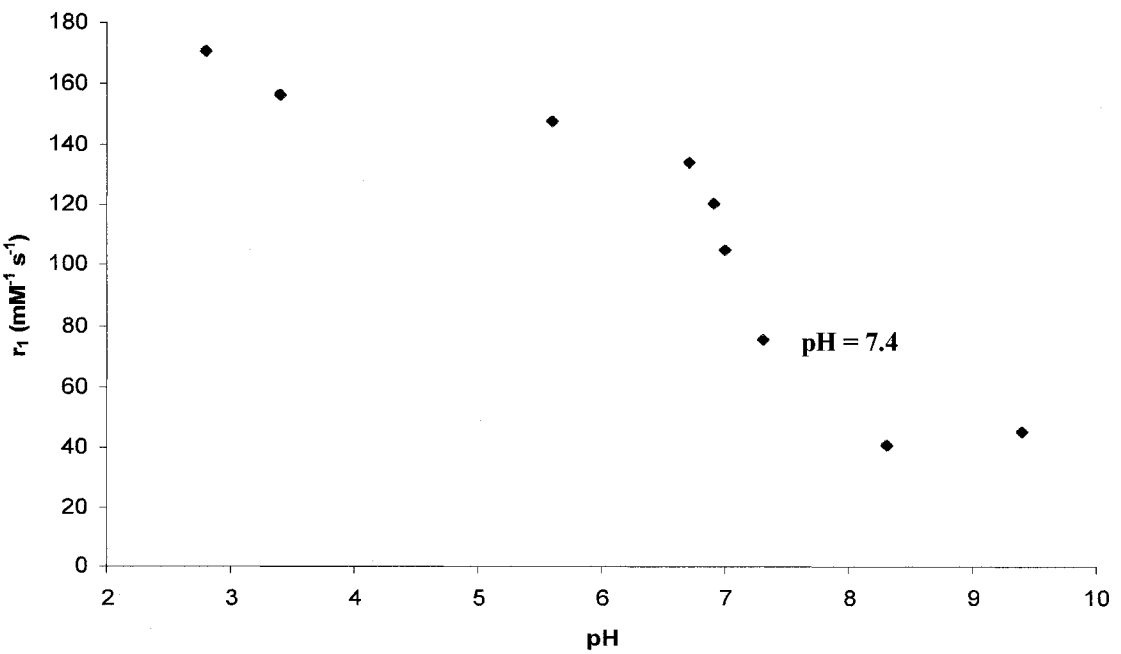

Figure 9: A plot of relaxivity as a function of pH for the gadonanotubes at 60 MHz and 37 °C.

the relaxivity change can vary somewhat between different batches of gadonanotube preparations, samples other than that from Figure 9 have demonstrated at least a 25% increase in relaxivity from pH 7.4 to 7.0, with the greatest being a 100% increase (a 300% increase from pH 8.3 to pH 6.9). This has the potential to be a very important discovery, as tumor cells exhibit depressed pH levels (pH=6.9 or lower) compared to healthy tissue (pH=7.4).[77,78]

No other pH-responsive MRI CA has demonstrated such a dramatically-large change in relaxivity over such a narrow pH range. For example, a pH-responsive agent described by Woods *et al.* utilized a pH-respondent pendant arm that ligates Gd^{3+} ion at high pH and releases it at low pH and undergoes a 60% increase in relaxivity from 4.4 $mM^{-1}s^{-1}$ at pH 8.5 to 7 $mM^{-1}s^{-1}$ at pH 6.5 (slope = 1.3 $mM^{-1}s^{-1}$/pH).[79] A Gd^{3+}-DO3A tetrapod system detailed by Jebasingh and Alexander exhibited a near-doubling of relaxivity from 3.2 $mM^{-1}s^{-1}$ at pH 8.5 to 6 $mM^{-1}s^{-1}$ at pH 6.5 (slope = 1.4 $mM^{-1}s^{-1}$/pH).[80] Another example, a PAMAM dendrimer-based system, has demonstrated an approximate 20% increase in relaxivity over similar r_1/pH ranges (slope = 4.4 $mM^{-1}s^{-1}$/pH).[81] Finally, a few Gd@C_{60}-based CAs (gadofullerenes) also exhibit r_1/pH variation which is strongly aggregation-state dependent (slope < 10 $mM^{-1}s^{-1}$/pH).[59,63,82] Thus, the gadonanotubes are interesting materials for MRI CA development, not only because they possess the greatest efficacy (relaxivity) by far at clinical fields of any known CA, but also because of their dramatic response to pH around physiological pH.

While the aforementioned relaxivity measurements are the accepted standard by which CAs are compared, relaxivity measurements do not guarantee that agents will perform accordingly in an MRI scanner. To confirm its pH-dependent properties in an

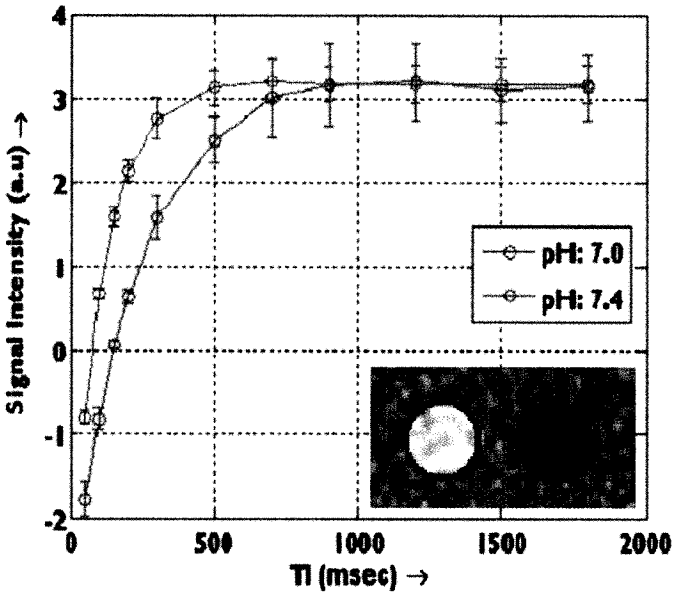

Figure 10: An inversion recovery MR scan of the gadonanotubes at pH = 7.0 (red) and pH = 7.4 (green) at 1.5 Tesla (63.8 MHz).

MRI scanner, a sample of gadonanotubes was divided into two parts, in which one part was adjusted to pH = 7.0 and a second to pH = 7.4. The pH was measured both before and after the MRI scan and found to be unchanged. A T_1-weighted inversion-recovery scan was collected on the two samples using a 1.5 T Philips MR scanner which confirmed a large relaxivity difference between the two samples (Figure 10). The image in Figure 10 shows the significant difference in the relaxivity of the two samples, which differed by a mere 0.4 pH units. The relaxivities from the images were calculated to be 200 $mM^{-1}s^{-1}$ (pH 7.0) and 98 $mM^{-1}s^{-1}$ (pH 7.4) at 25 °C.

To investigate whether the pH dependency of the gadonanotubes was an aggregation phenomenon (as is the case for gadofullerenes), dynamic light scattering (DLS) measurements were collected using a Nanotrac Ultra DLS Nanoparticle Analyzer, as a function of pH. In the DLS experiment, pH was adjusted incrementally from 5.3 to

8.5 and then back down to 7.4, 7.0, and 5.3. Five measurements were taken at each point, with the high and low measurement discarded, and an average of the three remaining measurements at each point was plotted in Figure 11. The accuracy of the measurements was validated with a 20 nm polystyrene bead standard.

The DLS data proves that aggregation of the gadonanotubes does not play a major role in their high-performance relaxivity characteristics. Previous studies on Gd@C_{60} found that relaxivities were both pH and aggregation state dependent.[59,63,82] For example, gadofullerene aggregates range in size from 50 nm at pH = 9 to 1200 nm at pH = 4, with relaxivities of 75 $mM^{-1}s^{-1}$ at pH $\approx$ 4 and 39 $mM^{-1}s^{-1}$ at pH $\approx$ 10. Thus, it was first assumed that gadonanotubes would also exhibit a similar aggregation state behavior and that this would be related to their pH-dependent relaxivities. However, the DLS data clearly demonstrates that the aggregation-state behavior of the gadonanotubes is vastly different than that for gadofullerenes and is unlikely to contribute to the observed relaxivity properties.

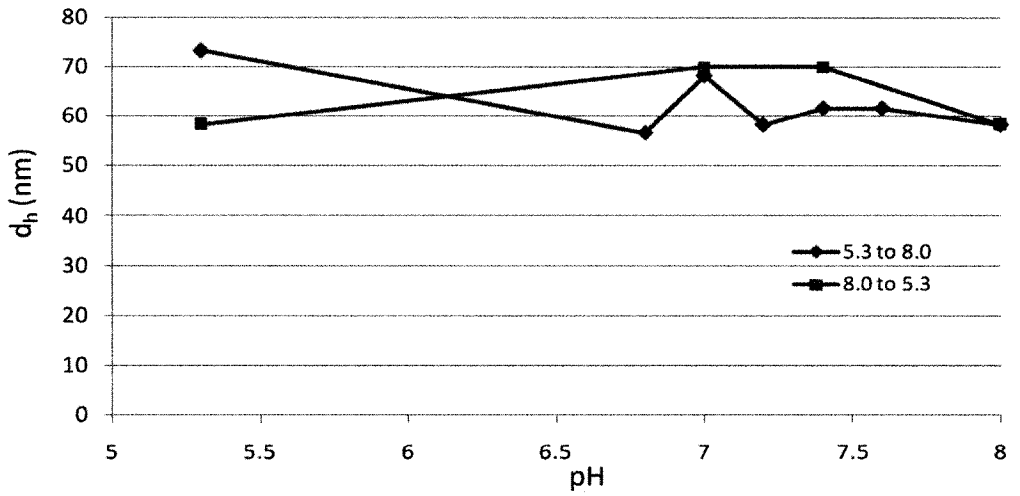

Figure 11: DLS measurements of the hydrodynamic diameter as a function of pH for the gadonanotubes. The sample was adjusted from 5.3 to 8.0 (blue) and then back down from 8.0 to 5.3 (red).

Gd^{3+} Cluster Stability. An alternative explanation of the pH-relaxivity relationship is that pH manipulation leads to Gd^{3+}-ion loss from the gadonanotubes upon exposure to alkaline solutions. Because the superparamagnetic clusters are believed to be a key to the high-performance characteristics of these probes, the integrity of these Gd^{3+}-ion clusters and their retention of Gd^{3+} are of utmost importance. The scope of the experiment was widened to test not only pH, but also different physiological challenges, including phosphate buffered saline solution (PBS), bovine serum, and heat. In an additional set of experiments, a sample of gadonanotubes was membrane dialyzed in PBS solution for 48 hours, with samples periodically taken for Gd^{3+}-ion analysis. None of these trials resulted in a measurable loss of Gd^{3+}-ion as determined by ICP-OES. Furthermore, there was no adverse effect on gadonanotube relaxivity after dialysis. The dialysis experiments confirmed that the Gd^{3+}-ion clusters are stable with regard to physiological conditions and that Gd^{3+} ion is not leaked from the gadonanotube itself. The limit of detection for ICP-OES instrumentation is ca. 1 ppb, which is less than 1% of the total Gd^{3+}-ion concentration present in a gadonanotube sample. Thus, the gadonanotubes retained greater than 99% of their Gd^{3+}-ion concentration upon exposure to pH and temperature challenges, as well as the physiological condition challenge mimicked by PBS dialysis. Taken together with the DLS results, the physiological challenge data indicate that the high-relaxivity property of the gadonanotubes is not due to an aggregation phenomenon, nor are Gd^{3+} ions released from the gadonanotubes during pH cycling, since the pH-dependent relaxivities of Figure 9 are reproduced exactly upon repeated cycling.

Temperature. To investigate the temperature dependence of the water exchange rate (assuming access to Gd^{3+} ions by water), a temperature dependence study was performed on three gadonanotube samples, with one sample under acidic conditions (pH = 2.8), a second sample under basic conditions (pH = 9.4), and a third sample at physiological pH = 7.4 at 60 MHz. The results of the study are shown in Figure 12. This plot of relaxivity vs. temperature demonstrated that the relaxivity is independent of temperature under basic conditions, whereas under acidic conditions the relaxivity rose dramatically to ca. 500 $mM^{-1}s^{-1}$ as the temperature was lowered from 50 °C to 5 °C. The general shape of the temperature plot for the acidic curve in Figure 12 has been previously documented for a Gd^{3+} chelate attached to a large protein where the relaxivity nearly tripled from 3.2 $mM^{-1}s^{-1}$ to 8.2 $mM^{-1}s^{-1}$ over the same temperature range.[83] There are two possible explanations for the strong increase of relaxivity at pH 2.8 by lowering temperature: (i) A formation of larger aggregates leading to slower rotational motion or (ii) slower rate of proton exchange. Previous DLS data suggest that aggregation does not appear to

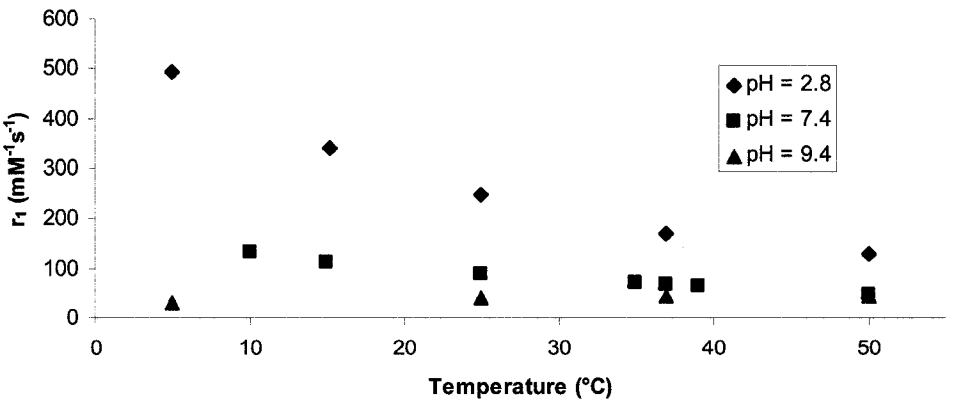

Figure 12: Relaxivity as function of temperature for the gadonanotubes at 60 MHz.

influence relaxivity dynamics, thus eliminating the aggregation explanation. Therefore, if we assume that the high relaxivity observed with gadonanotubes is due to high mobility of water protons, a property known from several studies,[84,85] we can assume that relaxivity is limited at high temperatures by fast proton exchange and that the lowering of temperature would lead to an increase in r_1.

Conclusion

Clearly gadonanotubes are intriguing building-block materials for the development of clinical MRI CAs, not only because they possess unprecedentedly high relaxivities, but also because they can be made relatively inexpensively in large quantities, with relatively high reproducibility. We have demonstrated that nanotube type (HiPco or Arc) and suspension agent (SDBS, F-108, BSA, etc.) does not appear to play a significant role in relaxivity performance. The anion identity may play a small role in the relaxivity peak maximum, which might allow for some tailoring of the relaxivity.

Although the relaxivity of gadonanotubes exhibits an impressive thermal response, it is unlikely to be of practical use in medicine or biology since the relaxivity change is relatively small over the narrow range of temperatures found in biology. In contrast, because of the sharp and dramatic change in relaxivity over physiologically-relevant pH ranges, the gadonanotubes make compelling agents for the development of pH-sensitive CA probes. The DLS and physiological challenge experiments demonstrate that these effects cannot be attributed to aggregation effects or Gd^{3+} ion loss from the tube. Coupled with the fully recyclable relaxivity curve, these phenomena unique to the gadonanotubes, are possibly attributed to the exceptionally fast water flow through

carbon nanotubes, or to complex bridging oxide/hydroxide structures known in lanthanide clusters. There is clearly still more that needs to be further investigated in this system before it is fully understood.

With their high relaxivity alone, the gadonanotubes make for an attractive circulatory CA candidate, especially in attempts to diagnose areas of cellular stress such as cancer or ischemia where the extracellular pH is 6.9 or lower (physiological pH is 7.4).[77,78] Because of the ultra-sensitivity of these agents to minute pH change, they also might lend themselves to a variety of other physiological applications that depend upon tight pH regulation, including certain enzymes that operate within narrow pH ranges[86] or processes involving heart mechanics,[87,88] or might even function as a non-targeted cancer detection probe. However, before such applications can be fully realized, gadonanotubes must be derivatized for biocompatibility and/or targeting and demonstrate that their high relaxivity performance is maintained in living systems. Some of the initial studies will be discussed in Chapter III.

CHAPTER III: GADONANOTUBES: FUNCTIONALIZATION FOR *IN VITRO* AND *IN VIVO* IMAGING

The previous chapter detailed the characterization of a new, nanotube-based MRI contrast agent, known as gadonanotubes. The relaxivity of this agent is the highest ever reported for a T_1-agent, and its sensitive response to pH is unprecedented. Classical SBM theory of paramagnetic relaxation cannot fit the relaxivity characteristics of the gadonanotubes, likely because of their new nanoscale properties. These properties make them attractive candidates in the development of next-generation, high-performance MRI applications, such as cellular tracking, early cancer detection, and single-cell imaging (yet to be accomplished by a T_1-weighted MRI contrast agent). In order for this to be realized, the gadonanotubes must be made biocompatible and/or targeted to cancer cells and demonstrate efficacy in living systems. This chapter will detail various solubilization and cancer targeting schemes, as well as initial *in vitro* and *in vivo* imaging of the gadonanotubes.

GadoPegEgg

The simplest application of a contrast agent in medical imaging is that of an intravenous contrast agent (e.g. ionic Gd^{3+} chelates such as Magnevist).[1] These agents are injected into the bloodstream and circulate through the body for a short time before being eliminated. Maximum contrast agent solubility is desired, and such agents are not targeted to tissues of interest, nor do they accumulate inside of cells. In previous studies, gadonanotubes were suspended non-covalently using a surfactant, sodium dodecyl benzenesulfonate (SDBS) to conduct measurements. Unfortunately, SDBS is highly

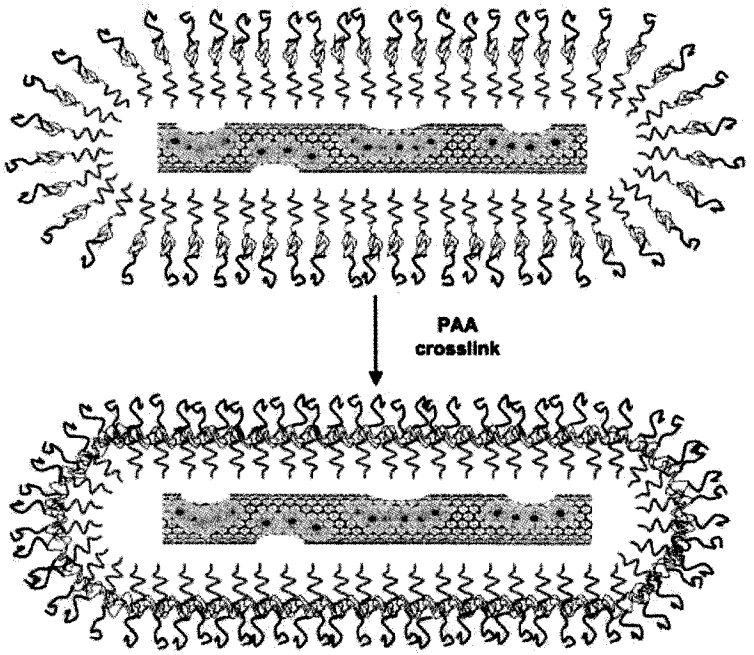

Figure 13: The GadoPegEgg encapsulate (figure amended from the original literature report[89]).

toxic and is not suitable for animal studies, thus, an alternative had to be found. One solution is the direct functionalization of the gadonanotubes, but this can be difficult due to the inert nature of the carbon nanotube, and highly water-soluble and salt-stable nanotube materials have yet to be discovered. Covalent functionalization strategies are more likely to be applied to specialized applications where performance, not solubility, is most important. Another possibility is the use of a biocompatible surfactant, such as pluronic or tween, but previous reports suggest that these types of non-covalent coatings are lost from the nanotubes, possibly within seconds of injection, and replaced by plasma proteins.[52]

A very promising solution to this problem is a recently developed material known as PEG-egg.[89] In this material, the nanotube is suspended inside a shell-crosslinked

polyethylene glycol (PEG) micelle, resulting in a highly stable material. There is no covalent attachment of this PEG shell to the outside of the nanotube, thus, the Gd^{3+} clusters and gadonanotube sidewalls remain intact (Figure 13). This product is denoted as 'GadoPegEgg'. The PEG encapsulation should also resist protein displacement, resulting in long blood circulation times needed for intravenous application.[90,91]

Materials and Methods. Gadonanotubes were synthesized as previously described using HiPco-produced carbon nanotubes. The PEG micelle shell synthesis has been recently reported[89] and was followed with minor amendments. In brief, the tri-block copolymer poly(ethylene glycol)-b-poly(acrylic acid)-b-(polystyrene) (PEG-PAA-PS) was synthesized by previous literature methods. Water was slowly added to a DMF solution of gadonanotubes and PEG-PAA-PS under probe tip sonication. To initiate the crosslinking of the polymer, EDC was added, followed by 2,2'-(ethylenedioxy)diethylamine (Figure 14). The sample was then purified by dialysis and fractional centrifugations at 5000 rpm. The resulting pellet was resuspended in HPLC grade water by sonication.

The sample was imaged on a JEOL 2010 transmission electron microscope (TEM) operating at 100 keV. Samples were prepared by evaporating a drop of diluted sample on a lacey carbon TEM copper grid. Atomic force microscopy (AFM) was performed using a Digital Instruments IIIa Nanoscope AFM instrument. Samples were spin-coated onto a mica wafer prior to analysis.

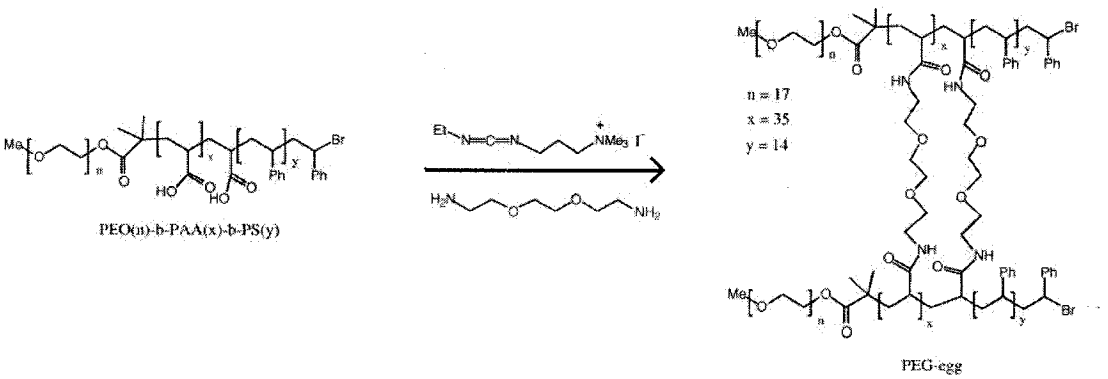

Figure 14: The cross-linking procedure to form the PEG-egg shell (figure amended from original literature report[89]).

Results. In the TEM image (Figure 15A), a single tube wrapped with a ca. 5 nm PegEgg shell coating the exterior can be clearly seen. This evidence is corroborated by AFM (Figure 15B) in which ovular features are clearly observed. The GadoPegEgg conjugate spans from 40-75 nm in length, with z-resolution heights of ca. 1.5-4.2 nm. The widened, flat structures are indicative of the GadoPegEgg laying flat on the surface, with the PEG coating flattened out, suggestive of individual GadoPegEgg conjugates. In solution, they would morphologically be more like rods as observed in the TEM, rather than as flat discs observed by the AFM.

The GadoPegEgg conjugate was soluble at ca. 4 mg/mL, by far the most stable of any nanotube suspension scheme. Furthermore, it was highly stable towards PBS solution and demonstrated stability for an excess of 2 weeks upon salt addition (most other systems flocculate in minutes or hours). The impressive stability of this conjugate is attributed to the single-species nature of the conjugate (i.e. not heavily bundled as observed for surfactant-suspended gadonanotubes).

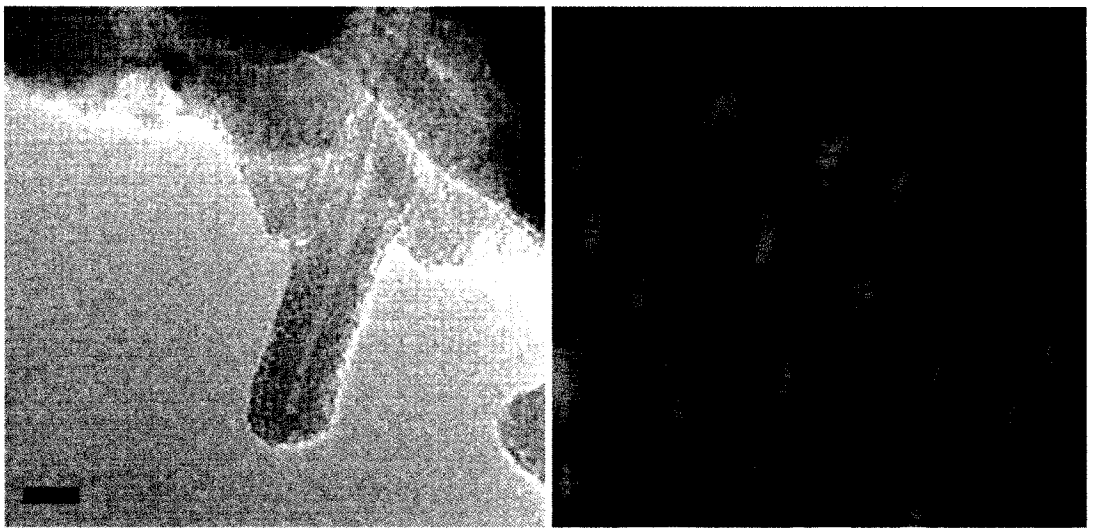

Figure 15: (A) A TEM image of the GadoPegEgg (scale bar = 10 nm) shows a single nanotube with ca. 5 nm of PegEgg shell around the tube. (B) An AFM image of the GadoPegEgg (750 nm x 750 nm) in which most conjugates are between 40-75 nm in length with heights up to 4.2 nm.

Initial relaxivity characterization indicated that the Gd^{3+} clusters inside the gadonanotube are not disturbed. The relaxivity of the GadoPegEgg at 37 °C, 60 MHz, and pH = 6.0 at 60 MHz was 87 $mM^{-1}s^{-1}$, indicating that the large relaxivity values are not diminished buy the coating. However, subsequent experiments revealed that the GadoPegEgg relaxivity behaved in sharp contrast to previous gadonanotube suspensions in SDBS. Unlike the gadonanotubes in SDBS, which showed extreme sensitivity to pH changes (Figure 9), the GadoPegEgg relaxivity was relatively unchanged by pH (see Appendix II).

In an attempt to discern possible reasons for this discrepancy, a full NMRD profile was obtained at 37 °C (Figure 16). Whereas the earlier reported NMRD plot for gadonanotubes suspended in SDBS is characterized by increasing relaxivity at low fields (<10 MHz; see Figure 8), the profile for the GadoPegEgg in Figure 16 is relatively flat at low fields. The qualitative shape of the plot is more reminiscent of gadofullerenes (or an SBM theoretical fit of a molecular rotation-optimized chelate;[69] see Figure 4) than that of

previous gadonanotube profiles. This may be because the GadoPegEgg is more like a "discrete" molecule, compared to bundled gadonanotubes in the SDBS-suspended samples. The AFM and TEM data clearly show that the samples are single nanotubes, in contrast to the previously reported surfactant-suspended gadonanotubes which are significantly bundled.[92] If the relaxivity was due to the molecular rotation (i.e. slow tumbling rate), it should exhibit a strong temperature dependence, however, this was not observed for the GadoPegEgg (see Appendix II).

This suggests that molecular environment plays a very strong role in gadonanotube relaxivity. Coupled with the anion-relaxivity dependence described in Chapter II, these data further suggest that gadonanotube relaxivity (and the response to temperature and pH) may be further controlled through the gadonanotube coating. For instance, surface covering might alter the inner-sphere/outer-sphere relaxation mechanisms, water exchange rates, proton mobility rates, or another parameter yet to be discovered. Clearly, there is more work to be done in this area to better understand this new contrast agent.

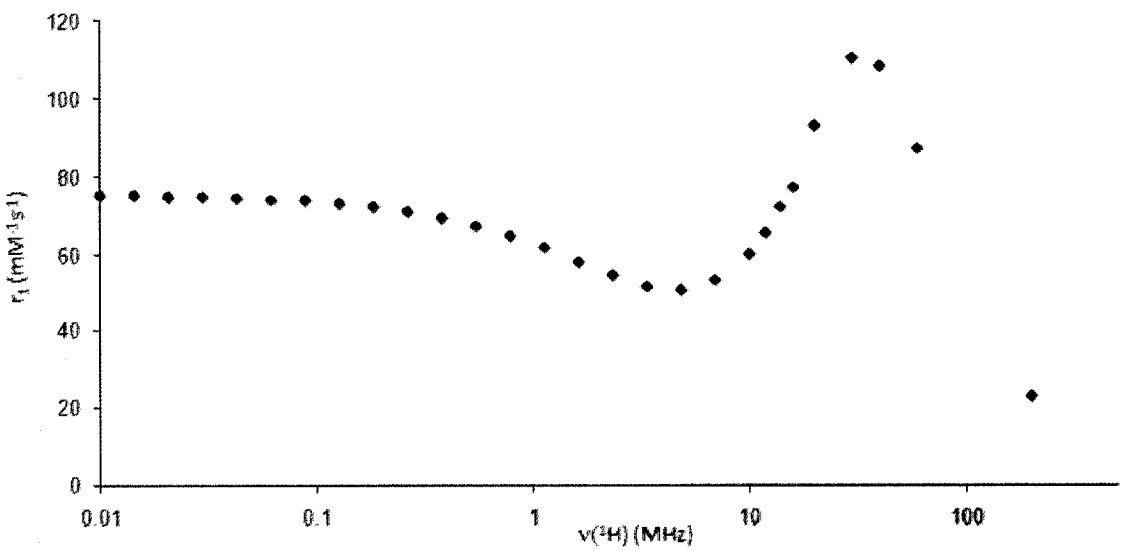

Figure 16: An NMRD plot of the GadoPegEgg, the shape of which is a clearly different than that of earlier SDBS-suspended gadonanotubes.

Covalently Functionalized Gadonanotubes

While the GadoPegEgg is a notable advance toward the application of gadonanotubes into medicine, it is not a good candidate for the realization of molecular imaging which requires cell-specific targeting. The PEG moieties in the GadoPegEgg scheme cannot be functionalized (at least with great control or pure products), nor do typical PEG encapsulates enter cells. As a result, we investigated direct covalent attachment of targeting ligands to the exterior of the gadonanotube. Although we have previously documented addition of water-solubilizing groups via the Bingel reaction, this mechanism only attached about 4-6 groups per nanometer of nanotube, and the products were not stable in salt solution.[75] Thus, we have developed a new functionalization scheme that uses an organometallic catalyst to attach a wide variety of solubilizing and cell targeting moieties with much greater coverage of the gadonanotube exterior surface.

Materials and Methods. The gadonanotubes were prepared from HiPco nanotubes because, due to their increased ring strain, they were found to be much easier to derivatize than their Arc counterparts. The gadonanotubes were dried at 60 °C prior to functionalization. The derivatization of the gadonanotubes is shown in Scheme I. Raman spectroscopy, thermogravimmetric analysis (TGA), and XPS data for compounds **II-V** are shown in Appendix III.

In a typical experiment, 20 mg of purified gadonanotubes (**I**), dried under N_2(g) at 100 °C for 12 hours, were dispersed in 100 mL of anhydrous toluene by bath sonication. 1 mL of a freshly-prepared, saturated solution of rhodium carbonyl, $Rh_6(CO)_{16}$, in THF (~ 4 mg) and 200 mg of ethyl diazoacetate were then added. The suspension was stirred

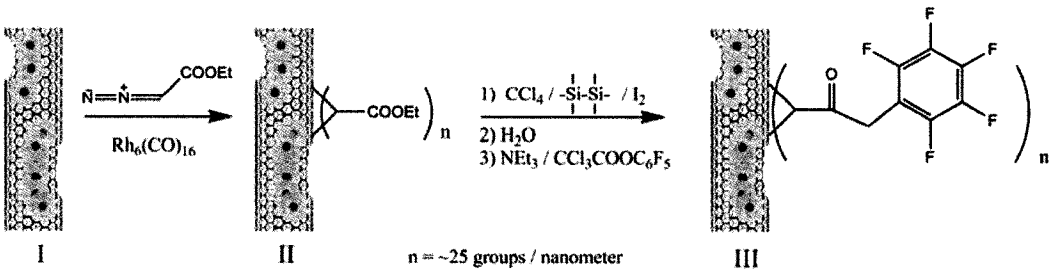

Scheme I: Derivatization scheme for the covalent functionalization of gadonanotubes.

under N_2 at 90-100 °C for 96 hours. Usually the coverage of the SWNT surface increases from 5-9 cyclopropanations per nanometer of tube after 24 hours, to 14-25 cyclopropanations per nanometer of tube after 96 hours; however, further treatment did not increase coverage. The SWNT ester (**II**) was filtered from solution, washed with toluene, methanol and water, and then dried under N_2 at room temperature.

30 mg of purified **II**, dried under N_2(g) at 100 °C for 12 hours, were dispersed in 20 mL of anhydrous CCl_4 by bath sonication. 0.1 mL of hexamethyldisilane (0.5 mmol) and 63 mg of I_2 (0.25 mmol) was added. The suspension was stirred under N_2 at 60 °C for 24 hours. All steps, excluding sonication, were performed in the drybox. Afterwards, the gadonanotube intermediate was collected by filtration, washed with methanol and water, and suspended in water with 2 hours of sonication. The product was washed repeatedly and then dried under N_2 at room temperature. It was then dispersed in 10 mL of anhydrous dioxane by sonication, and 0.33 g of perfluorophenyl 2,2,2-trichloroacetate and 0.1 mL of anhydrous Et_3N were added. The vial was sealed and sonicated at 50 °C for 2 hours and then stirred at 50 °C for 2 days. The gadonanotube derivative **III** was filtered from organic solvents and washed with dioxane on a PTFE filter. Compound **III**, which is sensitive to moisture, but stable under anhydrous conditions for months, readily reacts under mild conditions with sterically unhindered primary amines in several

solvents including dioxane, methylene chloride, or DMF to yield amides (Compounds **IVa-f** and **V**, Table II).

Results. Compound **III** was used as a starting material to attach several different amino acid derivatives, **IVa-f** and **V**. Compound **IVa** was used to estimate the number of groups per nanometer of tube using X-ray photoelectron spectroscopy (XPS) to determine the atomic percentage of nitrogen, since the reaction with $MeNH_2$ is quantitative. Thus, Scheme I is a new, convenient method to make the gadonanotubes water-soluble by attaching alcohol-containing compounds like serinol or hydroxy amino acids, such as threonine and serine.

Table II compiles the coverage, solubility, and relaxivity for each of the attached groups. Several amino acid derivatives yielded appreciable solubility, in the 1-2 mg/mL range, but the most soluble compound was obtained by the attachment of threonine. This

Table II: Gadonanotube functionalities, coverage, solubilities, and relaxivities.

Derivative	**-OR / -NHR groups**	**Abbreviation**	**Groups per nm of tube**	**Solubility (mg/mL)**	**r_1 (mM^{-1} s^{-1})**
I (SDBS)	n/a		0	0	64
II	- OEt		14-25	0	28
III	- OC_6F_5	PFP ester	14-19	reacts	n/a
IVa	- NHMe	N-methyl amide	12-19		60
IVb	-$NHCH(CH_2OH)_2$	Serinol	12	1-2	
IVc	-$NHCH(CO_2H)(CH_2)_2SMe$	Met	11	0	21
IVd	-$NHCH(CO_2H)CH_2OH$	Ser	14	1-2	47
IVe	-$NHCH(CO_2H)CH_2(Me)OH$	Thr	9	3	49
IVf	-$NHCH(CO_2H)(CH_2)_3NHC(NH_2)=NH$	Arg	12	1-2	33
V	-RGD+Ser	RGD+Ser	8-9	1-2	33

cationic amino acid derivative was the most soluble at 3 mg/mL, however, it immediately precipitated out of solution upon exposure to salt, likely due to the change in ionic strength of the solution. Thus, non-ionic amino acids are probably the best choice for stable nanotube derivatives in biological media. The relaxivities of all the gadonanotube derivatives were lower than that of the original gadonanotube sample. This may be due to alteration of the Gd-clusters as ICP-OES measurements revealed that some Gd^{3+} ion was lost from the gadonanotubes during the rigorous synthetic conditions. Finally, another obvious possibility is the role of surface functionalities on gadonanotube relaxation, which is a variable that is not yet well understood.

We also used this method to attach a cyclic arginine-glycine-aspartic acid (RGD) peptide sequence (specifically, cyclized RGDYK). RGD is a well-known targeting compound, most notably for breast cancer cells, and it has been demonstrated to deliver other nanoparticles successfully to breast cancer tumors.[93,94] The reaction with higher molecular mass compounds such as the cyclic RGD peptide, required a longer reaction time, the coverage was significantly lower, and the resulting gadonanotube-RGD material was nearly insoluble. Due to the low coverage of the RGD, it was possible to also attach smaller solubilizing constituents such as serinol amides (Ser). The gadonanotube-RGD-Ser compound (**V**) was highly soluble (1-2 mg/mL), and contained roughly 0.65-1 RGD units and 8 Ser units per nanometer of gadonanotube (Figure 17). We are currently testing this compound for cellular targeting and uptake on a breast cancer cell line.

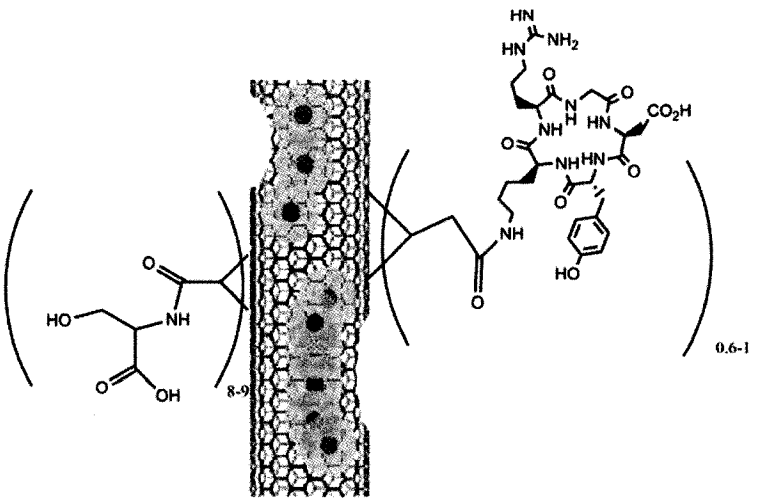

Figure 17: RGD-functionalized gadonanotube, with 8-9 serines and 0.6-1 RGD molecules per nanometer of gadonanotube.

Cell Labeling

Current clinical contrast agents such as Magnevist are unable to cross cell membranes, thus making them poor candidates for molecular MR imaging, which requires internalization and cell accumulation. Several nanostructures have been reported to cross cell membranes and have been used for magnetic labeling of cells for such high-performance applications like *in vivo* stem cell tracking.[62,95] Gadofullerenes ($Gd@C_{82}(OH)_x$ and $Gd@C_{60}[C(COOH)_2]_{10}$) have especially proven to be excellent for labeling cells in high efficiency, so we conducted similar experiments to investigate the ability of the gadonanotubes to also magnetically label cells.

Materials and Methods. Human breast cancer cells (MCF-7) were grown in tissue culture, and then incubated for 24 hours in serum free medium with Magnevist (Mag), gadofullerenols, $Gd@C_{60}(OH)_x$ (Ful), BSA-suspended gadonanotubes (BSA), and serine-functionalized gadonanotubes (Ser), all at equal Gd^{3+} concentrations (0.029 *mM*, 200

μL). This was performed in the presence or absence of the transfection agent protamine sulfate. Previous work with gadofullerenols documented that $Gd@C_{82}(OH)_x$ required a transfection agent,[95] whereas $Gd@C_{60}[C(COOH)_2]_{10}$ did not.[62] Each experiment was performed in triplicate.

Examination of the MCF-7 cells showed no change in viability for any of the treated samples (Figure 18). Following incubation, the cells were lysed from the cell medium with 0.25% trypsin and then thoroughly washed with PBS, pelleted down, the liquid removed and resuspended three times to remove any external contrast agent. The cells were then digested with boiling chloric acid and the Gd^{3+} concentration measured by ICP-OES. The Gd^{3+} concentrations are shown in Figure 19.

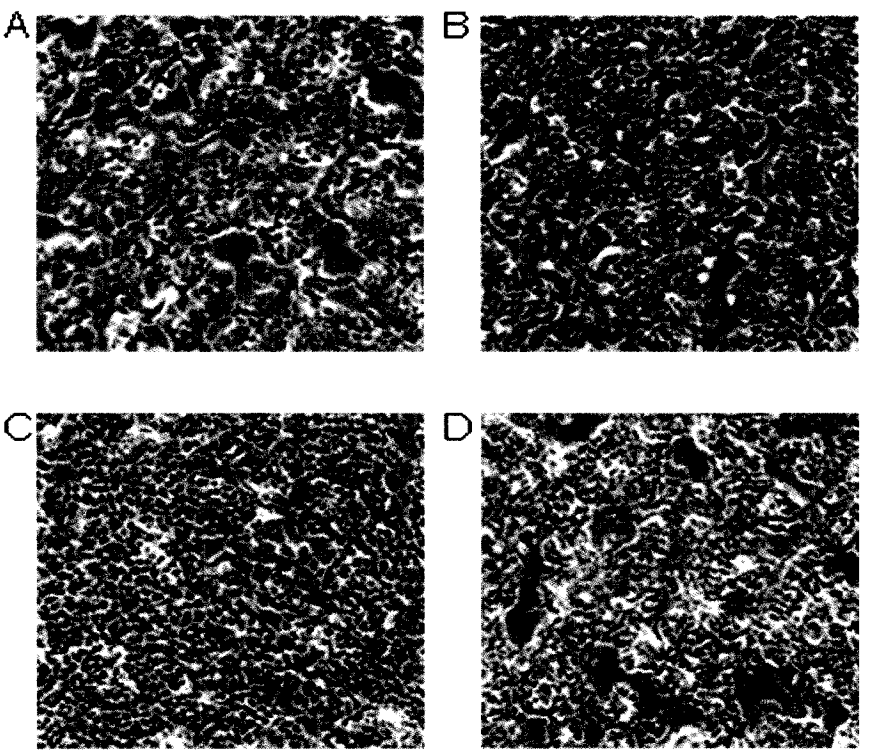

Figure 18: MCF-7 cell viability upon addition of 24 hour incubation with 0.029 mM (A) control, (B) Mag, (C) Ser, and (D) Ful; no change in viability was observed.

Results. ICP measurements confirmed that, as expected, Magnevist was unable to enter the cells. The values for the control and Mag samples are likely zero because these levels were at the limit of detection and the large amounts of salt in the sample from the cells interfere, yielding a false positive. There was minor transfection with BSA-coated gadonanotubes, but the low values are likely due to the large size of the BSA covering which inhibits transfection. In contrast, serine-derivatized gadonanotubes and gadofullerenols were able to enter MCF-7 cells in relatively high concentrations, both with and without the aid of a transfection agent. For the Ser sample, with the aid of the transfection agent, on the order of 10^9 Gd^{3+} ions per cell (65% of administered dose), was internalized by the cells. While carbon nanotubes and $Gd@C_{60}[C(COOH)_2]_{10}$ have been reported to readily cross cell membranes,[55,61,96] $Gd@C_{82}(OH)_x$ was reported to require a transfection agent.[37] It is noteworthy that $Gd@C_{60}(OH)_x$ behaved differently than what has been reported for the $Gd@C_{82}(OH)_x$.

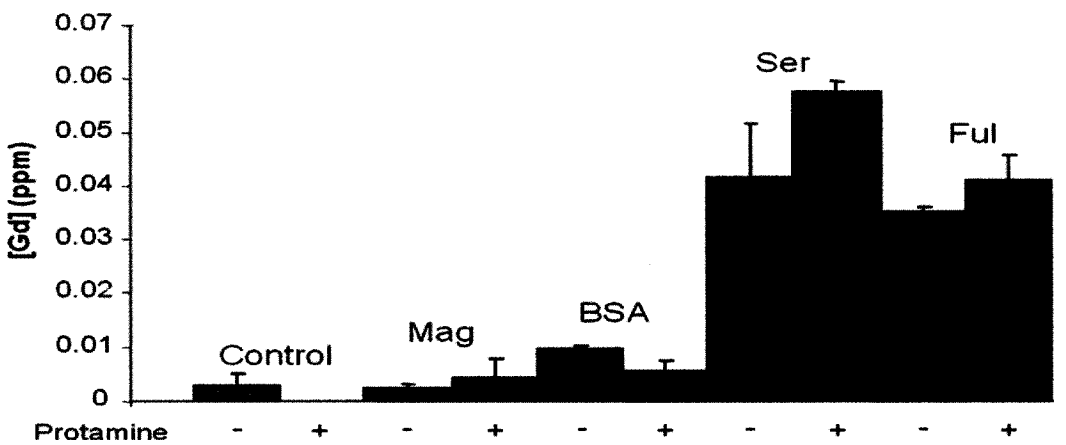

Figure 19: Gd^{3+} cellular uptake as measured by ICP-OES, (-) no transfection agent and (+) with transfection agent.

in vitro Imaging

To investigate the possible application of using these agents as magnetic labels for cellular MRI, their imaging efficacy was tested in an MR imager. Derivatized gadonanotubes and gadofullerenols were both found to transfect and accumulate within breast cancer cells (Figure 19). If they are to be used for high-performance applications such as magnetic cell-labeling, they must maintain their high-relaxivity in biological systems.

Materials and Methods. For the imaging, MCF-7 cells were incubated as described above with Mag, Ser, or Ful. Cells were resuspended in agar and then imaged at 9.4 T. In an attempt to gauge the feasibility of imaging a single cell, attempts were made to discern the fewest number of cells possible to image. Cells were also acid-stripped, removing the outside proteins to ensure that the signal was attributed to internalized CAs. Briefly, the protocol involved centrifuging chilled cells (4 °C), resuspending them in ice-cold acid-strip buffer (50 mM glycine, HCl, 100 mM NaCl, and 2 mg/mL polyvinylpyrrolidone at pH 3.0) for 5–10 min, and washing them twice with cold PBS.

Images were acquired utilizing a 9.4 T, Bruker Avance USR Biospec Spectrometer, 21 cm bore horizontal scanner with a 35 mm volume resonator and BG06 micro-imaging gradient insert. A T_1-weighted FLASH gated MRI sequence was utilized. The imaging parameters to acquire the dynamic contrast enhanced data in Bruker's Paravision 3.2 were as follows: TR = 47.8 ms; TE = 1.8 ms; FOV = 3.0 cm; slices = 8; slice thickness = 1 mm; interslice distance = 3.0 mm; matrix = 512 x 512; NEX = 8. Data was processed utilizing Paravision 3.2 software.

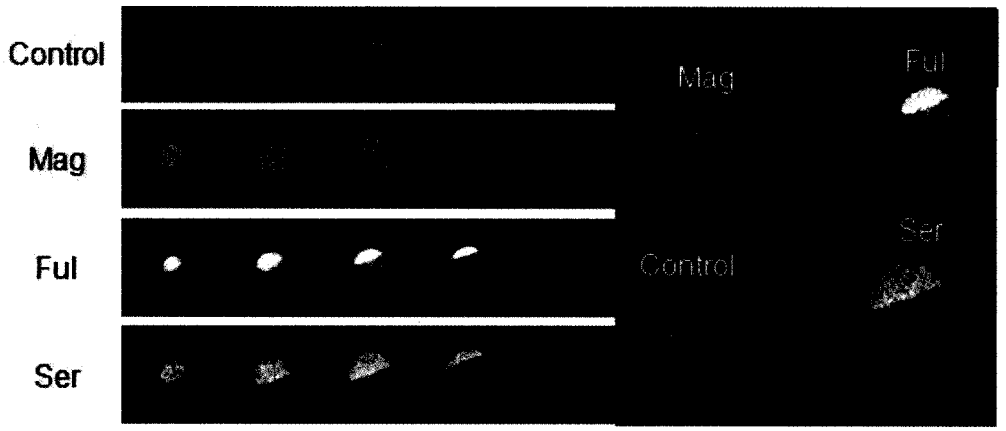

Figure 20: Cell pellets labeled with Ser and Ful demonstrate increased enhancement over Mag which is similar to control. Images are successive slices of the cells pelleted in agar in a tapered Eppendorf tube.

Results. As expected, and confirming our ICP analysis, Magnevist showed no MR contrast enhancement, confirming its inability to function as a cellular labeling agent (Figure 20). In stark contrast, both Ser and Ful labeled cells showed dramatic MRI contrast enhancement. To ensure that the measurement is real, and not due to physisorbed nanostructures on the exterior, the cells were acid-stripped to remove external proteins. This technique is known to remove 95% of proteins from the cell surface.[97] This experiment was repeated several times, and each time, the signal from the Ser sample after acid-stripping increased in intensity (Figure 21). This might be attributed to lower pH in the cell, resulting in increased relaxivity from the gadonanotubes, as described in Chapter II, demonstrating that this important property is maintained in cells. The measured Gd^{3+} concentration was equal to that of the non-acid-stripped sample, confirming internalization of the gadonanotubes.

Attempts were made to image a single cell, but failed due to limitations in the instrument or experimental procedure. While single voxels were imaged, the size of a

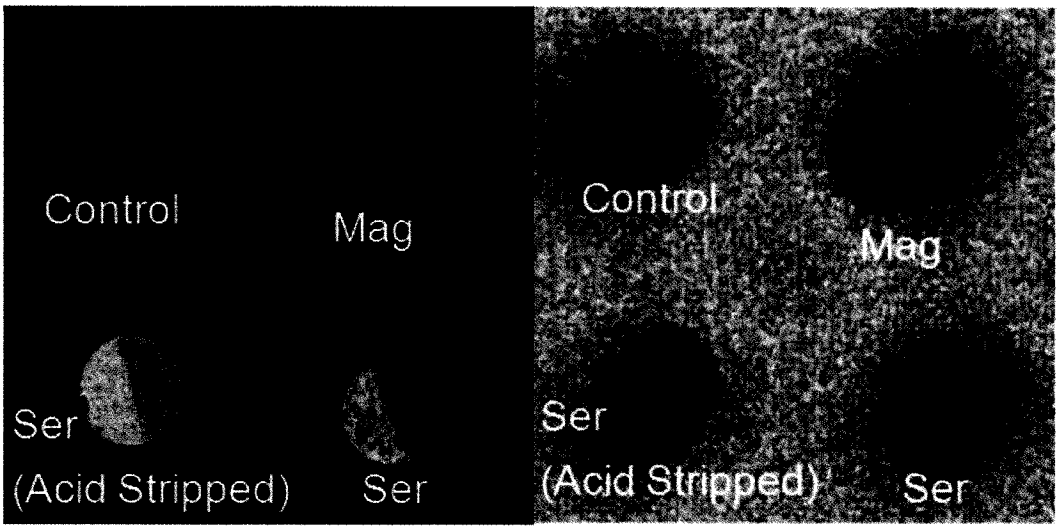

Figure 21: Cell pellets labeled with Ser appear to increase in image intensity after acid-strip treatment. Right image is color-enhanced for better visualization.

voxel (ca. 5 cm^3) is many times the size of a cell. Thus, there may have been multiple cells present. Another difficulty is that bright field images could not be obtained of the agar, thus we could not determine whether cells existed within the illuminated voxel, or whether it was random error. If, as we believe, that illumination from a single voxel was real, then it could be no more than 6 cells. A more conclusive result may be obtained with better cell patterning.

in vivo Imaging

Materials and Methods. All experiments were approved by the Baylor College of Medicine Animal Care and Use Committee. Animals were placed in a prone position on a custom-built head holder with adjustable nose bar and secure ear pins. The respiratory rate was monitored with a pressure pad placed under the animal. Temperature was monitored by use of a rectal probe and maintained at 37 °C using both a water blanket and an air heating system. Vital signs were monitored using the Model 1025 Small

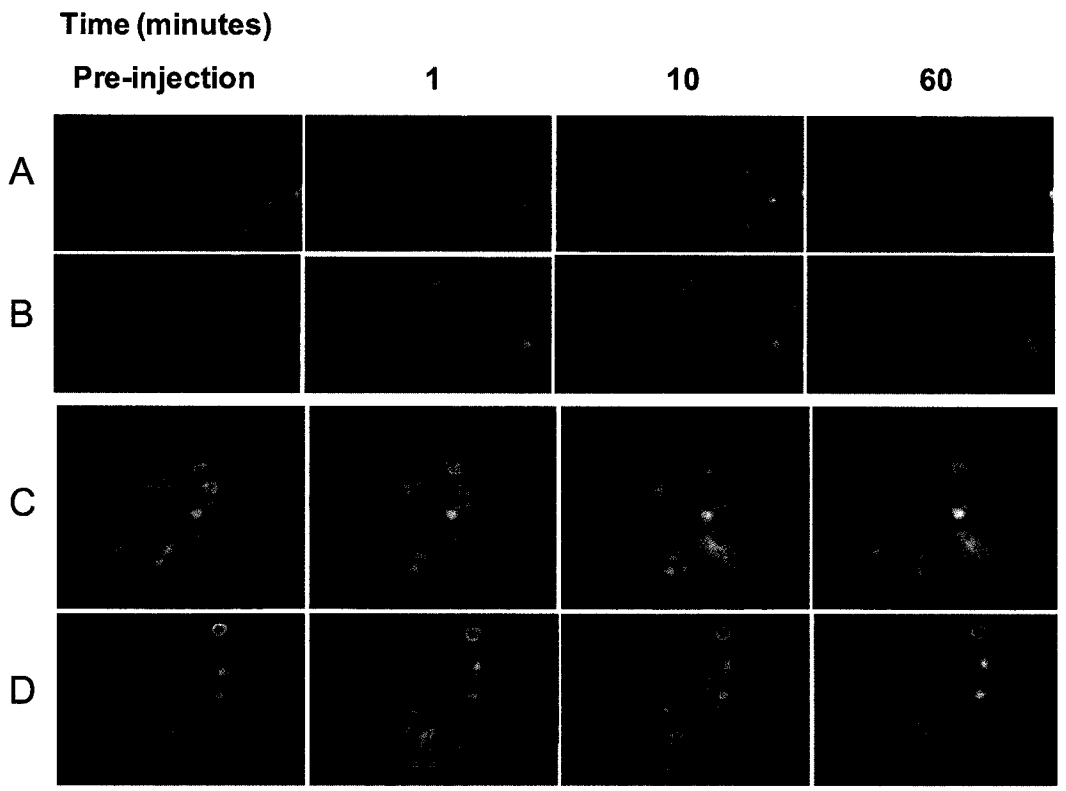

Figure 22: Enhancement in the kidneys (A, B) and liver (C, C) at several time points after the injection of 0.14 mM Magnevist (A, C) or BSA (B, D). The images are calibrated against a water phantom (the large circles in the upper left hand corner of each image).

Animal Monitoring and Gating System software. A tail vein line was introduced for infusion of the contrast agent. Mice were injected with equivalent Gd^{3+} concentrations (350 μl of a 0.14 mM solution) of BSA or Mag and T_1-weighted images were collected sequentially every minute (a phantom image of water was included in every image for normalization). BSA was used because it was the most solubilizing formulation we had in large quantities. Neither spontaneous animal death nor change in animal behavior was observed.

Data was processed utilizing Paravision 3.2 software. For each image, several regions of interest (ROI) were selected and the average of the intensity was normalized

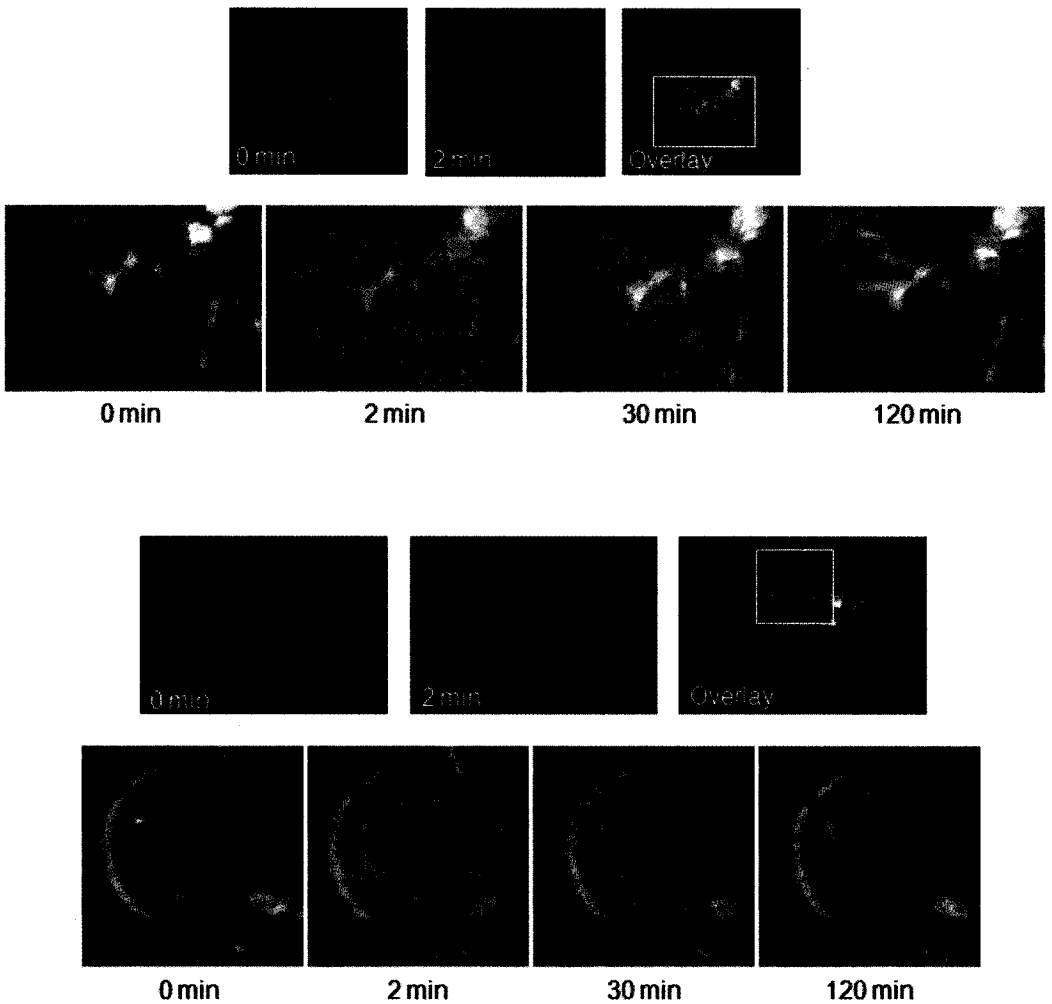

Figure 23: Pseudocoloring of the liver (above) and kidney (lower) at several time points upon the addition of 0.14 mM BSA.

with the intensity of the phantom. The corrected intensity was obtained from the normalized intensity of the pre-injection (Time 0) image subtracted from the normalized intensity at different time points.

Results. Injection of Mag caused a rapid enhancement of contrast in both the kidney (Figure 22A) and the liver (Figure 22C). In the kidney, gadonanotubes caused a similar

enhancement in the outer cortex, presumably representing a concentration of blood vessels with the glomerulus (Figure 22B). In the liver, gadonanotubes caused enhancement of major blood vessels and also caused a 'blush' of enhancement across the liver, presumably representing enhancement of microcapillaries (Figure 22D) similar to the effects caused by Magnevist.

The ability of gadonanotubes to cause enhancement was best visualized using pseudocoloring (Figure 23). Baseline images were colored green and subsequent images red. An overlay indicated no differential signal (i.e. everything yellow) at pre-injection (0 minutes), but 2 minutes after injection of 0.14 mM BSA-gadonanotubes, we observed strong enhancement (red areas) in major blood vessels and capillaries. This signal

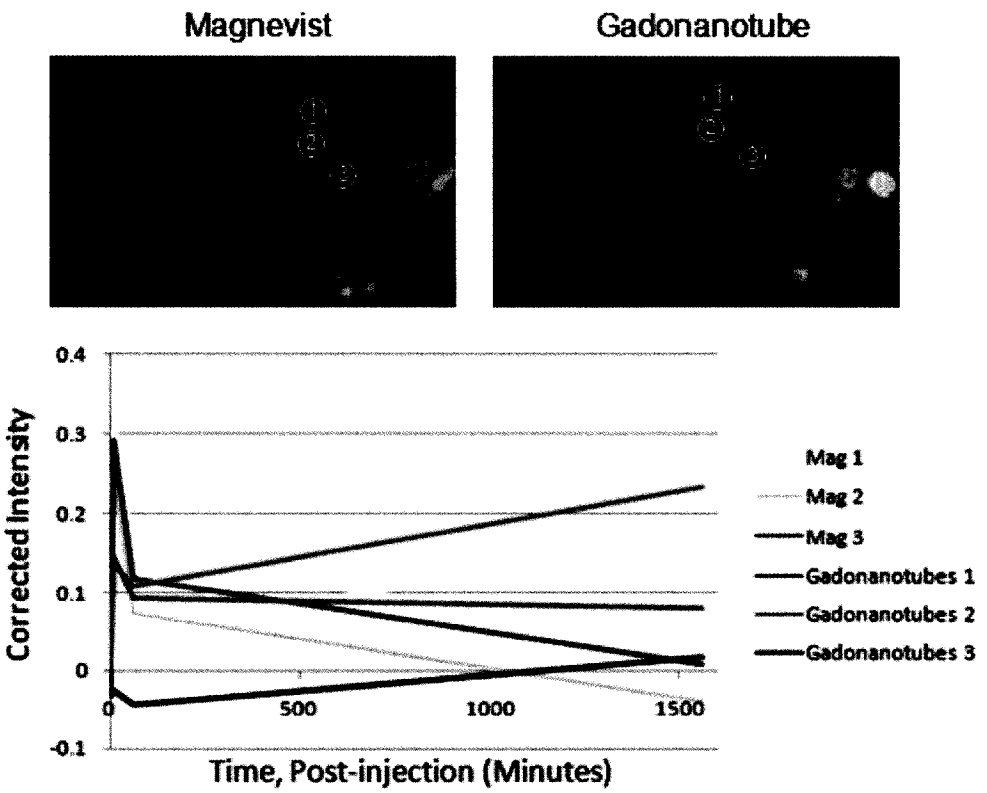

Figure 24: A quantification of contrast enhancement as a function of time for both Mag and BSA in the kidney. Three spots were selected for each image.

dissipated over time and was only slightly visible after 120 minutes. In the kidney, the gadonanotubes initially highlighted the cortex, and interestingly after 120 minutes, the signal was found in the major blood vessels of the cortex, suggesting that the gadonanotubes may be accumulating in this area.

Finally, we quantified the contrast enhancement by measuring pixel density in the MR images (normalized against a phantom image of water included in every scan). We measured intensity in three areas of the kidney (Figure 24) and liver (Figure 25). In the kidney, Magnevist caused a rapid enhancement after 1-5 minutes which then declined to baseline after approximately 24 hours. In contrast, gadonanotubes showed a dramatically

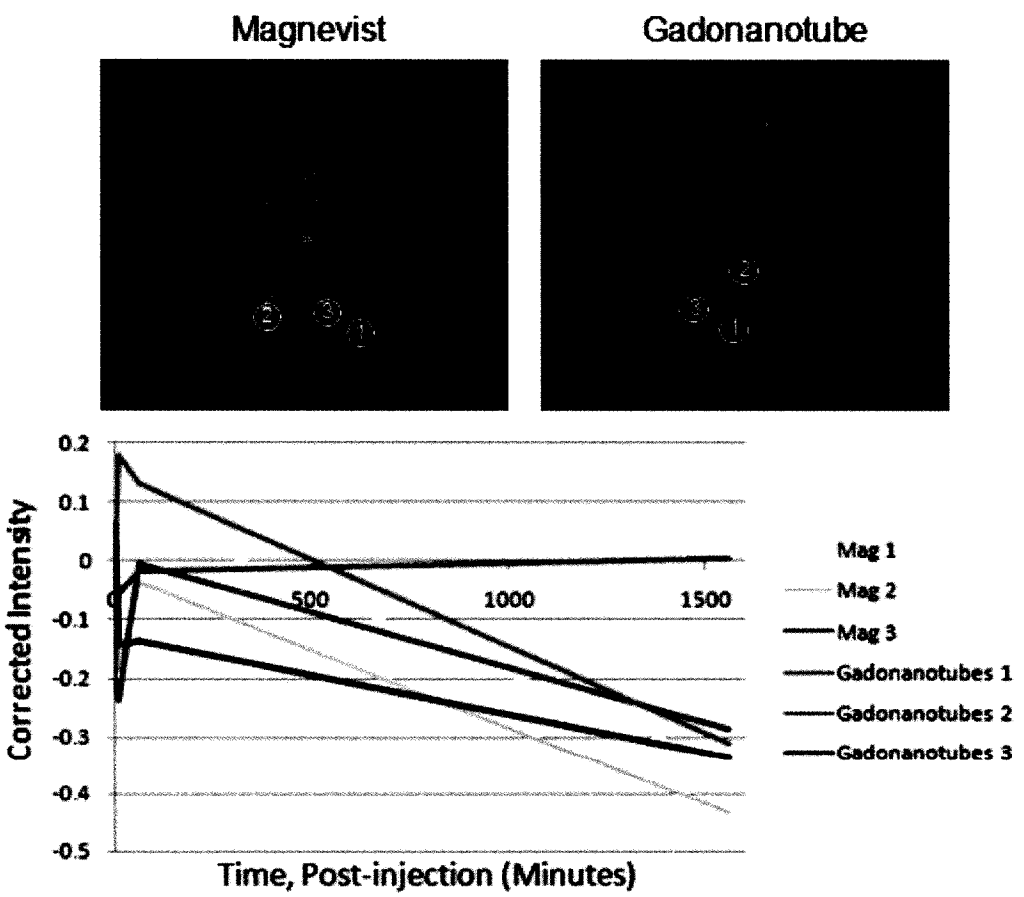

Figure 25: A quantification of contrast enhancement as a function of time for both Mag and BSA in the liver. Three spots were selected for each image.

different enhancement, with rapid and sustained enhancement of the outer cortex, followed by a gradual enhancement of the inner cortex, which was apparent only after 24 hours. In the liver, the area of contrast enhancement was similar between the Mag and BSA samples, although the gadonanotubes persisted longer, suggesting that the gadonanotubes may offer longer enhancement properties. Additional non-calibrated images with intensity quantifications (which demonstrate similar trends for the gadonanotubes) are shown in Appendix IV.

Conclusion

Gadonanotubes have not only demonstrated exciting new nanoscale properties for MRI contrast agent applications, but these materials, even upon functionalization, retain their high-performance relaxivity characteristics in both cells and animals. We have demonstrated the ability to cross-link the gadonanotubes in a PEG micelle with potential for an intravenous MRI contrast agent. Alternatively, for high-performance applications, gadonanotubes can be covalently functionalized with amino acids for solubility and biocompatibility, or with small peptide sequences for targeting, (in this work, RGD for breast cancer cells). Other possibilities for targeting agents include other small peptides, antibodies, or hormones. The water-soluble gadonanotubes are still highly lipophilic and can operate as magnetic cell labels for MRI cell tracking. Preliminary results indicate that the pH influence on relaxivity is maintained inside the cells. Finally, they have been injected into animals and demonstrated their ability to outperform Magnevist *in vivo*. The gadonanotubes have demonstrated differential accumulation and elimination

compared to Magnevist, which may allow them to used for important imaging applications not fulfilled by Magnevist.

CHAPTER IV: US-TUBES AS NANOCAPSULES IN α-RADIOTHERAPY

After cancer has been diagnosed, there are four general treatment strategies that may be employed (sometimes in combination) by oncologists to treat the patient: chemotherapeutics, surgery, antibody treatment, or radiotherapeutics. The most common approach taken in cancer treatment is the administration of chemotherapeutics that are highly lethal to cells (cell toxins). Unfortunately, these drugs kill indiscriminately, so the oncologist must delicately balance the dose ensure that there is enough drug to kill the cancer, but not so much that significant damage is done to other healthy tissue. The two major drawbacks of chemotherapeutic treatment are the heavy toll it takes on the patient's overall health (due to indiscriminate killing of healthy cells), and cancer cells have been known to develop immunity to these drugs over time. Surgery is highly invasive and is limited to large tumors that are accessible. It cannot be used to treat metastatic or small cancers (e.g. leukemia), and it is often difficult to ensure that all the cancerous tissue has been removed from an opened patient. Antibody treatment utilizes the body's own natural immunogenic response to foreign cells (tumors) to treat the disease. While these specialized proteins are specific to only cancer cells, they haven't proved to be the magic bullet that they were claimed to be upon their discovery, mainly because they have low efficacy and have trouble penetrating larger tumors past the first few layers of cells.

Oncologists have long been interested in the use of radioactive isotopes to treat cancers because cancer cells cannot develop immunity to radiation. Typical radiation treatments utilize either α- or β^--particles, emitted from ingested radionuclides.[98] β^--

particles are electrons and require thousands of particles to kill a cell. In contrast, α-particles are helium nuclei (He^{2+}), and due to their greater charge and much larger mass, only a few are required to kill a cell.[99] The main difficulty harnessing this potential treatment is safe delivery of the radionuclide to the area of interest. Typical α-emitting radionuclides are very large and thermodynamically unstable to traditional chelates, resulting in significant loss of the radionuclide. Because radiation damage is indiscriminate, most potential drugs fail because they cannot deliver the radionuclide to the cancerous region without unacceptable damage to healthy bystander tissue.

Recent advances in cellular targeting strategies, such as cell-specific antibodies or small peptides, have increased interest in radionuclides as agents for cancer therapy. Two antibody-targeted radiopharmaceuticals have recently been approved by the United States FDA using β^--emitting radionuclides (^{90}Y and ^{131}I).[100,101] One of the limitations of β^--emitting radiotherapeutics, such as ^{90}Y and ^{131}I, is their unsuitability for the treatment of small clusters of cancer cells (e.g. micrometastatic cancers or single-cell leukemias) because the path length of β^- particle penetration is hundreds of cell diameters, resulting in damage to healthy bystander tissue.[98,102] In contrast, α-particles ($^4He^{2+}$) have much higher linear energy transfer (LET) values and are therefore more lethal over much shorter path lengths, on the order of a few cell diameters. It is estimated that a single α-decay that penetrates the cell nucleus can kill the cell, whereas thousands of β^--decays are required to cause cell death.[99]

Several α-emitting radionuclides have garnered special attention in recent years as radiotherapeutic agents. The four most studied α-emitting radionuclides for radiotherapeutic applications are ^{211}At ($t_{½}$ = 7.2 hours), ^{212}Bi($t_{½}$ = 1 hour), ^{213}Bi($t_{½}$ = 46

minutes) and $^{225}Ac(t_{½}$ = 10 days).[98] While the short half-life of ^{212}Bi and ^{213}Bi can pose significant logistical problems for synthesis, labeling, and delivery, some recent success has been reported with a ^{213}Bi-labeled myeloid leukemia antibody.[103] $^{225}Ac^{3+}$ delivers a cascade of α-particles (4 per $^{225}Ac^{3+}$), however, the three daughter nuclei are extremely difficult to contain upon decay *in vivo* and can result in significant renal toxicity.[104] The long half-life of $^{225}Ac^{3+}$ also poses a significant problem for targeting and retention in the diseased site. Thus, ^{211}At is currently an attractive candidate for the development of α-radionuclide therapy because its half-life is reasonable for targeted delivery, its potential for treatment monitoring by SPECT imaging,[105] and its daughter nucleus, ^{207}Bi (EC; $t_{½}$ = 35 years), is relatively benign (i.e. has low radiation dose). However, the delivery of ^{211}At *in vivo* also has some problems. The carbon-astatine bond is considerably weaker than the carbon-iodine bond and, hence, many ^{211}At-labeled compounds, which exhibit excellent *ex vivo* stability, de-halogenate *in vivo*.[98] Because of these difficulties, nontraditional solutions to the problem of ^{211}At labeling, including carboranes[106] and silver-astatinide nanoparticles[107] have recently been reported.

US-tubes were investigated as a new platform for the containment and delivery of ^{211}At in targeted α-radionuclide therapy for several reasons. Previous work with $^{125}I^-$ found that once US-tubes are loaded with $^{125}I^-$, it could be oxidized to $^{125}I_2$ and strongly retained by the US-tubes (likely as $^{125}I_2$@US-tubes).[108] The $^{125}I^-$ retention half-life of the radioconjugate under flowing water was 2720 hours, however, even more impressive is the fact that with 1 *mM* H_2O_2, the retention half-life was 14,300 hours, or approximately two years. This result suggested that US-tubes might be good candidates to also retain a short-lived α-radionuclide such as ^{211}At (as $^{211}AtCl$@US-tubes or similar species).

Furthermore, the US-tubes possess several other properties that make them desirable as a universal α-TRT delivery platform. The carbon exterior, which is easily derivatized for biocompatibility and cellular targeting (see Chapter III), is relatively bioinert, preventing degradation and thus, radionuclide leakage *in vivo*. Several reports have now demonstrated the proclivity of single-walled carbon nanotube (SWNTs) materials to cross cell membranes and accumulate inside cells,[55,96,109] and cellular internalization of a radionuclide greatly enhances its therapeutic efficacy.[110] No current radionuclide treatment is intracellular, thus making the US-tube platform particularly attractive.

At-211 Labeling of US-tubes

Materials and Methods. US-tubes were synthesized from HiPco-produced SWNTs by the fluorination/pyrolysis method,[73] followed by chemical reduction with metallic potassium in dry THF for the radiolabeling experiments.[75] All experiments involving ^{211}At labeling were conducted at the University of Washington according to approved protocols. ^{211}At was produced by bombarding a ^{209}Bi target with 28 MeV α-particles on a Scandatronix MP-50 cyclotron.[111] Recovery of ^{211}At was carried out in a drybox under vacuum. The ^{209}Bi target was inserted into a tube furnace and heated to 650 °C to isolate ^{211}At by distillation from the ^{209}Bi target as previously described in depth. Briefly, argon gas was flowed through the tube furnace, and the product was collected in a coil of PEEK tubing cooled in a dry-ice bath. ^{211}At was removed from the PEEK tubing by washing with 0.5 mL portions of 0.05 *N* NaOH. ^{211}At extracted under basic conditions will exist in the -1 oxidation state, $^{211}At^-$.[112] The total amount of ^{211}At recovered after distillation and extraction was approximately 4 mCi.

^{211}At labeling experiments were conducted in parallel using using 0.1 mg of US-tubes suspended in either deionized H_2O or MeOH as solvents, with the a reducing agent, either chloramine-T (ChT) in water or N-chlorosuccinimide (NCS) in methanol, as depicted in Scheme II.[113] All experiments were conducted at room temperature. The labeling was conducted in 1.5 mL eppendorf tubes fitted with 0.5 mL centrifuge filters. A general procedure is as follows: The US-tubes were placed in the centrifuge filter with 250 μL of solvent. Next, 25-50 μL of $^{211}At^-$ in NaOH was added (approximately 16 μCi), followed by a 35 μL of the oxidizing agent (either ChT or NCS). If NCS/methanol was used, 2μL of acetic acid (yielding a 1% solution) was added to activate the oxidizing agent. The mixture was allowed to react for ten minutes and vortexed twice at 0 and 8 minutes before centrifugation at 12,000 *g* for 5 minutes with the ^{211}At labeled US-tubes caught on the filter. This solution was saved for γ-counting measurements on a Wallach 1480 Wizard Gamma Counter.

The US-tubes (trapped on the filters) were transferred to a new Eppendorf tube and washed with a 200 μL aliquot of the solvent, briefly vortexed, and centrifuged as described above. The washing was conducted twice, with the two washings collected and combined for γ-counting. The filters were again transferred to a new Eppendorf tube and either 35 μL of metabisulfate (a reducing agent to quench the reaction), 400 μL phosphate buffer solution (PBS), or a solvent wash, and allowed to react for 10 minutes. In the serum challenges, 400 μL of human serum was added and the mixture was allowed to react for 30 minutes. The mixtures were all briefly vortexed at 0 and 8 minutes before centrifugation upon the end of the reaction.

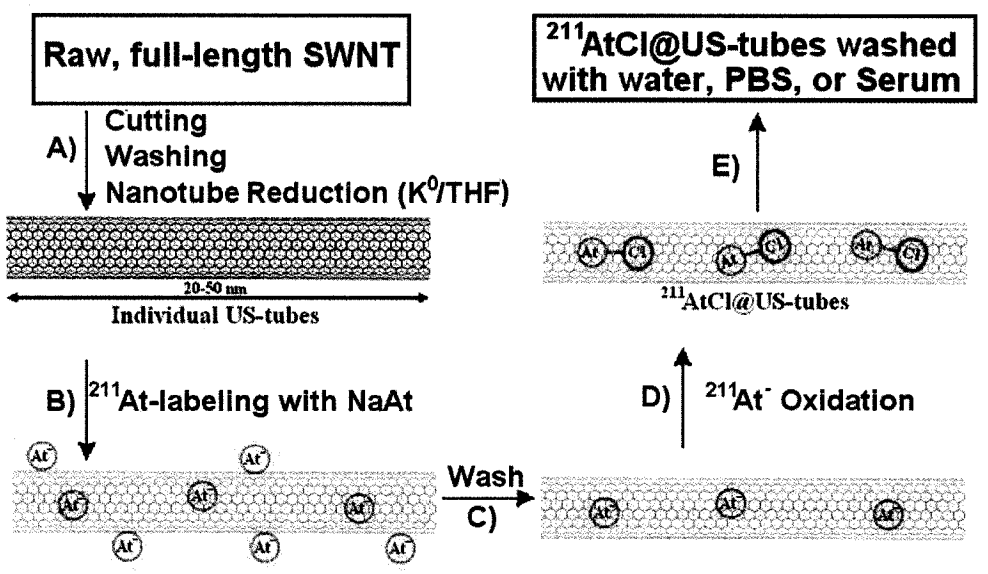

Scheme II: A flow diagram for the preparation and *ex vivo* testing of the ^{211}AtCl@US-tube radiotherapeutic agent.

Results. The first astatine radiolabeling experiments were conducted to determine whether a ^{211}At/US-tube conjugate is more stable when the radionuclide is present in the anion form ($^{211}At^-$) or as the mixed halogen (^{211}AtCl), which is a well-known stable compound.[114] $^{211}At_2$ is not likely to form since the amount of ^{211}At present is so small (36 femtomoles) which is several orders of magnitude less than the level of most contaminants (Cl^- from the oxidant, solvent, etc). Previous work with $^{125}I^-$ found half-life removal times of 2720 hours for $^{125}I^-$ and 14,300 hours for $^{125}I_2$.[108] The huge increase in retention of $^{125}I_2$ compared to $^{125}I^-$ is believed to be due to greatly enhanced van der Waals interactions between I_2 and the interior of the US-tube sidewall as compared to I^-.

After the US-tubes were labeled and washed, the initial radiolabeling (the amount of $^{211}At^-$ retained by the tubes) was relatively poor: 24.7% in water and 13.1% in methanol (Table III).[113] In contrast, when an oxidizing reagent (chloramine-T or N-

Table III: The effect of ^{211}At oxidation state on the radiolabeling of US-tubes.

Oxidation State	Solvent	Oxidant	Initial Labeling (%)	Wash (% remaining)	Overall Labeling (%)
$^{211}At^-$	H_2O	None	24.7 (14.0)	79.7 (1.0)	19.6 (10.9)
^{211}AtCl	H_2O	ChT	91.3 (8.5)	66.5 (12.9)	60.7 (14.0)
$^{211}At^-$	CH_3OH	None	13.1 (4.6)	77.6 (4.0)	11.0 (5.2)
^{211}AtCl	CH_3OH	NCS	77.7 (11.4)	69.8 (15.4)	55.4 (19.0)

ChT: Chloramine-T; NCS: N-chlorosuccinimide; four and three replicates for the ChT and NCS oxidized tubes, respectively; two replicates for the non-oxidized tubes; data is displayed as an average value with the standard deviation in parentheses.

chlorosuccinimide) was added before the washing, the resulting ^{211}AtCl molecules labeled the US-tubes to a much greater extent, 91.3% and 77.7% for water and methanol, respectively, as similarly observed for the $^{125}I^-$ /$^{125}I_2$ pair.[108]

While ^{211}AtCl has a high affinity for individual US-tubes, there is likely a small quantity of agent located at exterior US-tube sidewall defect sites or tube ends, which can be removed upon washing with metabisulfite (used to quench the reaction by reducing any accessible ^{211}AtCl to $^{211}At^-$) as shown in Table III.[113] As a result, overall retention of ^{211}AtCl by the US-tubes upon oxidation and washing to produce ^{211}AtCl@US-tubes is 60.7% and 55.4% for water and methanol, respectively. When the $^{211}At^-$ is not oxidized to the mixed halogen, but rather allowed to remain in anionic form, the labeling (following washing) was drastically reduced to only 19.6% and 11.0% for water and methanol, respectively. The overall labeling yields of the ^{211}AtCl@US-tubes are very encouraging considering that the labeling procedure is not yet optimized but is comparable to many astatine compounds in the literature: 23-41% for biotin derivatives,[115] 23-57% for carborane derivatives,[106] and 40-60% for benzoate-antibody conjugates.[116]

Physiological Simulations

In an attempt to better simulate *in vivo* conditions, a series of PBS washings and a serum challenge were conducted at room temperature. After labeling, the ^{211}AtCl@US-tubes were washed twice with PBS, resulting in the retention of 72-85% of the radionuclide, and upon challenge with human serum, 85-93% was retained post-exposure (Table IV).[113] This observed loss may be due to easily removed ^{211}AtCl residing at sidewall defect spaces or tube ends. An alternative explanation is that upon α-decay, the decay products puncture the nanotube, and some interior radionuclide is lost during washings, thus indirectly lowering the ^{211}AtCl retention percentages. Nevertheless, these results demonstrate that ^{211}AtCl@US-tubes exhibit reasonable stability toward physiological challenge.

Table IV: Washings and Serum Challenge Experiments with ^{211}AtCl@US-tubes

Solvent	Oxidant	Initial Labeling (%)	1st Wash (% remaining)	2nd Wash (% remaining)	Serum (% remaining)
H_2O	ChT	30.0 (0.2)	85.4 (1.3)	81.0 (1.9)	85.5 (3.4)
CH_3OH	NCS	37.4 (2.2)	78.3 (3.2)	72.4 (5.0)	93.1 (0.6)

Two replicates were conducted in each experiment.

Inside or Outside?

Finally, an important question that still lingers is whether the ^{211}AtCl-labeling molecules are truly inside the US-tubes or are merely physisorbed to the tube exterior. To help answer this question, we have simulated the astatine labeling experiments using I_2 as an appropriate halogen substitute for ^{211}AtCl. Under these aqueous loading conditions, it has been well documented that oxidation by chloramine-T does not form

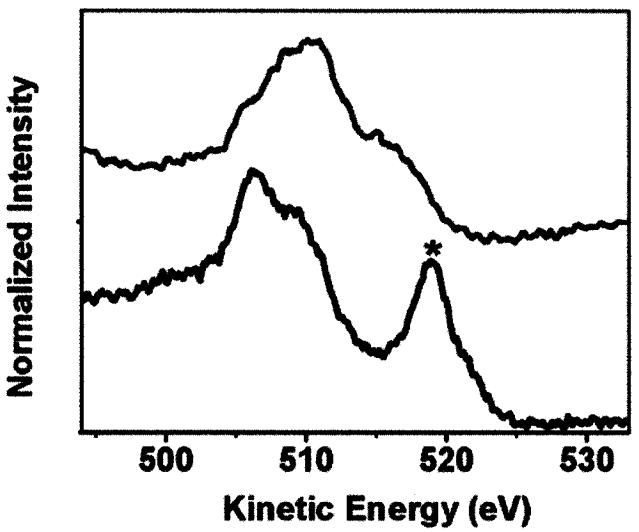

Figure 26: The peak at ~519-520 eV in the black trace (lower) has physisorbed exterior iodine. In the red trace (upper), the exterior iodine has been removed and the 520 eV peak is missing. The I_2@US-tube spectrum (Figure 2) clearly lacks a peak at ~520 eV, so no exterior I_2 is indicated.

ICl, but rather the product is present as I_2.[117,118] This has been done because, taken together, X-ray photoelectron spectroscopy (XPS) and X-ray-induced Auger emission spectroscopy (XAES) have the ability to prove the presence of I_2 and to discriminate between interior-loaded I_2 and exterior physisorbed I_2 for carbon nanotube materials.[119] XPS and XAES data were collected on US-tube samples, pressed onto indium foil, using a PHI Quantera spectrometer.

Aqueous I^- loading experiments were performed for both US-tubes and SWNTs, following the same procedures as used for $^{211}At^-$ loading, washing, and oxidation in water but with NaI as the source of I^-. Analysis by XPS found significant I_2 loading for the US-tube sample (1.5-3.0 atomic % iodine). In contrast, no loading of iodine occurred for the full-length SWNT sample. This is as expected since the SWNT ends are closed and there are no sidewall defects. A complementary technique to XPS, XAES can establish whether I_2 is loaded inside the nanotube or physisorbed to the exterior sidewall.[119,120]

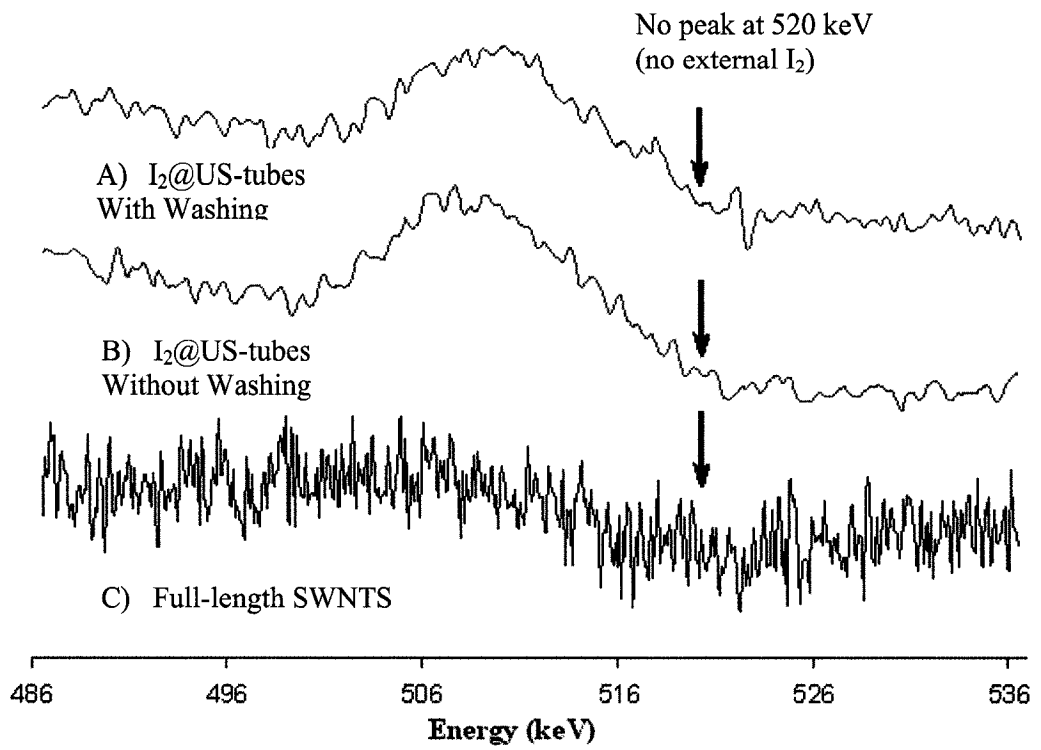

Figure 27: X-ray-induced Auger emission spectrum of (A) full-length SWNTs (B) iodine-loaded US-tubes with no solvent wash prior to oxidation (C) iodine-loaded US-tubes with a solvent wash prior to oxidation. The full-length SWNTs failed to load with I_2, as expected.

Previous work has demonstrated that physisorbed I_2 to the nanotube exterior will have a high-energy shoulder at 520 keV, as shown in Figure 26. The Auger emission spectrum for the aqueous I^- and ChT oxidation is shown in Figure 27. This clearly demonstrates that I_2 is exclusively loaded inside the US-tubes since any exterior adsorbed I_2 would exhibit a high-energy shoulder at 520 keV, which is clearly absent in both the Figure 27B or 27C spectra. The Figure 27C trace is a sample of US-tubes that was washed with solvent prior to oxidation, while the Figure 27B trace is a sample that was not washed with solvent prior to oxidation. The full-length SWNT sample in the Figure 27A spectrum clearly failed to load I_2 at all. These data establish that loading of debundled (individual) US-tubes with aqueous I^-, and subsequent oxidation, results in exclusive

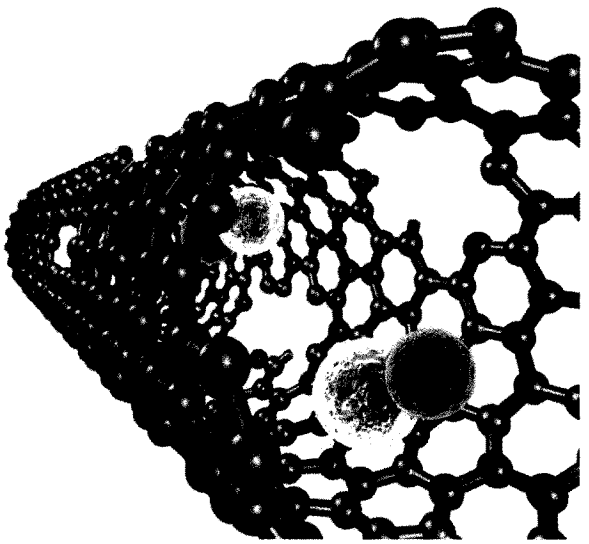

Figure 28: A pictorial representation of the ^{211}AtCl@US-tubes.

internal loading of I_2, and solvent washing of the resulting I_2@US-tube product does not remove spectroscopically-detectable amounts of I_2. It is reasonable to assume that ^{211}AtCl@US-tubes prepared in the same manner would also have all ^{211}AtCl internally loaded, as depicted in Figure 28. For astatine, ^{211}AtCl is expected to form in the US-tubes (with oxidation by Ch-T or NCS) instead of $^{211}At_2$ because the initial concentration of $^{211}At^-$ is so very low.

Conclusion

This work has demonstrated the use of US-tube materials as a new paradigm in radionuclide containment. By utilizing non-covalent van der Waals interactions between ^{211}AtCl and the interior sidewalls of the US-tubes, we have produced a promising candidate for α-radionuclide containment and delivery in medicine. While the main advantage of this carbon nanotube technology is likely to be for α-radionuclides where *in*

vivo retention is most problematic, β^--radionuclide therapies might also benefit. In the present case, the test as to whether ^{211}AtCl@US-tubes will serve as a viable α-TRT for α-treatable cancer must await the development of targeted US-tube-antibody constructs similar to that recently reported for a fullerene (C_{60}) immunoconjugate.[70] Alternative possibilities may include small peptide targeting (e.g. RGD for breast cancer, etc.)[93,94] or brachytherapy (direct implantation of the radioconjugate into the tumor).[121,122] As these US-tube capsules have been demonstrated to readily internalize inside of cells, the ability to shuttle their internal radionuclide cargo inside the cells, thus making them many times more lethal by placing the radionuclide closer to the nucleus, is very exciting.

This project, coupled with the previous project using gadonanotubes as a diagnostic agent, demonstrates the ability of the US-tubes to function as a universal imaging and therapy platform in the development of nanomedicine. The US-tubes need not be limited to a single entity inside the tube, but both elements could be combined to yield a simultaneous therapeutic and diagnostic (or "theranostic") agent. A combination Gd^{3+} and ^{211}At agent would operate as a magnetically-guided therapy, directed to the cancer site by attachment of a targeting agent.

CHAPTER V: AN ACUTE TOXICITY STUDY OF CARBON NANOTUBES IN MICE

Carbon nanotubes have clearly demonstrated their potential for medical applications, both here and elsewhere. However, as with any new platform technology proposed for medical applications, potential toxicity must be investigated as the technology develops. Nanomaterials, in particular, must be carefully evaluated because of their large surface areas. Thus far, many of the toxicity studies for carbon nanotube materials (both *in vitro* and *in vivo*) are conflicting, fragmentary, and subject to criticism. Many of the conflicts associated with these studies are related to the unique properties of carbon nanotubes, primarily their insolubility, their tendency to aggregate, and the presence of metal catalyst impurities which make them difficult to handle.

Some recent *in vivo* studies have focused on the pulmonary toxicity of SWNTs.[123-125] The toxicity of SWNTs is mainly characterized by a granulomatous reaction, however, the interpretations are contradictory.[126] For some authors, SWNTs are more toxic than quartz nanoparticles,[123,124] while for other authors, the granulomatous reaction is a nonspecific response to instillation of SWNT aggregates which may not have physiological relevance.[125] Subcutaneous implantation of SWNTs in mice also induced granuloma formation, however, the toxicity was certainly lower than that of asbestos.[127] Although two studies have also recently examined the biodistribution of CNTs by using intrinsic SWNT fluorescence[52] or ^{13}C-enriched SWNTs and isotope ratio mass spectroscopy,[128] these studies used doses too low (20 μg/kg - 200 μg/kg of body weight (bw)) and/or observation times too short (24 hours) to be of toxicological relevance.

Here, we have completed the first *in vivo* toxicity study of SWNTs in mice, assessing the acute toxicity, the biological fate, and the persistence/elimination after intraperitoneal (i.p.) administration of very large doses (up to 1g/kg bw) of two different types of HiPco SWNTs, raw (r-SWNTs) and purified (p-SWNTs) full-length SWNTs, and US-tubes. The r-SWNTs are 300 nm to several micrometers long and contain ca. 25% residual iron catalyst, while p-SWNTs are less than 4% iron by mass. US-tubes are 20-80 nm in length with less than 1.5% iron by mass, and compared with r- or p-SWNTs, US-tubes have many defects in the sidewalls due to the chemical cutting process.

Materials and Methods

Sample Preparation. Raw, full-length, single-walled HiPco carbon nanotubes (r-SWNTs) were obtained from Carbon Nanotechnologies, Inc. The r-SWNTs are 300 nm to several micrometers long, have diameters of ca. 1.0 nm, and contain ca. 25% residual iron catalyst by weight.[129] The r-SWNTs were chemically cut into US-tubes via fluorination and pyrolysis as described in Chapter II. The US-tubes were then bath sonicated in concentrated HCl for 30 minutes, followed by filtration and a DI water washing to remove amorphous carbon and iron catalyst impurities. The purified US-tubes are <1.5% iron by mass.

Aqueous suspensions of CNTs were prepared as previously described for C_{60} aqueous suspensions,[130,131] by alternate stirring and sonication in a 0.9% aqueous NaCl solution or in the same solution containing 0.1% polyoxyethylene sorbitan monostearate (Tween 60) and for some experiments 0.2% or 2% carboxymethylcellulose (CMC).

After sterilization by autoclaving for two hours at 120 °C, the resulting suspensions were administered intraperitoneally into mice (1 mL/mouse).

According to single-dose toxicity practical guidelines, a test compound should be administered to animals to identify doses causing no adverse effects and doses causing major (life-threatening) toxicity. For compounds with low toxicity, the maximum feasible dose should be administered. In the case of rodents, at least one route of administration should ensure full access of unchanged substance to the circulation. Because CNTs are prone to aggregate in polar media, the i.v. administration of large doses can lead to mechanical blockage of the vasculature system. Thus, intraperitoneal (i.p.) injection is the only possible route of administration that can ensure access to the circulation for high doses of CNTs suspended in a biocompatible medium. This method of administration has been used to inject up to 5 g/kg of body weight (bw) of suspended C_{60} into rodents.[130,131]

in vivo Studies and Biochemical Tests. Animals received human care and the study protocols complied with Université Paris-Sud 11, Paris, France, guidelines for the care and use of laboratory animals. Pathogen-free male Swiss mice (20 ± 2 g, Charles River, France) were housed in groups of three in individual polypropylene metabolic cages enabling urine and excrement collection at constant temperature (22 °C) and humidity (60%) and with a 12 hour light/dark cycle. The mice were fed a standard diet *ad libitum*. All mice were allowed to acclimate to this facility for at least one week before being used in the experiments.

The animals were sacrificed at Day 1 (D_1), D_2, D_7 and D_{14}, after body weight determination by bleeding through the thoracic aorta after sodium pentobarbital (1.0 mL/kg of body weight) anesthesia. Small, fresh pieces of the spleen and the right lobe of livers were fixed with pH 7.4 phosphate-buffered 10% formalin and were processed by embedding in paraffin. Liver histology was evaluated using hematoxylin and eosin or Masson's trichrome staining. Samples for high-resolution transmission electron microscopy (HRTEM) examination were processed as described previously.[131] Serum alanine aminotransferase (ALT) activities were determined using a Hitachi 911 Analyzer as described previously.[131]

Excretion Studies and Microscopy Analysis. Two mL of urine were mixed with 2 mL of 5M saccharose aqueous solution. The mixture was first vortexed for 2 minutes and then stirred for 12 hours. Afterwards, it was subjected to alternate sonication (15 minutes) and vortexing (2 minutes) five times. The resulting mixture was then centrifuged at 1000 *g* for 10 minutes and the supernatant was re-centrifuged at 3000 *g* for 30 minutes. The pellet was then washed twice with distilled water by alternating redispersion and centrifugation at 3000 *g* for 30 minutes.

The final pellet was prepared for HRTEM by redispersion in 200 μL of water (10 minutes of bath sonication). 3 μL of the resulting suspension were deposited onto an ionized 400 mesh copper grid. After 5 minutes, the excess of the suspension was absorbed by a slow filtration filter paper.

About 0.5 g of feces were rinsed with 2 mL of water and soaked in 3 mL of water. After adding 10 mL of a 0.1 M Tween 60 aqueous solution, the mixture was

homogenized by stirring in an Ultra Turax. The final mixture was then treated twice by alternating sonication (30 minutes) and stirring (24 hours). After decanting (30 minutes), the supernatant was further centrifuged at 3000 *g* for 30 minutes. The pellet was then washed twice with distilled water by redispersion and centrifugation at 3000 *g* (30 minutes). The final pellet was prepared for HRTEM by redispersion in 500 μL of water (sonication during 10 minutes). 3 μL of the mixture were deposed onto an ionized 400 mesh copper grid. After 5 minutes, the excess of the suspension was absorbed by a slow filtration filter paper.

Experiment I: *in vivo* Toxicity of SWNTs Suspended in Aqueous Media

Animal Behavior and Pathological Examination. In a first experiment (Experiment I), 42 mice (weighing 20 ± 2 g) were randomly divided into seven groups of six mice each and subjected to an i.p. injection of 1 mL bolus of CNTs suspended in 0.1% Tween 60, 0.2% CMC, and 0.9% aqueous NaCl solution at increasing doses (50, 250, and 500 mg/kg bw). Because we were interested only in exploring the toxicity and the fate of the maximum amount of administrable-sized aggregates of the materials, no effort was made to obtain individualized CNTs. Group 1 received only the vehicle, groups 2 to 4 received the r-SWNT suspensions, while groups 5 to 7 received the US-tube suspensions. The animals were kept under observation until D_{14}.

No spontaneous death occurred during the experiments, and the growth of all the animals was not different from that of the control group (Figure 29). Mice treated with all the r-SWNT doses and the lowest US-tube dose (50 mg/kg bw) showed no overt clinical signs or behavioral trouble. The animals treated with the doses of US-tubes equal

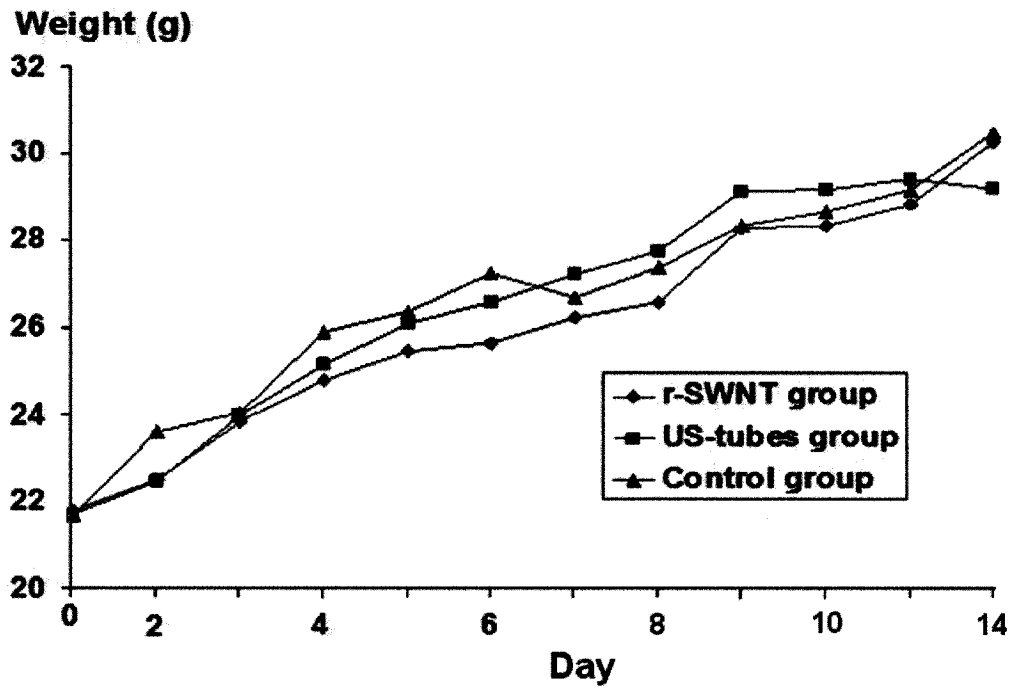

Figure 29: Animal growth after single-dose administration of r-SWNTs (500 mg/kg bw) or US-tubes (1 g/kg bw). Each point represents the median of 6 animals. The CVs were 4.6%, 7.4%, and 7.0% for the control group, the US-tube group, and the r-SWNT group, respectively.

to or higher than 250 mg/kg exhibited inactivity, lethargy, and piloerection. These symptoms persisted until the animals were sacrificed for histopathological examination. As the animals treated with r-SWNTs had no apparent signs of toxicity, we stopped the observation at D_{14} in order to compare the effect of the two kinds of CNTs.

Pathological examination of the r-SWNT-treated mice and those of the animals treated with the lowest US-tube dose (50 mg/kg) showed normal organ morphology with a few small deposits of the injected material on the organ surfaces (Figure 30A). The organs of the animals treated with the high US-tube doses were covered with some deposits of the injected material and showed different abnormalities as a function of the dose. Among the mice treated with 250 mg/kg of US-tubes, one exhibited a rounded

Figure 30: Photographs of the abdomens at D_{14} of (A) r-SWNT-treated mouse, (B) US-tubes suspended in 0.1% Tween 60, 0.2% CMC, and 0.9% NaCl (Experiment I), and (C) US-tubes suspended in 0.9% NaCl (Experiment II). The arrows indicate the greyish film of cell infiltrate.

liver while in a second mouse, the liver, spleen, and the intestine were adherent; however, the organs could be easily separated. In the group treated with the highest US-tube dose (500 mg/kg bw), the organs (livers, spleens, stomachs, and intestines) of most of the animals (4/6) were adherent and covered with several large deposits of the injected material (Figure 30B). In two cases, the deposits of the injected material were covered by a thin film of cell infiltrate (Figure 30B). Thus, at the macroscopic level, US-tubes at high doses are toxic while r-SWNTs are not.

Optical Microscopy. Microscopic examination after eosine-hematoxyllin staining of the liver and spleen sections of US-tube-treated animals revealed severe, foreign-body reactions characterized by multifocal epitheloid granulomatous lesions both inside and on the surface of the organs (Figure 31A and 31B). This is similar to that observed in previous studies, both in lungs[123,125,132] and in subcutaneous tissues.[124] If the granulomas

Figure 31: Light micrographs after hematoxylin-eosin staining of liver and spleen sections from mice intraperitoneally injected with a single dose (500 mg/kg) of full-length (r-SWNTs) or ultra-short (US-tubes) single-walled carbon nanotubes suspended in 0.1% Tween 60, 0.2 % CMC, and 0.9% NaCl aqueous solution, at 14 days post-administration. (A) Focal granulomas (arrows) containing foreign body giant cells inside a liver lobe. (B) Granuloma on the surface of the spleen of a r-SWNT-treated mouse. (C) Granuloma between a hepatic lobe (bottom) and an intestine tissue (left) of a US-tube-treated mouse. Note the absence of fibrosis around the granulomas. (D) High magnification of an US-tube-laden foreign body giant cell (black arrow) inside a liver lobe. (E) Granuloma coming off the surface of the spleen of a r-SWNT-treated mouse. (F) Small granulomas (arrows) inside the hepatic lobe of a mouse treated with US-tubes suspended in 0.1% Tween 60, 0.9% NaCl solution at D_7. Magnification = 20x for A, C, E, F, 5x for B, and 40x for D.

are large, they can act as glue between the organs (Figure 31C) which explains why adherent organs were observed in some cases. The granulomatous lesions are mainly formed by foreign body type giant cells[133] laden with US-tube particles (Figure 31D). In the group treated with r-SWNTs, there were also granulomatous lesions, however, they were very limited in number and size, and they were mostly localized on the surface of

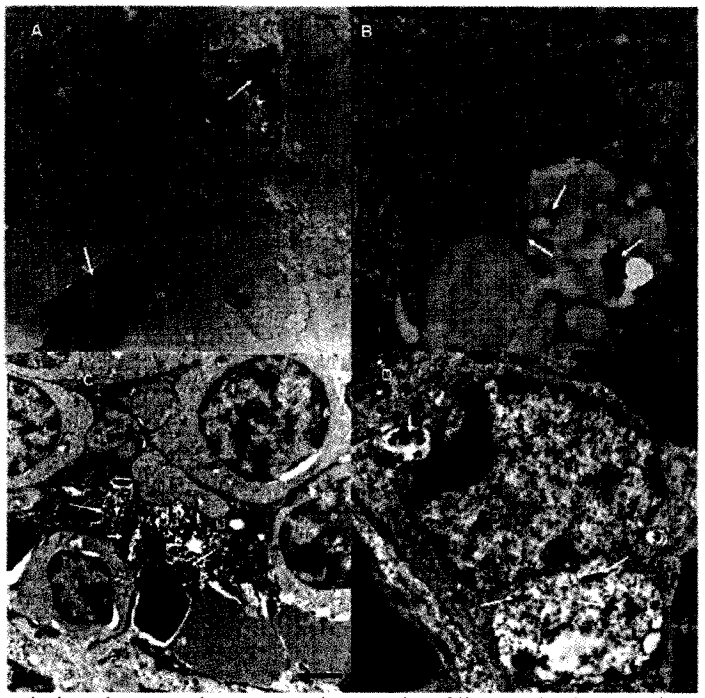

Figure 32: Transmission electron microscopy micrographs of liver and spleen sections of CNT-treated mice. US-tubes agglomerates (arrows) inside (A) a giant cell, (B) r-SWNT agglomerates inside an Ito cell, (C, D) spleen macrophages.

the organs where there were deposits of the injected material. While r-SWNT deposits could be easily removed from the organ surfaces (Figure 31E), the US-tubes aggregates could not be removed because they were strongly bound to the organ surfaces (Figure 31B). In all cases, the granulomatous lesions were, as expected,[133] associated with the degree of agglomeration of the injected material which supports the results of recent *in vitro* studies linking the toxicity of CNTs to their degree of aggregation.[134]

Transmission Electron Microscopy. Figure 32 shows the electron micrographs of liver and spleen sections of an US-tube-treated mouse. Inside both organs, the US-tube bundles were mostly localized within the granulomatous lesions (Figure 32A). Inside the liver, they accumulated within Kupffer cells and, in a very few cases, inside Ito cells

(Figure 32B), similar to that which occurs for C_{60} particles.[130,131] However, the US-tubes were never observed inside the hepathocytes, as in the case of C_{60}. Inside the spleen, the r-SWNT bundles were internalized by macrophages (Figure 32C). Inside vacuole-containing cells, the SWNT materials were always located near the nucleus (Figure 32B and 32D).

Biochemical Markers. The circulating levels of the alanine amino-transferase activities (ALT), used as markers of hepatolysis, increased for both the US-tubes and r-SWNTs relative to the control (Figure 33A); however the activities were higher in the US-tube-treated group than in the r-SWNT-treated group (2.5 and 1.5 times higher than the control group, respectively). It is worth noting, however, that this increase of ALT activity is relatively small compared to other well-known hepatotoxicants.[130] For example, carbon tetrachloride raises the ALT activity to ca. 3500 IU/L, nearly an order of magnitude greater than the r-SWNTs.

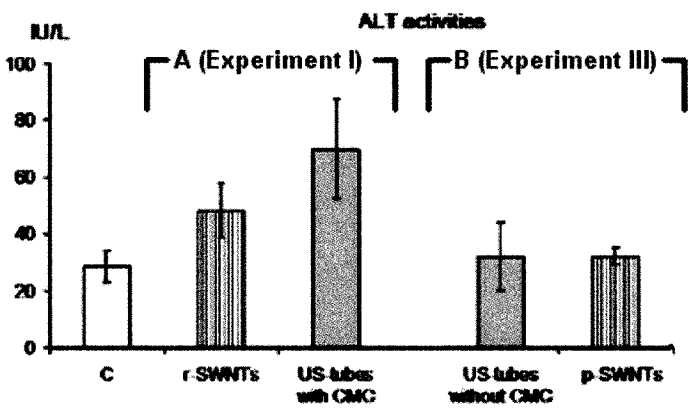

Figure 33: Effect of a single dose (500 mg/kg bw) CNT-treatment on serum ALT activity of mice ($n = 6$). (A) Animals treated with US-tubes or r-SWNTs suspended in 0.1% Tween 60, 0.2% CMC, and 0.9% NaCl aqueous solution at D_{14} after administration (Experiment I). (B) Animals treated with US-tubes suspended without 2% of CMC, or with p-SWNTs, at D_7 after administration (Experiment III).

Experiment II: Intrinsic Toxicity of SWNTs

In a second experiment (Experiment II), to better assess the intrinsic SWNT toxicity, highly concentrated aqueous formulations of US-tubes (20 mg/mL) and r-SWNTs (10 mg/mL) were prepared without adding dispersion agents. As it is more difficult to disperse the r-SWNTs than the US-tube aggregates, the r-SWNT concentrations were limited to 10 mg/mL.

Thirty-six mice (weighing 20 ± 2 g), randomly divided into six groups of six mice each, received an i.p. injection of a 1 mL bolus of US-tubes at increasing doses (50, 500, and 1000 mg/kg bw), r-SWNTs (50 and 500 mg/kg bw), or 1 mL of the 0.9% NaCl solution vehicle (control group). At D_{14}, all the animals were sacrificed for pathological examination. No spontaneous death occurred during the experiment, and the growth of the treated animals was not different from that of the control group. Nevertheless, the animals treated with US-tube doses equal to or higher than 500 mg/kg of body weight exhibited the same symptoms of inactivity, lethargy, and piloerection as in Experiment I (above).

After anesthesia and abdomen incision at D_{14}, the organs of the r-SWNT-treated mice and those treated with the lowest US-tube dose showed the same features as those treated with the same doses in Experiment I. In contrast, the organs (liver, spleen, stomach, and intestine) of most of the animals treated with the higher US-tube doses (4/6 and 5/6, respectively) were adherent and covered with several large deposits of the injected material, together with a grayish film of cell infiltrate which was most pronounced for the animals treated with the 1 g/kg bw dose (Figure 30C).

Experiment III: Removing the Iron Catalyst and Controlling the Surface Structure

As the r-SWNTs used in Experiment II contained high levels of metal catalyst, we also carried out a third experiment (Experiment III) using p-SWNTs with less than 4% iron by mass. Purification was achieved through non-acidic treatment, thus preserving the integrity of the SWNT sidewall. Finally, we also studied the effect of formulation viscosity (% of CMC) on US-tube toxicity.

Twenty-five mice, randomly divided into five groups, received an i.p. injection of a 1 mL bolus of p-SWNTs (500 mg/kg bw), US-tubes (50 mg/kg or 500 mg/kg bw) suspended in 0.1% Tween 60 and 0.9% NaCl aqueous solution, US-tubes (500 mg/kg bw) suspended in the same medium spiked with 2% of CMC, or 1 mL of the vehicle only (0.1% Tween 60, 2% of CMC, and 0.9% NaCl). After abdomen incision at D_7, the organs of all the animals treated with p-SWNTs or the lowest dose of US-tubes remained normal. In the group treated with the highest dose of US-tubes without CMC, only two animals showed signs of inflammation as reflected in the presence of a thin film of cell infiltrate covering the organs. In contrast, for the group treated with the US-tubes suspended with 2% CMC, all the animals showed signs of inflammation with very large deposits of the injected material on the organ surface covered by a thin film of cell infiltrate.

Microscopic examination of the liver and spleen sections of the groups treated with the p-SWNTs or the lowest dose of US-tubes revealed very small granulomas, and, except in one case for each group, they were exclusively located on the surface of the organs. For the group treated with the highest dose of US-tubes without CMC, the granulomas were also very small, and except in two cases, they were located on the

surface of the organs. In contrast, for the group treated with the US-tubes suspended with CMC, all the animals exhibited large multifocal granulomas both inside and on the surface of the organs. While the ALT activities of the latter group increased significantly, those of all the animals treated without CMC were not significantly different from the control group, thus confirming the absence of liver injury (Figure 31B).

In a second part of Experiment III, two groups of six mice each were administered with a 1 mL single bolus (250 mg/kg bw) of US-tubes suspended in 0.9% NaCl with or without 0.1% Tween 60. Three animals of each group were sacrificed at D_1 or at D_2. After microscopic examination, some very small granulomas were observed inside the organs both at D_1 and D_2 for the group treated with the tubes suspended with Tween 60. The granulomatous reaction inside the organs was detected only at D_2 for the second group, thus confirming the lack of diffusion of US-tubes when they are not well-dispersed. This was done to confirm the results of Experiment I.

Elimination Through Urine and Feces. After observing that well-absorbed CNTs did not accumulate in the organs for Experiment III, we proceeded to systematically investigate the presence of the CNTs in the excreted urine and feces. HRTEM analysis of urine and feces samples indicated the abundant presence of both p-SWNTs and US-tubes (Figure 34). The presence of the CNTs in the urine samples was confirmed by HRTEM (Figure 34D, 34E, and 34F). The elimination of US-tubes via the urine was only observed for the first 3 days post-injection, and was qualitatively less in quantity that the p-SWNTs. In contrast, p-SWNT elimination through the entire observation period (14 days). The US-

Figure 34: TEM and HRTEM micrographs of urine and feces extracts. (A) Urine extract from mice (n = 6) treated with a single dose (500 mg/kg bw) of r-SWNTs at D_4 after administration. (B) Urine and (C) feces extracts from mice (n = 6) treated with a single dose (1 g/kg bw) of US-tubes at D_1 after administration. HRTEM micrographs of urine extracts from (D and E) US-tube-treated mice at D_1 and (F) of r-SWNT- treated mice at D_4.

tubes eliminated in the urine were well-dispersed and likely corresponded to the fraction of well-dispersed CNTs present in the administered suspensions. In feces, both well-dispersed and compact bundles of US-tubes were observed.

Conclusion

Considered together with the animal behavior, the biological effects produced by the highest doses of US-tubes agree with the toxic effects and inflammation phenomenon reported previously after intratracheal instillation for non-US-tube CNT materials.[123,132] In contrast, the results obtained in this study using r-SWNTs agree with some reports that observed that SWNTs have relatively low toxicity.[123,124] Although considerably longer than US-tubes, full-length SWNTs were absorbed more efficiently after administration.

Furthermore, the US-tube aggregates were less efficiently dispersed inside the body, while adhering more strongly to the organs than the r-SWNTs. The difference in aggregation behavior between the US-tubes and the SWNT materials investigated in this study is likely due to the differences in their surface structure and chemistry. While the r-SWNT suspensions used in this study were mainly composed of flexible bundles of full-length SWNTs (Figure 35A and 35B), the US-tube suspensions prepared under the same conditions were mainly composed of short, compact bundles of US-tubes (Figure 35C). The cell infiltration phenomenon obviously results in the deposition of large US-tube agglomerates on and inside the organs. The stronger aggregation of the US-tubes, as well as their increased interactions with organ surfaces (possibly strengthened by hydrogen bonding and/or ionic effects), may explain the lack of diffusion of this material. This interpretation may also explain why toxicological studies performed previously with CNTs, purified by a strong acidic treatment, showed harmful effects[124,132,135,136] since it is well-known that strong acidic treatment of r-SWNTs results in surface modification.[137]

Figure 35: TEM micrographs of the injected suspensions. (A) r-SWNTs; (B) p-SWNTs; (C) US-tubes. All scale bars are 500 nm.

The results of Experiment II seem to confirm a hypothesis which links toxicity and the lack of diffusion/absorption of CNTs to their surface structure/chemistry, as well as to their state of aggregation. Dispersing and suspending US-tubes in Tween 60 and CMC in Experiment I did not enhance their absorption; however, they significantly attenuated the cell infiltration when compared to the effects observed in Experiment II. In particular, the dispersion agent, Tween 60, should cover the surface defects and any functionalities on the US-tubes, thus effectively attenuating their interactions with the cell membranes. However, use of the suspension agent, CMC, to increase the stability of the suspension (by increasing the viscosity of the medium) led to the immobilization of the CNT aggregates inside the abdomen and increased toxicity.

Experiment III demonstrated that covering the US-tubes with Tween 60 and lowering the viscosity of the formulation by eliminating CMC can enhance their absorption and attenuate their ability to induce large granulomas and cell infiltration, thus further confirming the dependence of these effects on the degree of agglomeration and CNT surface chemistry. Furthermore, removing the metal catalyst of the r-SWNT samples by means of a non-acidic treatment also resulted in the attenuation of liver injury (Figure 33B).

For all of the Experiments (I, II, III), the architectures of the organs remained normal without any sign of necrosis or fibrosis. Inside the organs, even for the highest doses of US-tubes, the granulomas were well circumscribed without any sign of fibrosis (Figure 31). Microscopic examinations also demonstrated that when the CNTs were well absorbed, most notably p-SWNTs, they do not accumulate inside the organs. Our results show for the first time that both underivatized SWNTs and US-tubes are cleared after

administration through the kidneys and probably bile ducts, as intact CNTs. However, this result must be confirmed by isolating the CNTs in pure bile because of the possible contamination of the feces by the urine during collection.

The results of the present study address the differences in toxicological assessments and the conclusions of previous studies on pulmonary[138] and subcutaneous toxicity of CNTs.[124] Since the US-tube aggregates are far more toxic than the r-SWNT and p-SWNT aggregates, the differences in toxicological assessments observed previously are probably due to the differences in the surface structure/chemistry and the degree of aggregation of the materials. Our results also confirm that the intrinsic toxicity of CNTs is mainly characterized by a granulomatous response. However, this response is only induced upon the deposition and the adsorption of large CNT aggregates. It is important to remember that the goal of this study was to investigate the toxicity of maximum doses. It is difficult to imagine a medical procedure that would require doses anywhere near the maximum doses used in this study (1 g/kg). When CNTs are well-dispersed, most notably for p-SWNTs, signs of necrosis, fibrosis, or liver degeneration are absent, suggesting that the inflammatory effect is mainly due to the degree of aggregation. The presence of CNTs in the excreted urine and feces shows that when CNTs are individualized, and probably also when the aggregates are very small, they can be eliminated without any sign of toxicity. This furthermore confirms the belief that in order for CNT materials to realize their biomedical potential they should be engineered into discrete, individual species.

Finally, as the toxicity can clearly be attenuated through dose formulation, further work needs to investigate the pharmacokinetics of derivatized nanotubes. *in vivo*

imaging suggests there is differential distribution and elimination compared to Magnevist. These properties might be exploited for new imaging agents. Further work exploring organ uptake and chronic exposure is needed. The role of surface coverings and its control over nanotube uptake, distribution, and elimination will be a significant field of study in the coming years.

THE FUTRE DIRECTION OF THE US-TUBE PLATFORM IN MEDICINE

Clearly, nanoscale materials have much to offer the field of medicine by providing new or improved opportunities for imaging and therapy. Hybrid combinations of such materials are already beginning to be explored, and undoubtedly, many new materials will be forthcoming in the future. As these agents continue to evolve, more emphasis will be placed on engineering single agents that are both therapeutic and diagnostic, or "theranostic" by design. These theranostic drugs will feature guided cancer therapy, allowing the oncologist to track the distribution and targeted accumulation of the agent within the patient before the therapy is triggered externally by NIR, magnetic fields, or radiofrequency signaling, or perhaps combinations thereof.

Carbon nanotubes have the potential to play a significant role in the development of new nanoplatforms. In only a few short years, these materials have been shown to dramatically outperform current clinical MRI CAs both *in vitro* and *in vivo* and have been derivatized for biocompatibility and cell targeting. With their ultra-sensitive relaxivity response to pH, they have the potential to revolutionize the field of medical MR imaging, possibly functioning as a non-targeted, cancer-specific MRI CA. They could compliment (or even replace) current MRI contrast agents because of their superior relaxivities or they may encourage the development of entirely new technologies, such as micro-tesla imaging.

The US-tube platform is not limited to only imaging since the US-tubes also have been loaded with an α-radionuclide, At-211. As the loading of ions inside the interior of the US-tube appears to be indiscriminate, different species could be loaded inside the tube for multi-functionality. For instance, the US-tube could be loaded with At-211 and

Gd^{3+} for a magnetically-guided radiotherapeutic, or with Gd^{3+} and $^{124}I^-$ for a multi-modal MRI/PET imaging agent. The US-tubes can easily be functionalized with peptides for targeting, and current work is underway to develop nanotube-antibody conjugates.

APPENDIX I: ABBREVIATIONS AND SYMBOLS

α	alpha particle ($^4He^{2+}$)
AFM	atomic force microscope
ALT	alanine aminotransferase
Arg	arginine
Arc	arc-ablation-produced SWNTs
β^-	beta particle (an electron)
BSA	bovine serum albumin (suspended gadonanotubes)
bw	body weight
c	concentration
°C	degrees Celsius
CA(s)	contrast agent(s)
ChT	chloramine-T
cm	centimeter
CMC	carboxymethylcellulose
CNTs	carbon nanotubes (may be single-walled, multi-walled, etc.)
conc.	concentrated
D_n	the n^{th} day of the toxicity study
DI	deionized
DLS	dynamic light scattering
DMF	dimethylformamide
DTPA	diethylene triamine pentaacetic acid

EC	electron capture
EDC	1-ethyl-3-[3-dimethylaminopropyl]carbodiimide hydrochloride
Et	ethyl
eV	electron volt
FDA	[United States)]Food and Drug Administration
Ful	$Gd@C_{60}(OH)_x$
g	gram
g	G-force acceleration
GadoPegEgg	gadonanotube inside a PEG-egg
HiPco	high pressure carbon monoxide produced-SWNTs
HPLC	high-performance liquid chromatography
HRTEM	high-resolution transmission electron microscopy
keV	kilo electron volt
ICP-OES	inductively coupled plasma-optical emission spectroscopy
i.p.	intraperitoneal
i.v.	intravenous
kg	kilogram
LET	linear energy transfer
M	molar (moles per liter)
Mag	Magnevist
mCi	milliCurie
Me	methyl
Met	methionine

MeV	mega electron volt
mg	milligram
MHz	megahertz
mL	milliliter
mm	millimeter
mM	millimolar
MRI	magnetic resonance imaging
ms	millisecond
N	normal solution
Na^0	sodium metal
NaH	sodium hydride
NCS	N-chlorosuccinimide
NIR	near infrared
nm	nanometer
NMR	nuclear magnetic resonance
NMRD	nuclear magnetic resonance dispersion (relaxivity vs. magnetic field)
ns	nanosecond
PAA	polyacrylic acid
PAMAM	poly(amidoamine) dendrimer
PBS	phosphate buffer saline solution
PEEK	polyetheretherketone
PEG	polyethylene glycol
PEG-egg	cross-linked polyethylene glycol micelle

PFP	pentafluorophenyl
ppb	parts per billion (microgram per liter)
ppm	parts per million (milligram per liter)
ppt	parts per thousand (gram per liter)
PS	polystyrene
p-SWNTs	purified SWNTs
PTFE	polytetrafluoroethylene
r_1	T_1-weighted relaxivity
r_2	T_2-weighted relaxivity
RF	radiofrequency
RGD	arginine-glycine-aspartic acid
ROI	region of interest
r-SWNTs	raw SWNTs
s	seconds
SBM	Solomon-Bloembergen-Morgan (theory of paramagnetic relaxation)
SDBS	sodium dodecyl benzene sulfonate
Ser	serine (derivatized gadonanotubes)
SPECT	single photon emission computed tomography
SPIO	superparamagnetic iron oxide
SQUID	superconducting quantum interference device
SWNT	single-walled carbon nanotube(s)
T	Tesla
$t_{½}$	half-life (decay rate)

T_1	T_1-weighted relaxation time
T_2	T_2-weighted relaxation time
TEM	transmission electron microscopy
TGA	thermogravimmetric analysis
THF	tetrahydrofuran
Thr	threonine
TRT	targeted radiotherapy
μCi	microCurie
μg	microgram
μm	micrometer
US-tubes	ultra-short, single-walled carbon nanotubes
VCAM	vascular cell adhesion molecule
W	Watt
XAES	X-ray-induced Auger electron spectroscopy
XPS	X-ray photoelectron spectroscopy

Appendix II: GadoPegEgg Relaxivity Studies

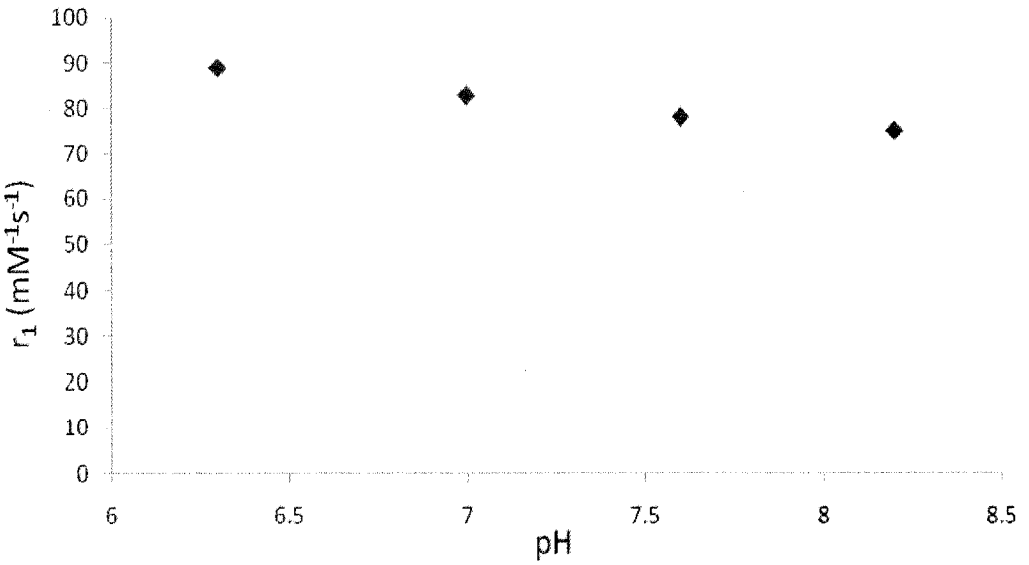

Figure A1: Relaxivity as a function of pH for the GadoPegEgg at 60MHz and 37 °C.

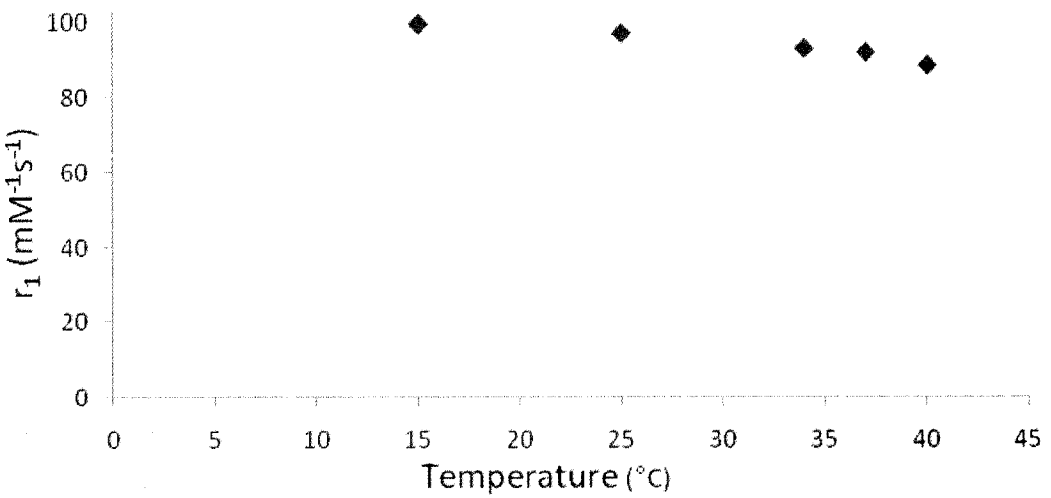

Figure A2: Relaxivity as a function of temperature for the GadoPegEgg at 60 MHz and pH = 6.3.

APPENDIX III: TGA, RAMAN, AND XPS DATA

All Raman spectra collected using a Renishaw Raman microscope, using a 633 nm laser. TGA data was acquired on a TA Instruments SDT 2960 DSC-TGA instrument. The temperature was ramped at 6 °C per minute, under flowing argon gas. For XPS analysis, samples were pressed into indium foil and data collected on a Phi Quantera XPS spectrometer.

II Gadonanotube-Ethyl ester

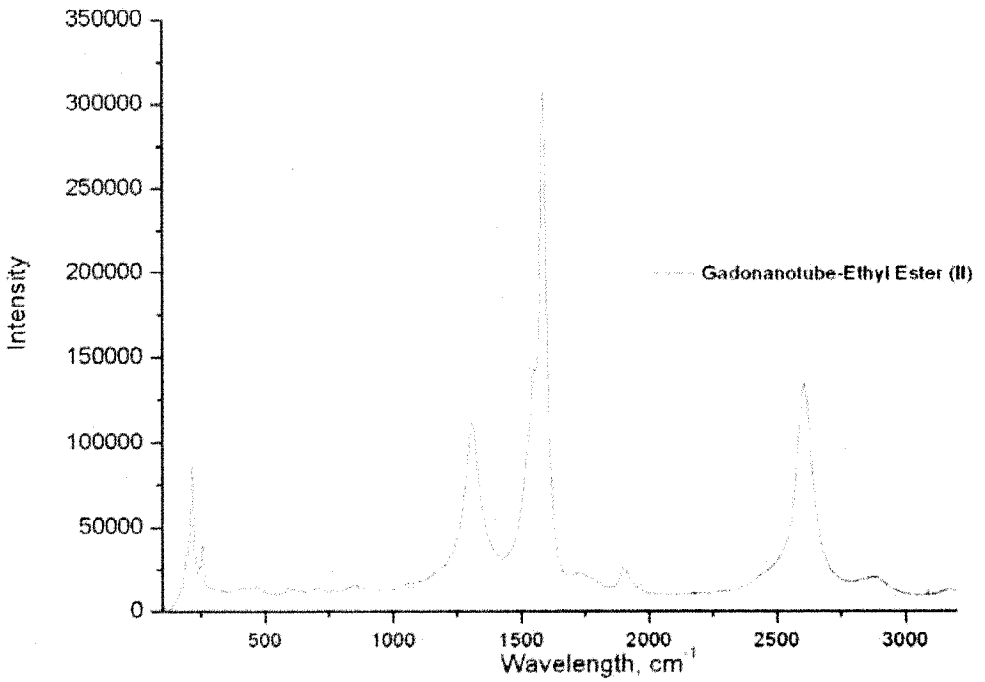

Figure A3: Raman spectrum of compound **II**.

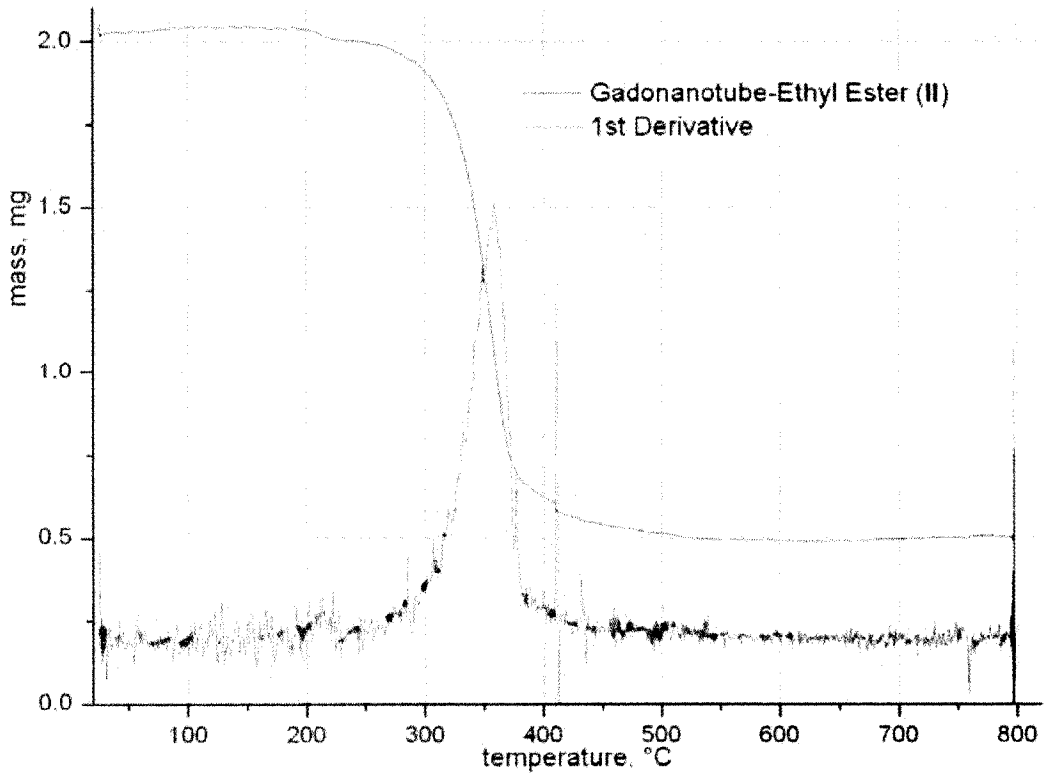

Figure A4: TGA spectrum of compound **II**.

IVa Gadonanotube-Methyl Amide

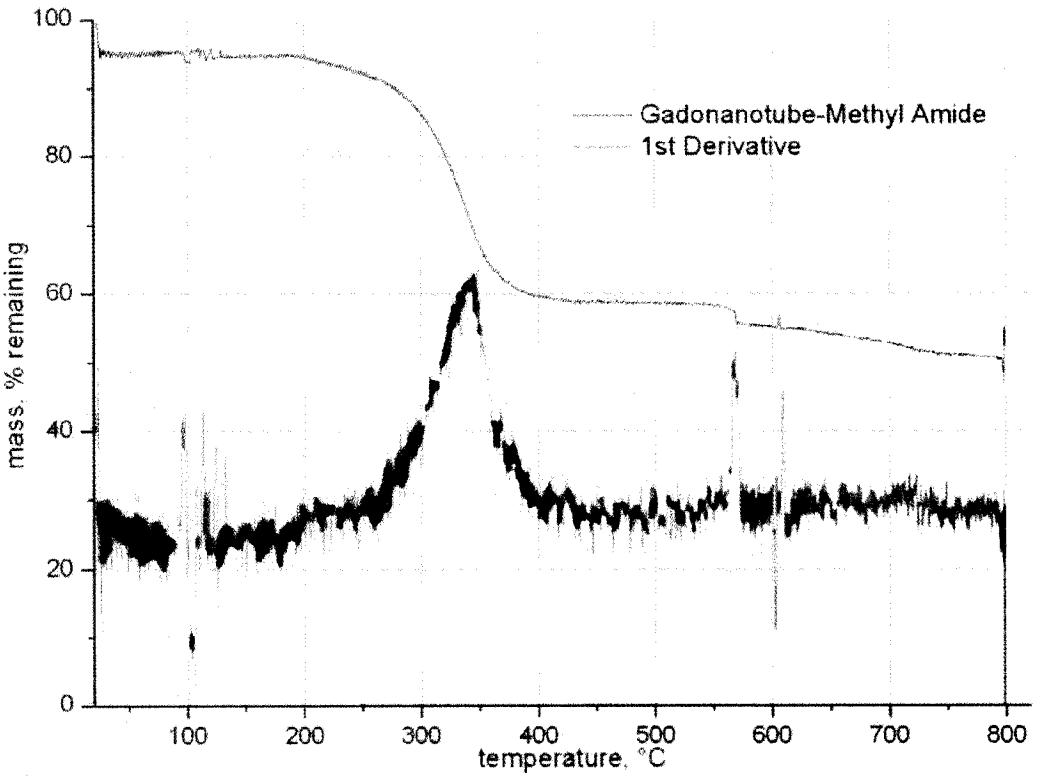

Figure A5: TGA spectrum of compound **IVa**.

IVb Gadonanotube-Serinol

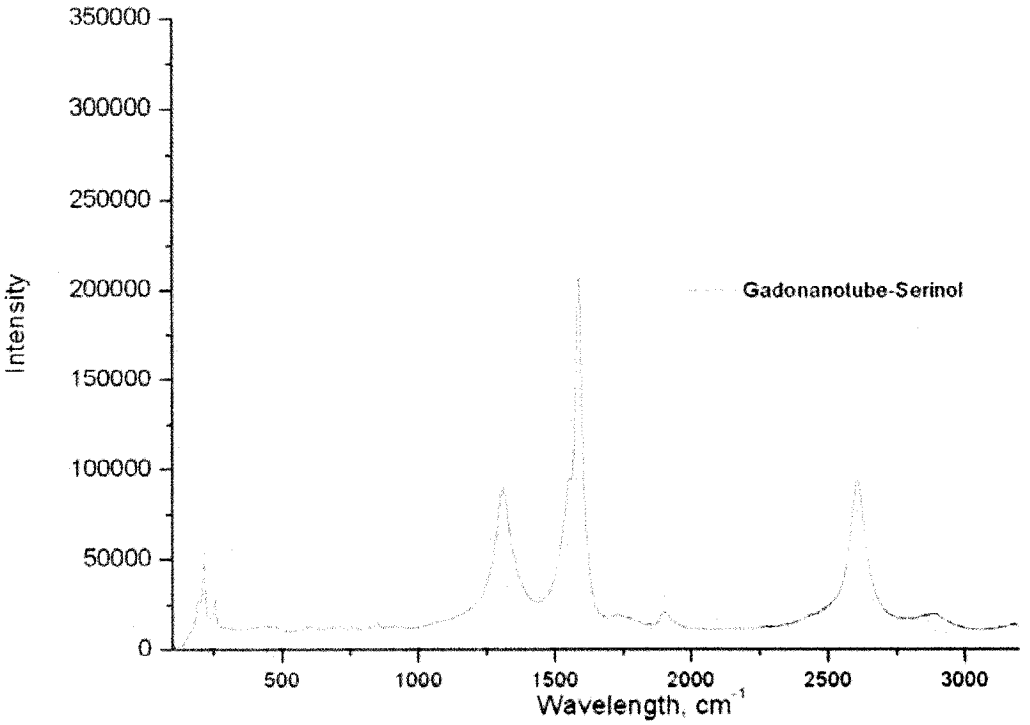

Figure A6: TGA spectrum of compound **IVb**.

Table AI: XPS data from the Gadonanotube-Serinol (**IVb**) sample; values are an average of 3 measurements.

	C	O	N
Atomic %	71.3	23.8	4.9

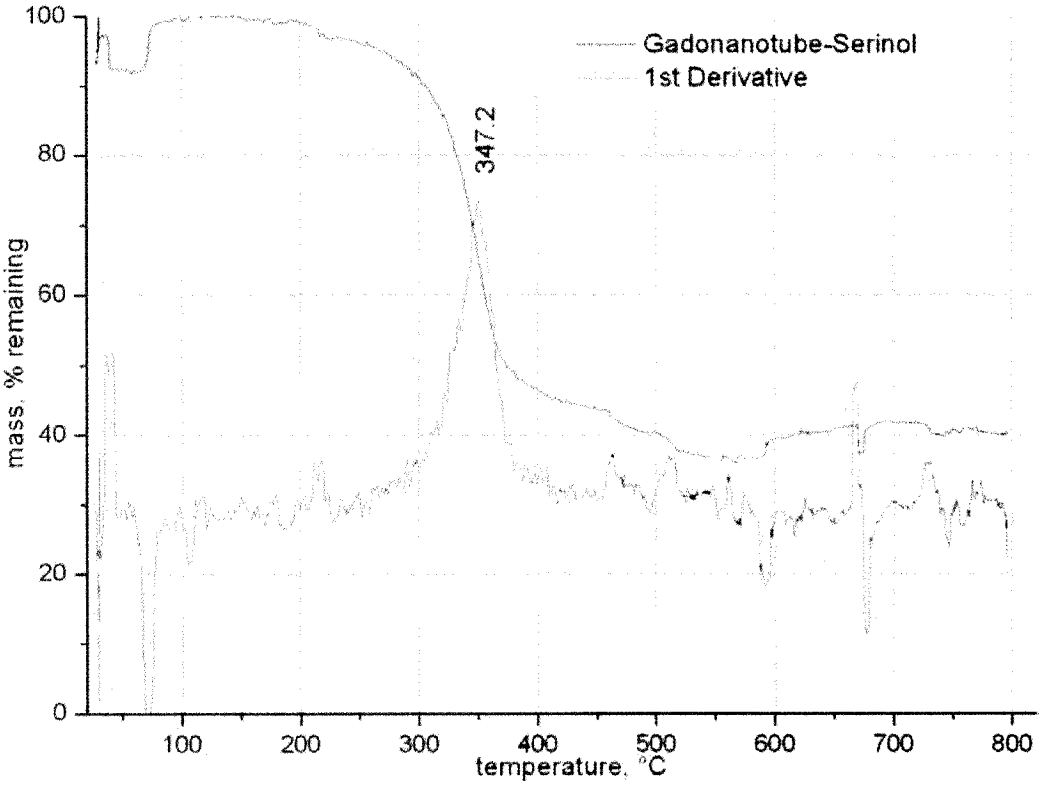

Figure A7: TGA spectrum of compound **IVb**.

IVc Gadonanotube-Met

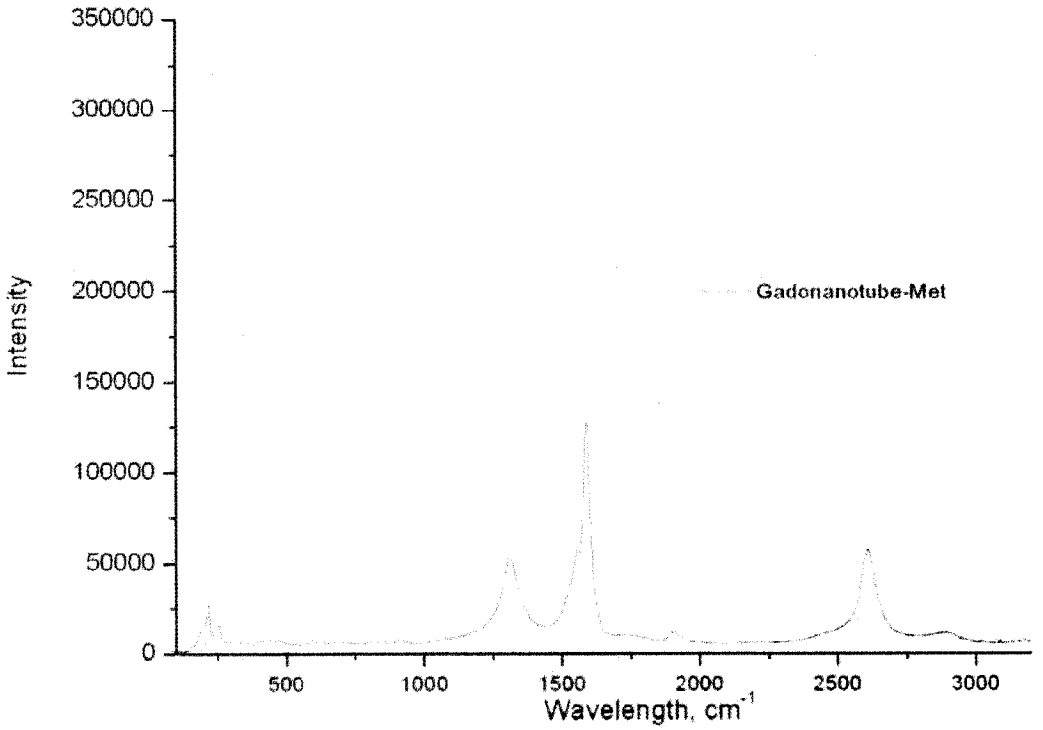

Figure A8: Raman spectrum of compound **IVc**.

Table AII: XPS data from the Gadonanotube-Met (**IVc**) sample; values are an average of 3 measurements.

	C	O	S	N	F
Atomic %	56.1	28.6	8.1	7.1	0.2

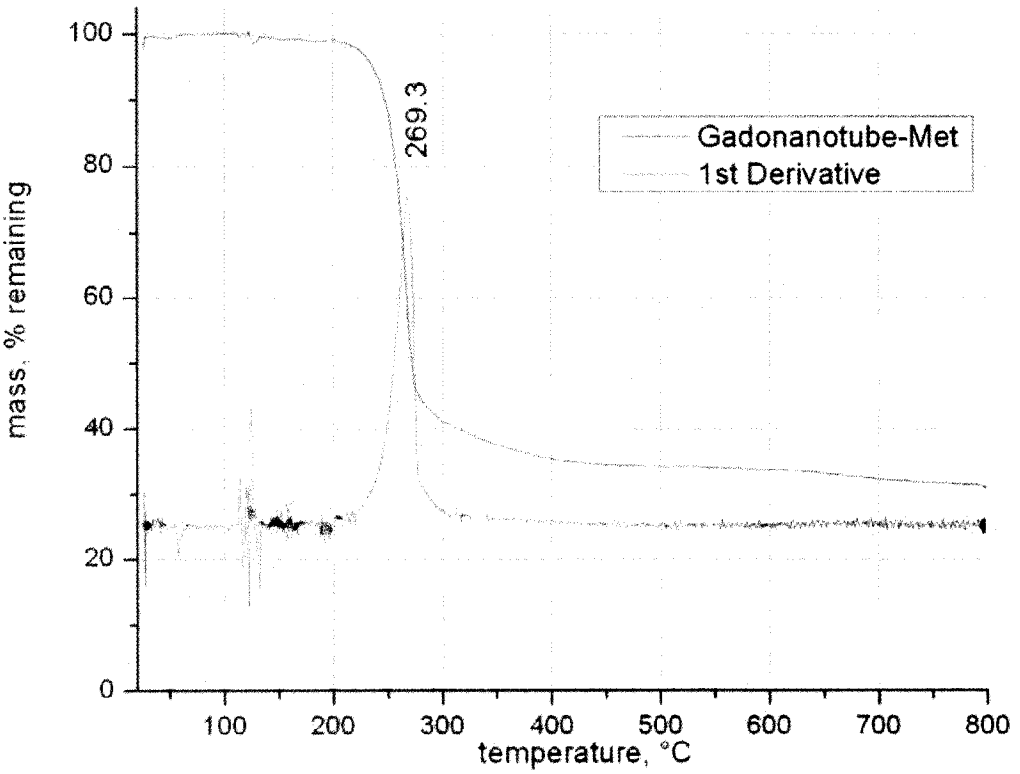

Figure A9: TGA spectrum of compound **IVc**.

IVd Gadonanotube-Ser

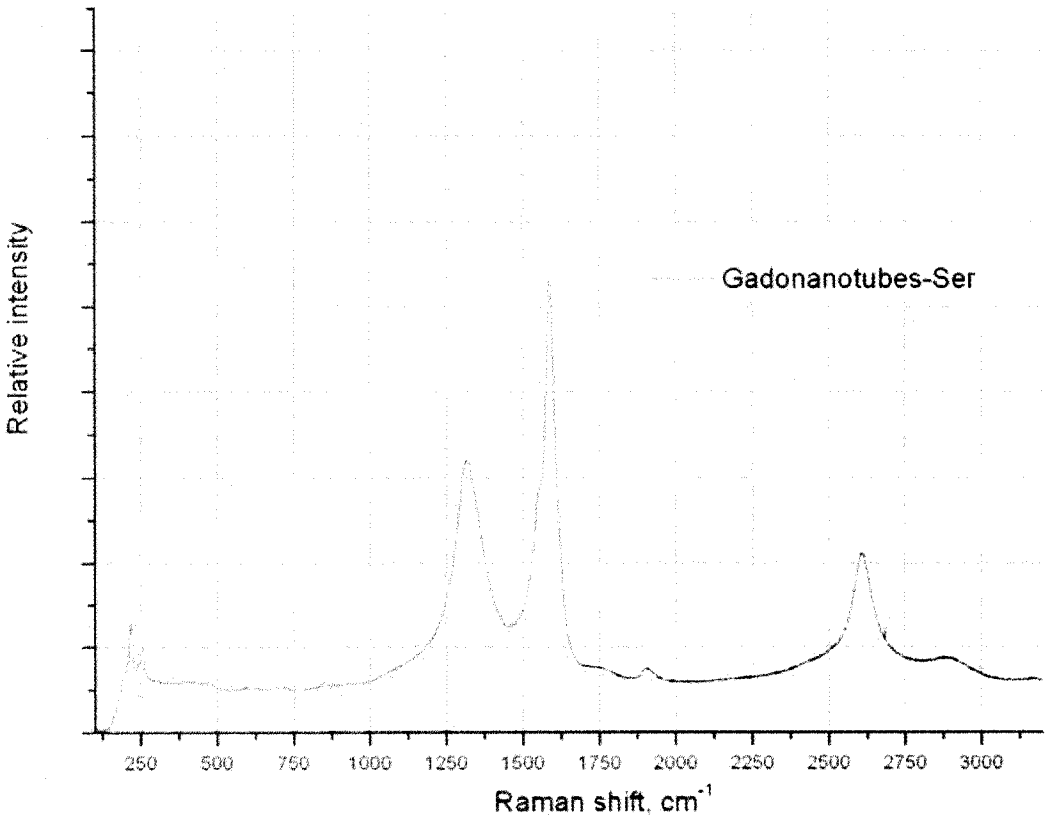

Figure A10: Raman spectrum of compound **IVd**.

Table AIII: XPS data from the Gadonanotube-Ser (**IVd**) sample; values are an average of 3 measurements.

	C	O	N	Gd
Atomic %	77.7	21.5	0.5	0.3

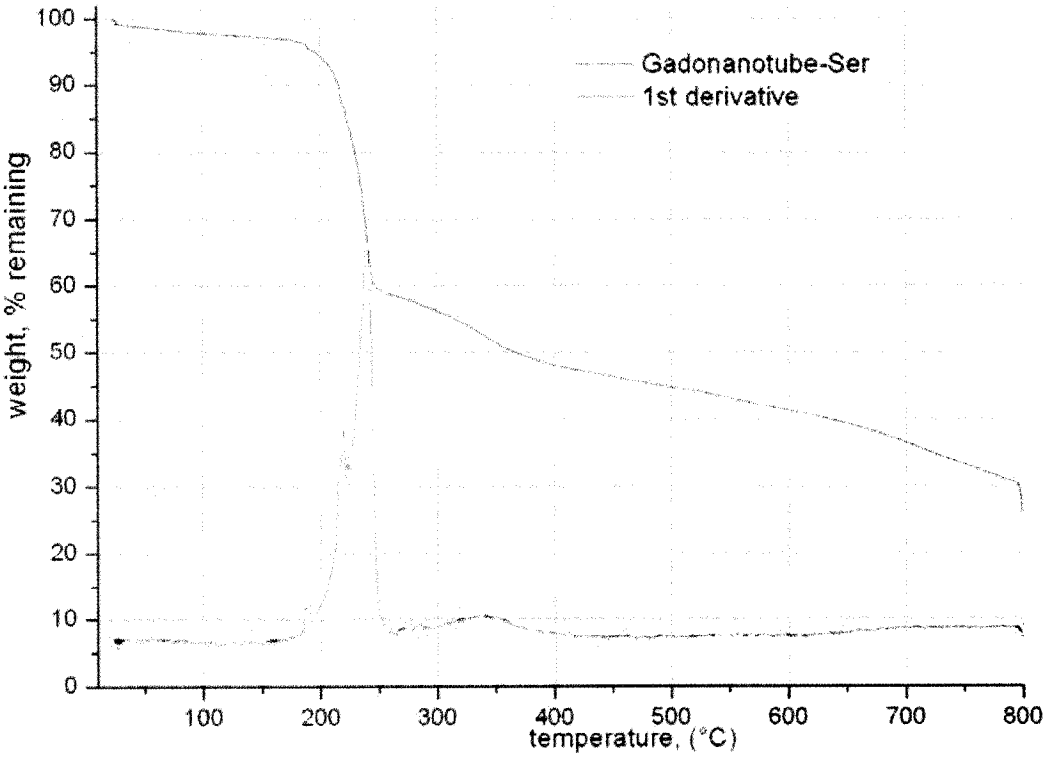

Figure A11: TGA spectrum of compound **IVd**.

IVe Gadonanotube-Thr

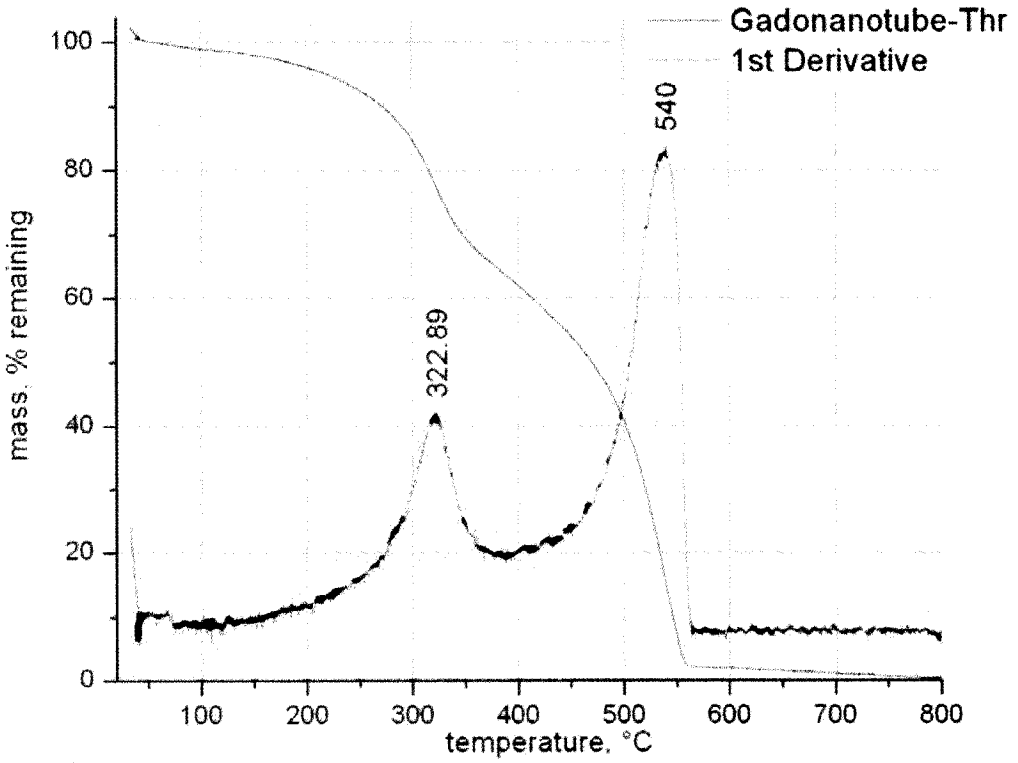

Figure A12: TGA spectrum of compound **IVe**.

IVf Gadonanotube-Arg

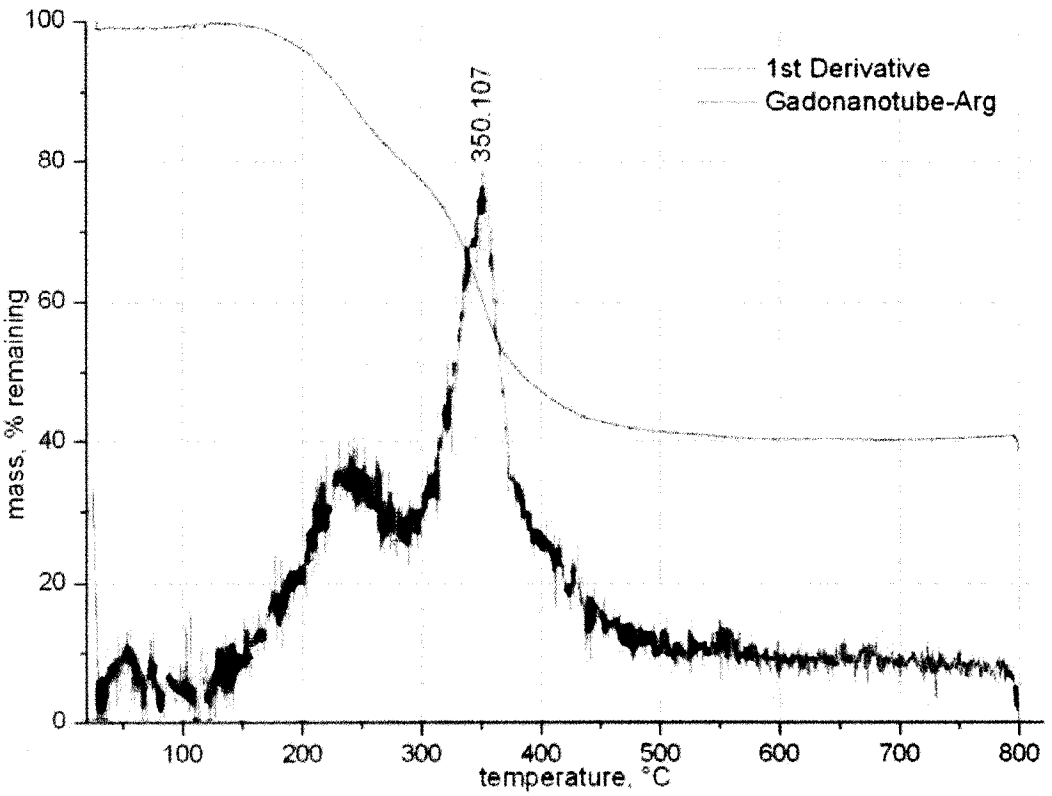

Figure A13: TGA spectrum of compound **IVf**.

V Gadonanotube-RGD-Ser

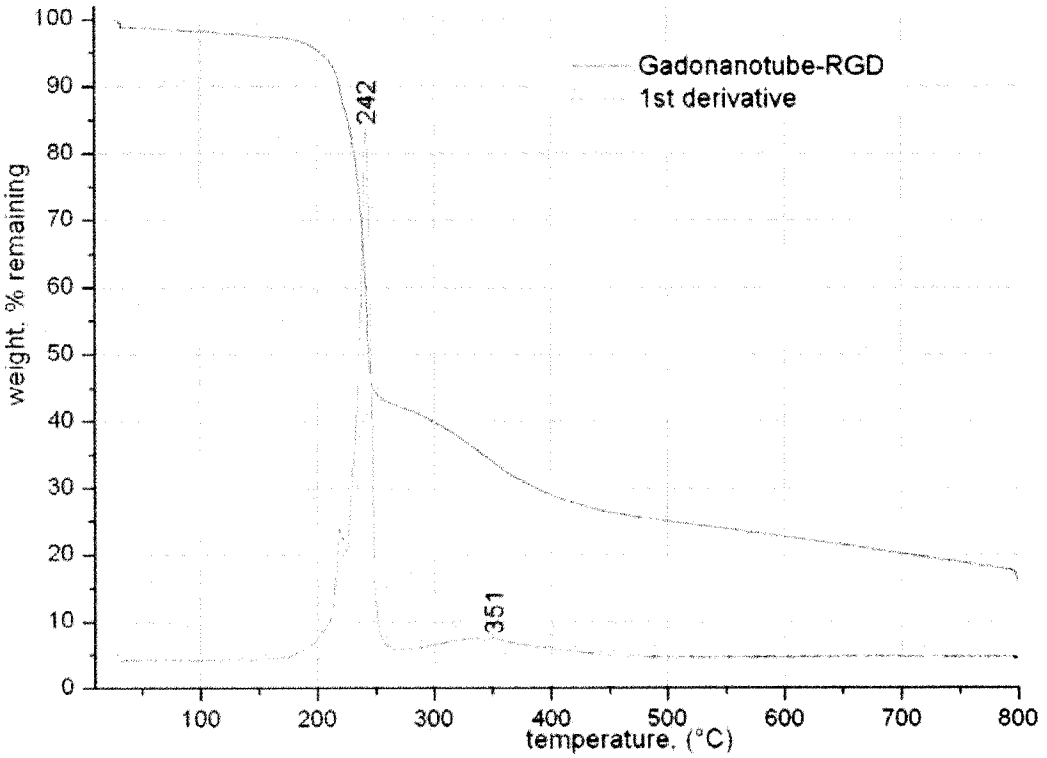

Figure A14: TGA spectrum of compound **V**.

Table AIV: XPS data from the Gadonanotube-RGD-Ser (**V**) sample; values are an average of 7 measurements.

	C	O	N	Gd
Atomic %	76.2	22.2	1.4	.2

APPENDIX IV: ANIMAL IMAGING AND INTENSITY AS A FUNCTION OF TIME

BSA-suspended gadonanotubes were injected into mice as described in Chapter III. The below images and intensities are displayed for the liver and kidney. The intensities have not been standardized.

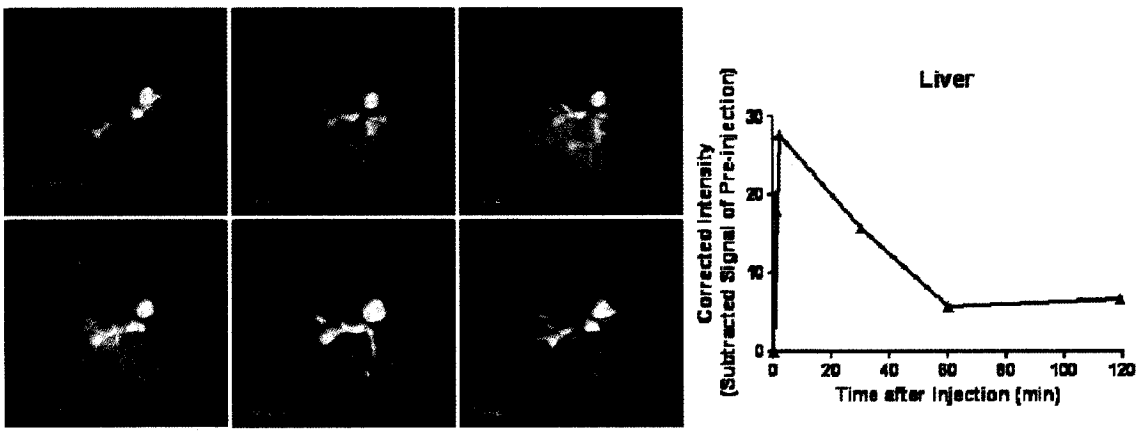

Figure A15: Image and intensity of the liver at t = 0, 1, 2, 30, 60, and 119 minutes post-injection of BSA-suspended gadonanotubes.

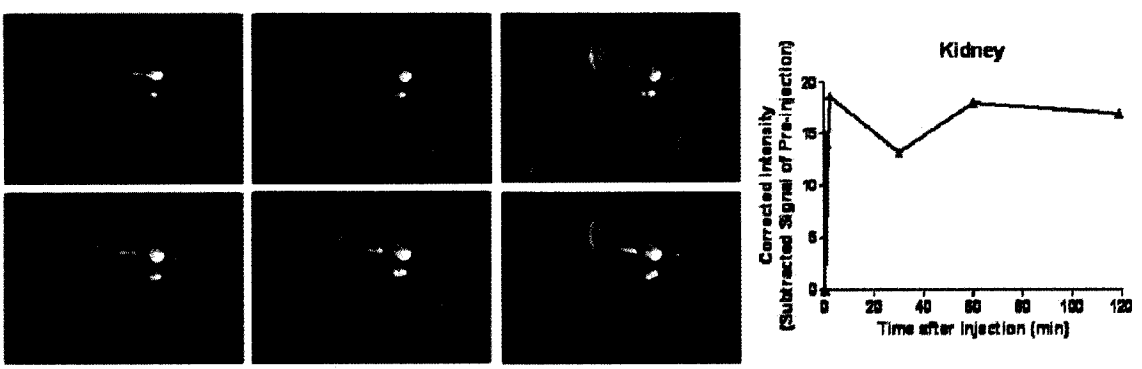

Figure A16: Image and intensity of the kidney at t = 0, 1, 2, 30, 60, and 119 minutes post-injection of BSA-suspended gadonanotubes.

REFERENCES

1. A. E. Merbach, E. Toth, Editors, *The Chemistry of Contrast Agents in Medical Magnetic Resonance Imaging*. John Wiley & Sons, Ltd.: London, 2001.

2. R. B. Lauffer, *Chem. Rev.* **1987,** *87*, 901-927.

3. R. N. Muller, L. Vander Elst, P. A. Rinck, P. Vallet, F. Maton, H. Fischer, A. Roch, Y. Van Haverbeke, *Invest. Radiol.* **1988,** *23 Suppl 1*, S229-31.

4. N. R. Jagannathan, *Curr. Sci.* **2007,** *92(8)*, 1061-1070.

5. W. Cai, J. Rao, S. S. Gambhir, X. Chen, *Molec. Canc. Therap.* **2006,** *5(11)*, 2624-2633.

6. S. Gross, D. Piwnica-Worms, *Curr. Op. Chem. Biol.* **2006,** *10(4)*, 334-342.

7. R. Weissleder, *Science* **2006,** *312(5777)*, 1168-1171.

8. A. Agrawal, Y. Xing, X. Gao, S. Nie, *Nanotechnol. Biol. Med.* **2007**, 10/1-10/15, 2 plates.

9. J. M. Klostranec, W. C. W. Chan, *Adv. Mater.* **2006,** *18(15)*, 1953-1964.

10. L. R. Hirsch, A. M. Gobin, A. R. Lowery, F. Tam, R. A. Drezek, N. J. Halas, J. L. West, *Ann. Biomed. Eng.* **2006,** *34(1)*, 15-22.

11. M. Bruchez, Jr., M. Moronne, P. Gin, S. Weiss, A. P. Alivisatos, *Science* **1998,** *281(5385)*, 2013-2016.

12. J. K. Jaiswal, H. Mattoussi, J. M. Mauro, S. M. Simon, *Nat. Biotechnol.* **2003,** *21(1)*, 47-51.

13. H. Kobayashi, Y. Hama, Y. Koyama, T. Barrett, C. A. S. Regino, Y. Urano, P. L. Choyke, *Nano Lett.* **2007,** *7(6)*, 1711-1716.

14. M.-K. So, C. Xu, A. M. Loening, S. S. Gambhir, J. Rao, *Nat. Biotechnol.* **2006,** *24(3)*, 339-343.

15. H. Wang, D. W. Brandl, P. Nordlander, N. J. Halas, *Acc. Chem. Res.* **2007,** *40(1)*, 53-62.

16. A. M. Gobin, M. H. Lee, N. J. Halas, W. D. James, R. A. Drezek, J. L. West, *Nano Lett.* **2007,** *7(7)*, 1929-34.

17. L. R. Hirsch, R. J. Stafford, J. A. Bankson, S. R. Sershen, B. Rivera, R. E. Price, J. D. Hazle, N. J. Halas, J. L. West, *PNAS* **2003,** *100(23)*, 13549-13554.

18. C. Corot, P. Robert, J.-M. Idee, M. Port, *Adv. Drug Deliv. Rev.* **2006,** *58(14)*, 1471-1504.

19. E. Duguet, S. Vasseur, S. Mornet, J.-M. Devoisselle, *Nanomed.* **2006,** *1(2)*, 157-168.

20. P. Tartaj, M. d. P. Morales, S. Veintemillas-Verdaguer, T. Gonzalez-Carreno, C. J. Serna, *J. Phys. D Appl. Phys.* **2003,** *36(13)*, R182-R197.

21. A. K. Gupta, M. Gupta, *Biomater.* **2005,** *26(18)*, 3995-4021.

22. S. Mornet, S. Vasseur, F. Grasset, E. Duguet, *J. Mater. Chem.* **2004,** *14(14)*, 2161-2175.

23. O. Clement, N. Siauve, C. A. Cuenod, G. Frija, *Top. Magn. Reson. Imaging* **1998,** *9(3)*, 167-82.

24. W. Li, S. Tutton, T. Vu Anthony, L. Pierchala, S. Y. Li Belinda, M. Lewis Jerome, V. Prasad Pottumarthi, R. Edelman Robert, *J. Magn. Reson. Imaging* **2005,** *21(1)*, 46-52.

25. S. J. McLachlan, M. R. Morris, M. A. Lucas, R. A. Fisco, M. N. Eakins, D. R. Fowler, R. B. Scheetz, A. Y. Olukotun, *J. Magn. Reson. Imaging* **1994,** *4(3)*, 301-7.

26. P. Reimer, C. Marx, E. J. Rummeny, M. Muller, M. Lentschig, T. Balzer, K. H. Dietl, U. Sulkowski, T. Berns, K. Shamsi, P. E. Peters, *J. Magn. Reson. Imaging* **1997,** *7(6)*, 945-9.

27. M. Taupitz, S. Wagner, J. Schnorr, I. Kravec, H. Pilgrimm, H. Bergmann-Fritsch, B. Hamm, *Invest. Radiol.* **2004,** *39(7)*, 394-405.

28. P. Reimer, B. Tombach, *Eur. Radiol.* **1998,** *8(7)*, 1198-204.

29. A. Toma, E. Otsuji, Y. Kuriu, K. Okamoto, D. Ichikawa, A. Hagiwara, H. Ito, T. Nishimura, H. Yamagishi, *Brit. J. Canc.* **2005,** *93(1)*, 131-136.

30. A. Funovics Martin, B. Kapeller, C. Hoeller, S. Su Henry, R. Kunstfeld, S. Puig, K. Macfelda, *Magn. Reson. Imaging* **2004,** *22(6)*, 843-50.

31. A. Tsourkas, V. R. Shinde-Patil, K. A. Kelly, P. Patel, A. Wolley, J. R. Allport, R. Weissleder, *Bioconj. Chem.* **2005,** *16(3)*, 576-581.

32. L. Josephson, C.-H. Tung, A. Moore, R. Weissleder, *Bioconj. Chem.* **1999,** *10(2)*, 186-191.

33. M. Zhao, F. Kircher Moritz, L. Josephson, R. Weissleder, *Bioconj. Chem.* **2002,** *13(4)*, 840-4.

34. C. Leuschner, C. S. Kumar, W. Hansel, W. Soboyejo, J. Zhou, J. Hormes, *Breast Canc. Res. Treat.* **2006,** *99(2)*, 163-76.

35. C. Sun, R. Sze, M. Zhang, *J. Biomed. Mater. Res. A* **2006,** *78(3)*, 550-7.

36. C. Bos, Y. Delmas, A. Desmouliere, A. Solanilla, O. Hauger, C. Grosset, I. Dubus, Z. Ivanovic, J. Rosenbaum, P. Charbord, C. Combe, W. M. Bulte Jeff, T. W. Moonen Chrit, J. Ripoche, N. Grenier, *Radiol.* **2004,** *233(3)*, 781-9.

37. A. Frank Joseph, R. Miller Brad, S. Arbab Ali, A. Zywicke Holly, E. K. Jordan, K. Lewis Bobbi, L. H. Bryant, Jr., W. M. Bulte Jeff, *Radiol.* **2003,** *228(2)*, 480-7.

38. C.-J. Chen, S. Hayek, V. Mohite, H. Yuan, J. Chatterjee, Y. Haik, *Canc. Nanotech.* **2007**, 159-195.

39. S. B. Field, N. M. Bleehen, *Cancer Treat. Rev.* **1979,** *6(2)*, 63-94.

40. C. D. Kowal, J. R. Bertino, *Cancer Res.* **1979,** *39(6 Pt 2)*, 2285-9.

41. R. E. Rosensweig, *J. Magn. Magn. Mater.* **2002,** *252(1-3)*, 370-374.

42. A. Jordan, T. Rheinlaender, N. Waldoefner, R. Scholz, *J. Nanopart. Res.* **2003,** *5(5-6)*, 597-600.

43. Q. A. Pankhurst, J. Connolly, S. K. Jones, J. Dobson, *J. Phys. D Appl. Phys.* **2003,** *36(13)*, R167-R181.

44. M. Johannsen, U. Gneveckow, K. Taymoorian, B. Thiesen, N. Waldofner, R. Scholz, K. Jung, A. Jordan, P. Wust, S. A. Loening, *Int. J. Hyperthermia* **2007,** *23(3)*, 315-23.

45. H. W. Kroto, J. R. Heath, S. C. O'Brien, R. F. Curl, R. E. Smalley, *Nature* **1985,** *318(6042)*, 162-3.

46. D. M. Guldi, G. M. A. Rahman, V. Sgobba, C. Ehli, *Chem. Soc. Rev.* **2006,** *35(5)*, 471-487.

47. D. Tasis, N. Tagmatarchis, A. Bianco, M. Prato, *Chem. Rev.* **2006,** *106(3)*, 1105-1136.

48. H. Dai, *Acc. Chem. Res.* **2002,** *35(12)*, 1035-1044.

49. R. C. Haddon, *Acc. Chem. Res.* **2002,** *35(12)*, 997.

50. A. Hartschuh, H. N. Pedrosa, J. Peterson, L. Huang, P. Anger, H. Qian, A. J. Meixner, M. Steiner, L. Novotny, T. D. Krauss, *Chem. Phys. Chem.* **2005,** *6(4)*, 577-582.

51. L. Cognet, D. A. Tsyboulski, J.-D. R. Rocha, C. D. Doyle, J. M. Tour, R. B. Weisman, *Science* **2007,** *316(5830)*, 1465-1468.

52. P. Cherukuri, S. M. Bachilo, S. H. Litovsky, R. B. Weisman, *J. Am. Chem. Soc.* **2004,** *126(48)*, 15638-15639.

53. P. Cherukuri, C. J. Gannon, T. K. Leeuw, H. K. Schmidt, R. E. Smalley, S. A. Curley, R. B. Weisman, *PNAS* **2006,** *103(50)*, 18882-18886.

54. T. K. Leeuw, R. M. Reith, R. A. Simonette, M. E. Harden, P. Cherukuri, D. A. Tsyboulski, K. M. Beckingham, R. B. Weisman, *Nano Lett.* **2007,** *7(9)*, 2650-2654.

55. N. W. S. Kam, M. O'Connell, J. A. Wisdom, H. Dai, *PNAS* **2005,** *102(33)*, 11600-11605.

56. C. J. Gannon, P. Cherukuri, B. I. Yakobson, L. Cognet, J. S. Kanzius, C. Kittrell, R. B. Weisman, M. Pasquali, H. K. Schmidt, R. E. Smalley, S. A. Curley, *Canc.* **2007**.

57. R. D. Bolskar, A. F. Benedetto, L. O. Husebo, R. E. Price, E. F. Jackson, S. Wallace, L. J. Wilson, J. M. Alford, *J. Am. Chem. Soc.* **2003,** *125(18)*, 5471-5478.

58. P. Fatouros Panos, D. Corwin Frank, Z.-J. Chen, C. Broaddus William, L. Tatum James, B. Kettenmann, Z. Ge, W. Gibson Harry, L. Russ Jennifer, P. Leonard Anthony, C. Duchamp James, C. Dorn Harry, *Radiol.* **2006,** *240(3)*, 756-64.

59. S. Laus, B. Sitharaman, E. Toth, R. D. Bolskar, L. Helm, S. Asokan, M. S. Wong, L. J. Wilson, A. E. Merbach, *J. Am. Chem. Soc.* **2005,** *127(26)*, 9368-9369.

60. S. Laus, B. Sitharaman, E. Toth, R. D. Bolskar, L. Helm, L. J. Wilson, A. E. Merbach, *J. Phys. Chem. C* **2007,** *111(15)*, 5633-5639.

61. B. Sitharaman, R. D. Bolskar, I. Rusakova, L. J. Wilson, *Nano Lett.* **2004,** *4(12)*, 2373-2378.

62. B. Sitharaman, L. A. Tran, Q. P. Pham, R. D. Bolskar, R. Muthupillai, S. D. Flamm, A. G. Mikos, L. J. Wilson, *Contrast Media Molec. Imag.* **2007,** *2(3)*, 139-146.

63. E. Toth, R. D. Bolskar, A. Borel, G. Gonzalez, L. Helm, A. E. Merbach, B. Sitharaman, L. J. Wilson, *J. Am. Chem. Soc.* **2005,** *127(2)*, 799-805.

64. N. Bloembergen, *J. Chem. Phys.* **1957,** *27*, 572.

65. N. Bloembergen, L. O. Morgan, *J. Chem. Phys.* **1961,** *34*, 842.

66. N. Bloembergen, E. M. Purcell, R. V. Pound, *Phys. Rev.* **1948,** *73*, 678.

67. I. Solomon, *Phys. Rev.* **1955,** *99*, 559.

68. I. Solomon, N. Bloembergen, *J. Chem. Phys.* **1956,** *25*, 261.

69. I. Bertini, O. Galas, C. Luchinat, G. Parigi, *J. Magn. Reson. A* **1995,** *113(2)*, 151-8.

70. J. M. Ashcroft, D. A. Tsyboulski, K. B. Hartman, T. Y. Zakharian, J. W. Marks, R. B. Weisman, M. G. Rosenblum, L. J. Wilson, *Chem. Commun.* **2006,** *(28)*, 3004-3006.

71. F. Rancan, M. Helmreich, A. Moelich, E. A. Ermilov, N. Jux, B. Roeder, A. Hirsch, F. Boehm, *Bioconj. Chem.* **2007,** *18(4)*, 1078-1086.

72. B. Sitharaman, K. R. Kissell, K. B. Hartman, L. A. Tran, A. Baikalov, I. Rusakova, Y. Sun, H. A. Khant, S. J. Ludtke, W. Chiu, S. Laus, E. Toth, L. Helm, A. E. Merbach, L. J. Wilson, *Chem. Commun.* **2005,** *(31)*, 3915-3917.

73. Z. Gu, H. Peng, R. H. Hauge, R. E. Smalley, J. L. Margrave, *Nano Lett.* **2002,** *2(9)*, 1009-1013.

74. L. A. Girifalco, M. Hodak, R. S. Lee, *Phys. Rev. B* **2000,** *62(19)*, 13104-13110.

75. J. M. Ashcroft, K. B. Hartman, Y. Mackeyev, C. Hofmann, S. Pheasant, L. B. Alemany, L. J. Wilson, *Nanotechnology* **2006,** *17(20)*, 5033-5037.

76. J. K. Holt, H. G. Park, Y. Wang, M. Stadermann, A. B. Artyukhin, C. P. Grigoropoulos, A. Noy, O. Bakajin, *Science* **2006,** *312(5776)*, 1034-1037.

77. R. J. Gillies, Z. Liu, Z. Bhujwalla, *Am. J. Physiol.* **1994,** *267(1, Pt. 1)*, C195-C203.

78. R. P. Mason, *Curr. Med. Chem.* **1999,** *6(6)*, 481-499.

79. M. Woods, G. E. Kiefer, S. Bott, A. Castillo-Muzquiz, C. Eshelbrenner, L. Michaudet, K. McMillan, S. D. K. Mudigunda, D. Ogrin, G. Tircso, S. Zhang, P. Zhao, A. D. Sherry, *J. Am. Chem. Soc.* **2004,** *126(30)*, 9248-9256.

80. B. Jebasingh, V. Alexander, *Inorg. Chem.* **2005,** *44(25)*, 9434-9443.

81. S. Laus, A. Sour, R. Ruloff, E. Toth, A. E. Merbach, *Chem. Eur. J.* **2005,** *11(10)*, 3064-3076.

82. B. Sitharaman, S. Asokan, I. Rusakova, M. S. Wong, L. J. Wilson, *Nano Lett.* **2004,** *4(9)*, 1759-1762.

83. T.-H. Cheng, W.-T. Lee, J.-S. Jeng, C.-M. Wu, G.-C. Liu, M. Y. N. Chiang, Y.-M. Wang, *Dalton Trans.* **2006,** *(43)*, 5149-5155.

84. C. Dellago, G. Hummer, *Phys. Rev. Lett.* **2006,** *97(24)*, 245901/1-245901/4.

85. C. Dellago, M. M. Naor, G. Hummer, *Phys. Rev. Lett.* **2003,** *90(10)*, 105902/1-105902/4.

86. I. H. Madshus, *Biochem. J.* **1988,** *250(1)*, 1-8.

87. R. D. Vaughan-Jones, B. E. Peercy, J. P. Keener, K. W. Spitzer, *J. Physiol.* **2002,** *541(1)*, 139-158.

88. C. Bountra, R. D. Vaughan-Jones, *J. Physiol.* **1989,** *418*, 163-87.

89. R. Wang, P. Cherukuri, J. G. Duque, T. K. Leeuw, M. K. Lackey, C. H. Moran, V. C. Moore, J. L. Conyers, R. E. Smalley, H. K. Schmidt, R. B. Weisman, P. S. Engel, *Carbon* **2007,** *45(12)*, 2388-2393.

90. F. Heath, P. Haria, C. Alexander, *AAPS J.* **2007,** *9(2)*, E235-E240.

91. S. Parveen, S. K. Sahoo, *Clin. Pharmacokin.* **2006,** *45(10)*, 965-988.

92. B. Sitharaman, L. J. Wilson, *Int. J. Nanomed.* **2006,** *1(3)*, 291-295.

93. W. Cai, D.-W. Shin, K. Chen, O. Gheysens, Q. Cao, S. X. Wang, S. S. Gambhir, X. Chen, *Nano Lett.* **2006,** *6(4)*, 669-676.

94. X. Montet, K. Montet-Abou, F. Reynolds, R. Weissleder, L. Josephson, *Neoplasia* **2006,** *8(3)*, 214-22.

95. S. A. Anderson, K. K. Lee, J. A. Frank, *Invest. Radiol.* **2006,** *41(3)*, 332-8.

96. D. Pantarotto, J.-P. Briand, M. Prato, A. Bianco, *Chem. Commun.* **2004,** *1(1)*, 16-17.

97. H. S. Wiley, J. J. Herbst, B. J. Walsh, D. A. Lauffenburger, M. G. Rosenfeld, G. N. Gill, *J. Biol. Chem.* **1991,** *266(17)*, 11083-94.

98. W. A. Volkert, T. J. Hoffman, *Chem. Rev.* **1999,** *99(9)*, 2269-2292.

99. J. L. Humm, *Int. J. Radiat. Oncol. Biol. Phys.* **1987,** *13(11)*, 1767-73.

100. B. D. Cheson, *Curr. Drug Targets* **2006,** *7(10)*, 1293-1300.

101. D. H. Silverman, E. S. Delpassand, F. Torabi, A. Goy, P. McLaughlin, J. L. Murray, *Canc. Treat. Rev.* **2004,** *30(2)*, 165-172.

102. R. B. Wilder, G. L. DeNardo, S. J. DeNardo, *J. Clin. Oncol.* **1996,** *14(4)*, 1383-400.

103. J. G. Jurcic, S. M. Larson, G. Sgouros, M. R. McDevitt, R. D. Finn, C. R. Divgi, A. M. Ballangrud, K. A. Hamacher, D. Ma, J. L. Humm, M. W. Brechbiel, R. Molinet, D. A. Scheinberg, *Blood* **2002,** *100(4)*, 1233-1239.

104. M. Miederer, M. R. McDevitt, G. Sgouros, K. Kramer, N.-K. V. Cheung, D. A. Scheinberg, *J. Nucl. Med.* **2004,** *45(1)*, 129-137.

105. E. L. Johnson, T. G. Turkington, R. J. Jaszczak, D. R. Gilland, G. Vaidyanathan, K. L. Greer, R. E. Coleman, M. R. Zalutsky, *Nucl. Med. Biol.* **1995,** *22(1)*, 45-54.

106. D. S. Wilbur, M.-K. Chyan, D. K. Hamlin, B. B. Kegley, R. Risler, P. M. Pathare, J. Quinn, R. L. Vessella, C. Foulon, M. Zalutsky, T. J. Wedge, M. F. Hawthorne, *Bioconj. Chem.* **2004,** *15(1)*, 203-223.

107. J. Kucka, M. Hruby, C. Konak, J. Kozempel, O. Lebeda, *Appl. Radiat. Isot.* **2006,** *64(2)*, 201-206.

108. Y. A. Mackeyev, J. W. Marks, M. G. Rosenblum, L. J. Wilson, *J. Phys. Chem. B* **2005,** *109(12)*, 5482-5484.

109. Q. Lu, J. M. Moore, G. Huang, A. S. Mount, A. M. Rao, L. L. Larcom, P. C. Ke, *Nano Lett.* **2004,** ***4****(12)*, 2473-2477.

110. S. M. Goddu, R. W. Howell, L. G. Bouchet, W. E. Bolsch, D. V. Rao, *MIRD Cellular s-values, published by Society of Nuclear Medicine* **1997**.

111. D. S. Wilbur, R. L. Vessella, J. E. Stray, D. K. Goffe, K. A. Blouke, R. W. Atcher, *Nucl. Med. Biol.* **1993,** *20(8)*, 917-27.

112. G. L. Johnson, R. F. Leininger, E. Segre, *J. Chem. Phys.* **1949,** *17*, 1-10.

113. K. B. Hartman, D. K. Hamlin, D. S. Wilbur, L. J. Wilson, *Small* **2007,** *3(9)*, 1496-9.

114. E. Anders, *Ann. Rev. Nucl. Sci.* **1959,** *9*, 203-20.

115. D. S. Wilbur, D. K. Hamlin, M.-K. Chyan, B. B. Kegley, J. Quinn, R. L. Vessella, *Bioconj. Chem.* **2004,** *15(3)*, 601-616.

116. S. W. Hadley, D. S. Wilbur, M. A. Gray, R. W. Atcher, *Bioconj. Chem.* **1991,** *2(3)*, 171-9.

117. M. M. Campbell, G. Johnson, *Chem. Rev.* **1978,** *78(1)*, 65-79.

118. F. A. Philbrick, *J. Am. Chem. Soc.* **1934,** *56*, 1257-9.

119. K. R. Kissell, K. B. Hartman, P. A. W. Van der Heide, L. J. Wilson, *J. Phys. Chem. B* **2006,** *110(35)*, 17425-17429.

120. J. M. Ashcroft, K. B. Hartman, K. R. Kissell, Y. Mackeyev, S. Pheasant, S. Young, P. A. W. Van der Heide, A. G. Mikos, L. J. Wilson, *Adv. Mater.* **2007,** *19(4)*, 573-576.

121. S. Buono, N. Burgio, M. Hamoudeh, H. Fessi, E. Hiltbrand, L. Maciocco, S. Mehier-Humbert, *Anti-Canc. Agents Med. Chem.* **2007,** *7(4)*, 411-424.

122. G. L. Mayers, *Drug Dev. Res.* **2006,** *67(1)*, 94-106.

123. C.-W. Lam, J. T. James, R. McCluskey, R. L. Hunter, *Toxicol. Sci.* **2004,** *77(1)*, 126-134.

124. A. A. Shvedova, E. R. Kisin, R. Mercer, A. R. Murray, V. J. Johnson, A. I. Potapovich, Y. Y. Tyurina, O. Gorelik, S. Arepalli, D. Schwegler-Berry, A. F. Hubbs, J. Antonini, D. E. Evans, B.-K. Ku, D. Ramsey, A. Maynard, V. E. Kagan, V. Castranova, P. Baron, *Am. J. Physiol.* **2005,** *289(5, Pt. 1)*, L698-L708.

125. D. B. Warheit, B. R. Laurence, K. L. Reed, D. H. Roach, G. A. M. Reynolds, T. R. Webb, *Toxicol. Sci.* **2004,** *77(1)*, 117-125.

126. C.-w. Lam, J. T. James, R. McCluskey, S. Arepalli, R. L. Hunter, *Crit. Rev. in Toxicol.* **2006,** *36(3)*, 189-217.

127. S. Koyama, M. Endo, Y.-A. Kim, T. Hayashi, T. Yanagisawa, K. Osaka, H. Koyama, H. Haniu, N. Kuroiwa, *Carbon* **2006,** *44(6)*, 1079-1092.

128. S.-t. Yang, W. Guo, Y. Lin, X.-y. Deng, H.-f. Wang, H.-f. Sun, Y.-f. Liu, X. Wang, W. Wang, M. Chen, Y.-p. Huang, Y.-P. Sun, *J. Phys. Chem. C* **2007,** *111(48)*, 17761-17764.

129. H. Dai, A. G. Rinzler, P. Nikolaev, A. Thess, D. T. Colbert, R. E. Smalley, *Chem. Phys. Lett.* **1996,** *260(3,4)*, 471-475.

130. N. Gharbi, M. Pressac, M. Hadchouel, H. Szwarc, S. R. Wilson, F. Moussa, *Nano Lett.* **2005,** *5(12)*, 2578-2585.

131. F. Moussa, F. Trivin, R. Ceolin, M. Hadchouel, P. Y. Sizaret, V. Greugny, C. Fabre, A. Rassat, H. Szwarc, *Fullerene Sci. Tech.* **1996,** *4(1)*, 21-9.

132. J. Kolosnjaj, H. Swarc, F. Moussa, "Toxicity Studies of Carbon Nanotubes", *Bio-Applications of Nanoparticles*, Chan, W.C.W, Editor, Landes Biosciences, **2007**, 181-204.

133. S. M. Jay, E. Skokos, F. Laiwalla, M.-M. Krady, T. R. Kyriakides, *Am. J. Pathol.* **2007,** *171(2)*, 632-640.

134. P. Wick, P. Manser, L. K. Limbach, U. Dettlaff-Weglikowska, F. Krumeich, S. Roth, W. J. Stark, A. Bruinink, *Toxicol. Lett.* **2007,** *168(2)*, 121-131.

135. A. Magrez, S. Kasas, V. Salicio, N. Pasquier, J. W. Seo, M. Celio, S. Catsicas, B. Schwaller, L. Forro, *Nano Lett.* **2006,** *6(6)*, 1121-1125.

136. A. Nimmagadda, K. Thurston, M. U. Nollert, P. S. McFetridge, *J. Biomed. Mater. Res. A* **2006,** *76A(3)*, 614-625.

137. Y. Mackeyev, S. Bachilo, K. B. Hartman, L. J. Wilson, *Carbon* **2007,** *45(5)*, 1013-1017.

138. K. Donaldson, R. Aitken, L. Tran, V. Stone, R. Duffin, G. Forrest, A. Alexander, *Toxicol. Sci.* **2006,** *92(1)*, 5-22.